

Ionic liquids based aqueous electrolytes for redox flow batteries

Dissertation

zur Erlangung des Grades

des Doktors der Naturwissenschaften

der Naturwissenschaftlich-Technischen Fakultät

der Universität des Saarlandes

von

Yonglai Zhang

Saarbrücken

2019

Tag des Kolloquiums:	29.08.2019
Dekan:	Prof. Dr. Guido Kickelbick
Berichterstatter:	Prof. Dr. Dr. h.c. Rolf Hempelmann PD Dr. Guido Falk
Vorsitz:	Prof. Dr. Kaspar Hegetschweiler
Akad. Mitarbeiter:	Dr. Anle Wang

Eidesstattliche Versicherung

Hiermit versichere ich an Eides statt, dass ich die vorliegende Arbeit selbstständig und ohne Benutzung anderer als der angegebenen Hilfsmittel angefertigt habe. Die aus anderen Quellen oder indirekt übernommenen Daten und Konzepte sind unter Angabe der Quelle gekennzeichnet. Die Arbeit wurde bisher weder im In- noch im Ausland in gleicher oder ähnlicher Form in einem Verfahren zur Erlangung eines akademischen Grades vorgelegt.

Ort, Datum

Unterschrift

Abstract

Redox flow batteries (RFBs) attract ever increasing attention in stationary energy storage due to the decoupled power and energy. In this dissertation, ionic liquids based aqueous electrolytes have been introduced for RFBs. To develop RFBs with high energy density, it is effective to build high-voltage RFBs or increase the concentration of active species. To realize high-voltage RFBs, hydrophilic ionic liquids have been screened to develop aqueous supporting electrolytes with wide electrochemical stability windows (ESWs) up to 4.4 V. Imidazolium chloride based ionic liquids have been found to be effective reaction media to promote the redox activity of iron species. An aqueous $\text{TiO}_2\text{-FeCl}_2$ hybrid battery has been designed to prove the feasibility to develop high-voltage RFBs. A Zn-Fe hybrid flow battery has been built based on aqueous ionic liquid electrolytes accordingly. The kinetics of iron species and zinc plating/stripping has been investigated. Furthermore, imidazolium chloride based solutions are found to be preferable solvents for hydroquinone to remarkably improve its concentration by eight times at room temperature. An aqueous organic-inorganic hybrid flow battery has been designed based on hydroquinone and zinc chloride, with an unprecedented energy density above 220 Wh L^{-1} theoretically.

Zusammenfassung

Redox-Flow-Batterien (RFBs) finden in stationären Energiespeichern aufgrund der Entkopplung von Leistung und Energie immer mehr Beachtung. In dieser Dissertation wurden wässrige Elektrolyte auf Basis ionischer Flüssigkeiten für RFBs vorgestellt. Um RFBs mit hoher Energiedichte zu entwickeln ist es effektiv, Hochspannungs-RFBs aufzubauen sowie die Konzentration aktiver Spezies zu erhöhen. Zur Realisierung von Hochspannungs-RFBs wurden hydrophile ionische Flüssigkeiten gescreent, um wässrige Leitelektrolyte mit einem breiten elektrochemischen Stabilitätsfenster von bis zu 4,4 V zu entwickeln. Es wurde festgestellt, dass ionische Flüssigkeiten auf Imidazoliumchlorid-Basis Reaktionsmedien sind, die die Redoxaktivität von Eisenspezies wirksam fördern. Eine wässrige $\text{TiO}_2\text{-FeCl}_2$ -Hybridbatterie wurde entwickelt, um die Machbarkeit der Entwicklung von Hochspannungs-RFBs zu beweisen. Analog dazu wurde eine Zn-Fe-Hybrid-Flow-Batterie auf Basis wässriger ionischer Flüssigelektrolyte gebaut. Die Kinetik von Eisenspezies und die Zink-Abscheidung und -Auflösung wurden untersucht. Weiterhin hat sich herausgestellt, dass Lösungen auf der Basis von Imidazoliumchlorid als Lösungsmittel für Hydrochinon geeignet sind, dessen Konzentration bei Raumtemperatur um das Achtefache zu erhöhen. Eine wässrige organisch-anorganische Hybrid-Flow-Batterie wurde auf der Basis von Hydrochinon und Zinkchlorid entwickelt, die theoretisch eine beispiellose Energiedichte von über 220 Wh L^{-1} aufweist.

Acknowledgement

This PhD research work was carried out at Transfercenter Sustainable Electrochemistry, Saarland University and KIST Europe.

First I would like to thank my supervisor, Prof. Dr. Dr. h.c. Rolf Hempelmann, who offered me a nice opportunity to start my PhD research. I really appreciate his kind help and suggestions during my PhD study. He is not only a good scientist with broad research interests, but also a passionate fancier in music and languages. His enthusiastic attitude of learning impressed me and motivated me to explore the unknown world. I also appreciate Prof. Dr. Kaspar Hegetschweiler, who serves as my scientific advisor, for his benignity and insightful comments in my annual presentations. This memorable experience of PhD study is a wonderful gift to support me when I encounter difficulties and challenges in my future career.

I am grateful to Dr. Sangwon Kim, a principal investigator at KIST Europe, for his nice coordination and support in this project. Thanks to Dr. Ruiyong Chen for his guidance in my early PhD research. Technical problems always exist in scientific research, especially in the startup of my work. Here I would like to thank Rudolf Richter and technicians in the workshop of Saarland University, for their assistance in manufacture of flow cell and H-cell devices, as well as Prof. Dr. Dirk Henkensmeier at KIST Soul for providing us some anion exchange membranes. Dr. Matthias Altmeyer at KIST Europe is warm-hearted and always ready to help people, many thanks for his technical support.

Furthermore, I would like to thank my colleagues in Prof. Hempelmann's group and KIST Europe, this PhD work could not be finished without their assistance. I want to give my special thanks to Sang Jun Yoon, who gladly shared his facilities and experimental consumables and offered sincere help. Thanks to Dr. Jaeho Lee, Galina Skorikova and Zhenzhen Wang for their kind help in my PhD study. Sincere thanks to Daniel Rauber, who has rich experience in synthesis and characterization of ionic liquids, for his warm-hearted help in viscosity test and partial discussion. I also express my gratitude to Dr. Dan Durneata for XRD measurements and Carsten Brill

for SEM tests.

Subsequently, I want to thank my committee members for their positive feedback and constructive comments on my thesis.

Finally, I would like to appreciate my relatives and friends, for their firm support and continuous encouragement during my PhD study.

Table of Contents

Abstract.....	i
Zusammenfassung.....	ii
Acknowledgement	iii
List of abbreviations.....	vii
List of Tables.....	viii
List of Figures.....	ix
1 Introduction.....	1
1.1 The technology of redox flow battery.....	1
1.2 Typical redox flow batteries.....	3
1.2.1 All vanadium redox flow battery	3
1.2.2 Iron–vanadium redox flow battery.....	5
1.2.3 Zinc–halogen flow battery	5
1.2.4 Polysulfide–bromine flow battery.....	6
1.2.5 New-concept flow batteries.....	7
1.3 Current progress and challenges of redox flow batteries	12
1.3.1 Typical active species for redox flow batteries	12
1.3.2 Liquid media for redox flow batteries.....	18
1.3.3 Current issues for redox flow batteries.....	19
1.4 Ionic liquids and their applications in redox flow batteries	22
1.5 Scope of this thesis.....	24
2 Characterization methods.....	26
2.1 Physical properties	26
2.2 Anodic oxidation.....	26
2.3 Electrochemical tests.....	27
2.3.1 Electrochemical impedance spectroscopy.....	27
2.3.2 Cyclic voltammetry.....	28
2.3.3 Galvanostatic charge/discharge test	29
3 Screening of ionic liquids for aqueous electrolytes.....	31
3.1 Experimental.....	32
3.1.1 Preparation and characterization of “water-in-ionic-liquid” solutions.....	32
3.1.2 Preparation and characterization of anodic titanium dioxide	33
3.1.3 Electrochemical test of titanium dioxide–iron (II) chloride hybrid battery.....	33
3.2 Characterization of electrochemical stability windows.....	34
3.3 Physical properties of aqueous ionic liquid electrolytes	38
3.4 Prototype of a titanium dioxide–iron (II) chloride hybrid battery.....	41
3.5 Conclusions.....	48
4 Ionic liquid based aqueous electrolytes for a zinc–iron hybrid flow battery	49
4.1 Experimental.....	50
4.1.1 Preparation and characterization of electrolytes.....	50
4.1.2 Assembly of symmetric Zn–Zn cells and characterization of zinc dendrites..	51
4.1.3 Electrochemical tests of the zinc–iron flow battery	51
4.2 Design of the zinc–iron hybrid flow battery	52
4.3 Optimization of catholyte and anolyte	53

4.4	Kinetic analyses of Zn-based and Fe-based redox active species	63
4.5	Performance of the zinc–iron hybrid flow battery	69
4.6	Conclusions	72
5	Aqueous ionic liquid electrolytes towards an organic–inorganic hybrid flow battery	73
5.1	Experimental	73
5.1.1	Preparation and characterization of the electrolytes.....	73
5.1.2	Flow battery tests	74
5.2	Development of an organic–inorganic hybrid flow battery.....	74
5.3	Conclusions.....	83
6	Summary and outlook	84
Appendix	86
	Chemical list	86
	Publications and activities.....	87
	Bibliography	88

List of abbreviations

AEM	Anion exchange membrane
ATO	Anodic titanium oxide
CE	Counter electrode
CEM	Cation exchange membrane
CV	Cyclic voltammetry
EIS	Electrochemical impedance spectroscopy
GC	Glassy carbon
IEM	Ion exchange membrane
IL	Ionic liquid
PBI	Polybenzimidazole
PSBFB	Polysulfide–bromine flow battery
RE	Reference electrode
RFB	Redox flow battery
SEM	Scanning electron microscopy
VRFB	Vanadium redox flow battery
WE	Working electrode
XRD	X-ray diffraction
ZBFB	Zinc–bromine flow battery
ZHFB	Zinc–halogen flow battery
ZIFB	Zinc–iodine flow battery

List of Tables

Table 1.1 Redox-targeting reactions with two redox shuttle mediators in a flow battery.	9
Table 1.2 Molecular modifications of active species for redox flow batteries.	20
Table 3.1 Compositions of the “water-in-ionic-liquid” solutions.	38
Table 3.2 Viscosities of the “water-in-ionic-liquid” solutions.	40
Table 3.3 Capacity comparison of TiO ₂ based rechargeable batteries.	48
Table 5.1 Physical properties of Nafion based membranes.	80

List of Figures

- Figure 1.1** Schematic illustration of (a) typical RFB system, 1. flow cell, 2. electrode, 3. ion exchange membrane, 4. current collector, 5. reservoir, 6. electrolyte, 7. pump; (b) a hybrid RFB system with (i) gas, (ii) solid or (iii) solid suspension/colloidal dispersion as redox active species.2
- Figure 1.2** Redox-targeting reactions with (a) one redox shuttle mediator and (b) two redox shuttle mediators; (c) illustration of a flow battery via redox-targeting reactions with two redox shuttle mediators. Red line represents the charge process, while blue line represents the discharge process. An asterisk (*) represents the oxidized state and an octothorpe (#) represents the reduced state, respectively.8
- Figure 1.3** A scheme of multiple ion exchange membranes based redox flow battery. 10
- Figure 1.4** Redox potentials of active species versus standard hydrogen electrode (SHE). Abbreviations: 7,8-dihydroxyphenazine-2-sulfonic acid (DHPS); triethanol- amine (TEOA); 2,6-dihydroxyanthraquinone (DHAQ); alloxazine 7/8-carboxylic acid (ACA); methyl viologen (MV); 9,10-anthraquinone-2,7-disulfonic acid (AQDS); ferrocene (Fc); quaternary ammonium salts (QA); 1,4-benzoquinone/p-hydroquinone (Q/H₂Q); 4-hydroxy-2,2,6,6-tetramethylpiperidin -1-oxyl (4-HO-TEMPO). 13
- Figure 1.5** Molecular modifications of (a) para-hydroquinone (p-H₂Q) and ortho-hydroquinone (o-H₂Q); (b) ferrocene (Fc) and the corresponding derivatives, FcNCl and FcN₂Br₂ (Ref. ^[77]), BTMAP-Fc (Ref. ^[78]); (c) 4-HO-TEMPO and the corresponding derivatives, pTEMPO-pNCl (Ref. ^[81]), TEMPTMA (Ref. ^[82,96]) and g⁺- TEMPO (Ref. ^[15]). 16
- Figure 1.6** Synthesis routes of viologens (top: MV, Ref. ^[82]) and its two-electron-reaction derivative (bottom: viologen derivative, Ref. ^[78,98]). 17
- Figure 1.7** Representative (a) cations and (b) anions of ionic liquids. Abbreviations: PDDA (poly dimethyl diallyl ammonium); DBU (1,8-di aza bicyclo [5.4.0]undec-7 -ene); QA (quaternary ammonium); QP (quaternary phosphonium); OTf (trifluoromethanesulfonate, triflate); TFSI (bis(trifluoromethane)sulfonimide); FSI (bis(fluorosulfonyl)imide); DCA (dicyanamide). 22
- Figure 2.1** Scheme of anodic oxidation. 26
- Figure 2.2** (a) Relationship between the alternating voltage signal and response current, (b) typical Nyquist plot. 27
- Figure 2.3** A laboratory-scale flow cell, (a) components, 1. end plate, 2. copper

current collector, 3. graphite bipolar plate, 4. gasket; (b) front view and (c) top view of an assembled flow cell.	29
Figure 3.1 CV curves of (a) EMImCl/H ₂ O, (b) BMImCl/H ₂ O, (c) TEACl/H ₂ O, (d) TBACl/H ₂ O, (e) TriMImMeSO ₄ /H ₂ O and (f) EMMImEtSO ₄ /H ₂ O at 20 mV s ⁻¹ , arrows indicate scan direction.	34
Figure 3.2 (a) Summary of ESWs of “water-in-ionic-liquid” solutions and lithium salt solutions, * data from Ref. ^[142] , potential values are now referenced to the Ag/AgCl. (b) Molecular structures of the selected ionic liquids. (c) Scheme of interaction between water molecules and ionic liquids.	36
Figure 3.3 Digital photographs of the “water-in-ionic-liquid” solutions: fresh prepared solutions (a, b) and solutions rested for two weeks (c, d). 1: EMImCl/H ₂ O (20 m); 2: BMImCl/H ₂ O (20 m); 3: TEACl/H ₂ O (15 m); 4: TBACl/H ₂ O (15 m); 5: TriMImMeSO ₄ /H ₂ O (20 m); 6: EMMImEtSO ₄ /H ₂ O (20 m).	39
Figure 3.4 Ionic conductivities of the “water-in-ionic-liquid” solutions at different molalities (solvent refers to water).	40
Figure 3.5 XRD pattern of anodic titanium dioxide (ATO).	41
Figure 3.6 SEM images of ATO, (a) cross-section of ATO film, (b) enlarged cross-section of ATO film, (c) front-view of ATO film, (d) back-view of ATO film.	42
Figure 3.7 (a) Electrochemical stability windows of aqueous LiCl solutions at 20 mV s ⁻¹ . CV curves of ATO in (b) aqueous LiCl solutions, (c) BMImCl/H ₂ O (10 m) with or without LiCl at 10 mV s ⁻¹ , arrows indicate scan direction.	43
Figure 3.8 CV curves of ATO in (a) BMImCl/H ₂ O (10 m) with 1.0 M of LiCl at different scan rates and (b) BMImCl/H ₂ O (10 m) containing different amounts of LiCl at 10 mV s ⁻¹ , arrows indicate scan direction.	44
Figure 3.9 CV curves of of ATO in EMImCl/H ₂ O (10 m) containing 1.0 M of LiCl at 10 mV s ⁻¹ , arrow indicates scan direction.	44
Figure 3.10 CV curves of of ATO in EMMImEtSO ₄ /H ₂ O (10 m) containing 1.0 M of LiCl at 10 mV s ⁻¹ , arrow indicates scan direction.	45
Figure 3.11 CV curves of iron active species in water and BMImCl/H ₂ O (10 m) at 10 mV s ⁻¹ , arrow indicates scan direction.	45
Figure 3.12 A digital photograph of home-made H-cell.	46
Figure 3.13 (a) Illustration of an aqueous TiO ₂ -FeCl ₂ hybrid battery. CV curves of (b) ATO in BMImCl/H ₂ O (10 m) containing 1.0 M of LiCl, and (c) BMImCl/H ₂ O (10 m) containing 0.1 M of FeCl ₂ and 1.0 M of HCl at scan rates of 10 mV s ⁻¹ , arrows indicate scan direction. (d) Cycle	

performance of aqueous hybrid battery at 10 mA cm^{-2} , inset shows the charge/discharge curves.....	47
Figure 4.1 Redox potentials of Fe-based and Zn-based redox active species. Abbreviations: triethanolamine (TEOA); ferrocene (Fc); quaternary ammonium salts (QA); 1,10-phenanthroline (phen).	52
Figure 4.2 CV curves of 50 mM FeCl_2 in (a) H_2O ; (b) various aqueous ionic liquid solutions.	53
Figure 4.3 Different molalities of $\text{BMImCl}/\text{H}_2\text{O}$ without HCl addition.	54
Figure 4.4 Electrochemical stability windows (ESWs) of $\text{BMImCl}/\text{H}_2\text{O}$ (8 m) with different amount of HCl addition.	55
Figure 4.5 CV curves of (a) ZnCl_2 (50 mM) in $\text{BMImCl}/\text{H}_2\text{O}$ (8 m) with different amount of NH_4Cl	55
Figure 4.6 CV curves of (a) aqueous GB solution (6 m to balance the osmotic pressure from the catholyte) with NH_4Cl and (b) ZnCl_2	56
Figure 4.7 Electrochemical stability windows (ESWs) of NH_4Cl solutions.	57
Figure 4.8 Electrochemical stability windows (ESWs) of $\text{CaCl}_2/\text{H}_2\text{O}$ (3.5 m) with different amount of NH_4Cl addition.....	57
Figure 4.9 CV curves of ZnCl_2 (10 mM) in $\text{CaCl}_2/\text{H}_2\text{O}$ (3.5 m) with different amount of NH_4Cl addition.....	58
Figure 4.10 Charge/discharge curves of symmetric Zn–Zn cells with different aqueous supporting electrolytes, (a) NH_4Cl solutions range from 0~1.0 M; (b) BMImCl and CaCl_2 solutions with/without NH_4Cl . The circles inside indicate the short circuit during charge/discharge test.....	59
Figure 4.11 SEM images of the Zn metal in symmetric Zn–Zn cells after charge/discharge curves with different supporting electrolytes (E1~E8), (a) E1, (b) E2, (c) E3, (d) E4, (E) E5, (F) E6, (G) E7, (H) E8. Inset shows the corresponding enlarged images.	60
Figure 4.12 Schematic illustration of a Zn–Fe hybrid flow battery (a); (b) top: CV curves of 10 mM ZnCl_2 and 50 mM FeCl_2 in $\text{CaCl}_2/\text{H}_2\text{O}$ (3.5 m) with 0.5 M NH_4Cl and $\text{BMImCl}/\text{H}_2\text{O}$ (8 m) with 1.0 M HCl , respectively; bottom: ESWs of the supporting electrolytes, scan rates: 20 mV s^{-1}	62
Figure 4.13 (a) CV curves of 10 mM ZnCl_2 in different aqueous NH_4Cl solutions; (b) current densities of zinc plating/stripping versus overpotentials and the corresponding standard rate constant (right table), a: 0 M NH_4Cl ; b: 0.2 M NH_4Cl ; c: 0.5 M NH_4Cl ; d: 1.0 M NH_4Cl	64
Figure 4.14 Current densities versus overpotentials in zinc plating/stripping with different supporting electrolytes containing 0.5 M NH_4Cl and the corresponding standard rate constants (table below).	66

Figure 4.15 CV curves of 1 mM FeCl ₂ and 1 mM FeCl ₃ in BMImCl/H ₂ O (8 m) with 1.0 M HCl (a) at various scan rates; (b) peak currents versus square roots of scan rates; (c) and (d) experimental and simulated CV curves at low and high scan rates; (e) peak separation and peak current ratio versus scan rates; (f) CV stability at 20 mV s ⁻¹	67
Figure 4.16 Representative CV curve of 1 mM FeCl ₂ and 1 mM FeCl ₃ in BMImCl/H ₂ O (8 m) with 1.0 M HCl after calibration with baselines. ...	68
Figure 4.17 Ionic conductivities of iron (III)/(II) chloride in BMImCl/H ₂ O (8 m) with 1.0 M HCl, and ZnCl ₂ in CaCl ₂ /H ₂ O (3.5 m) with 0.5 M NH ₄ Cl, respectively.	69
Figure 4.18 Galvanostatic charge/discharge performance of Zn–Fe hybrid flow battery. (a) charge/discharge curves and (b) efficiencies at 20 mA cm ⁻² ; (c) and (d) test in an H-cell at 10 mA (contact area of graphite rod and electrolyte: 0.75 cm ²), inset shows the charge/discharge curves of the Zn–Fe H-cell.	70
Figure 4.19 EIS of the Zn–Fe hybrid flow battery before and after cycle test at 20 mA cm ⁻²	71
Figure 5.1 Concentration of H ₂ Q in different molalities of BMImCl/H ₂ O solutions. The concentration is calculated based on the total volume after thorough dissolution of H ₂ Q, e.g. 9 mmol H ₂ Q can be dissolved in 1 mL of BMImCl/H ₂ O (10 m) with total volume of 1.8 mL.....	75
Figure 5.2 Redox behavior of H ₂ Q in different molality of BMImCl/H ₂ O, (a) CV curves at 20 mV s ⁻¹ ; and (b) the corresponding anodic peak currents as well as the peak separation.	76
Figure 5.3 CV curves of 10 mM H ₂ Q in BMImCl/H ₂ O (5 m) with different additives: (a) LiCl and (b) NH ₄ Cl.	77
Figure 5.4 CV curves of ZnCl ₂ in BMImCl/H ₂ O (5 m) with different amount of NH ₄ Cl, (a) 0 M NH ₄ Cl; (b) 0.2 M NH ₄ Cl; (c) 0.5 M NH ₄ Cl.	78
Figure 5.5 CV curves of 25 mM ZnCl ₂ and 10 mM H ₂ Q in the supporting electrolyte of BMImCl/H ₂ O (5 m) containing 0.5 M NH ₄ Cl.	79
Figure 5.6 Charge/discharge curves of H ₂ Q–ZnCl ₂ hybrid flow battery with a PVDF/Nafion composite membrane at ± 1.5 mA cm ⁻² , inset shows the cycle curves. Catholyte: 10 mL of 0.1 M H ₂ Q in BMImCl/H ₂ O; anolyte: 10 mL of 0.2 M ZnCl ₂ in BMImCl/H ₂ O, 0.4 M LiCl was used as conductive additive in both catholyte and anolyte.	81
Figure 5.7 EIS curves of the H ₂ Q–ZnCl ₂ hybrid flow battery with Nafion based membranes, (a) before and (b) after galvanostatic cycling test with potential limitation (GCPL).....	81
Figure 5.8 CV curve of anolyte in the H ₂ Q–ZnCl ₂ hybrid flow battery after charge/discharge test.	82

1 Introduction

1.1 The technology of redox flow battery

The depletion of fossil fuels, e.g. crude oil, coal and natural gas, makes it urgent to search alternative energy sources. Furthermore, the combustion of fossil fuels causes serious environmental issues. Renewable and sustainable solar, wind and tide energy sources attract intensive interest in recent decades.^[1] Consequently, the global energy crisis has stimulated booming market for energy conversion and storage. On account of the natural intermittency of these renewables, integration of electric grids and energy storage devices becomes a primary choice.^[2]

Redox flow batteries (RFBs) present remarkable potential for grid-scale energy storage in the regulation of peak shaving and load shifting, owing to their merits of quick response and high safety at operation, long calendar life as well as deep discharge capability.^[1,3] In a RFB, the power and energy can be decoupled regardless of the scale of cell stacks. Unlike ordinary rechargeable batteries, for instance, lithium-ion batteries (LIBs), in which the energy is stored by electrochemical reactions of solid active materials,^[4] in RFBs the energy is stored in flowable electrolytes, this unique cell architecture enables RFBs high design flexibility and modularity. That is to say, the capacity of a LIB is confined by the size of cell stacks; while the capacity of a RFB can be increased in demand even in limited cell stacks, as long as the required volumes of electrolytes are available.

The earliest prototype of flow battery was invented in 1884 by French engineers, Charles Renard and his colleague Arthur Krebs, who utilized a zinc–chlorine flow battery to power their airship called La France to eight kilometers in 23 minutes.^[5] Afterwards, Kangro and his coworkers filed a patent to introduce a method for energy storage with chromous sulfate dissolved in sulfuric acid as the positive and negative electrolytes in 1949.^[6,7] However, it was not until the 1970s, Lawrence Thaller, a scientist at the National Aeronautics and Space Administration (NASA), invented the

modern RFB, using a Fe (III)/(II) ($\text{Fe}^{3+}/\text{Fe}^{2+}$) halide solution and a chromic/chromous ($\text{Cr}^{3+}/\text{Cr}^{2+}$) halide solution as positive and negative electrolytes, respectively.^[2] In 1984, Maria Skyllas-Kazacos and her colleagues at the University of New South Wales, Australia invented all vanadium redox flow battery (VRFB), taking vanadium compounds as active species in both catholyte and anolyte,^[8] which attracted considerable attention in the next decades.

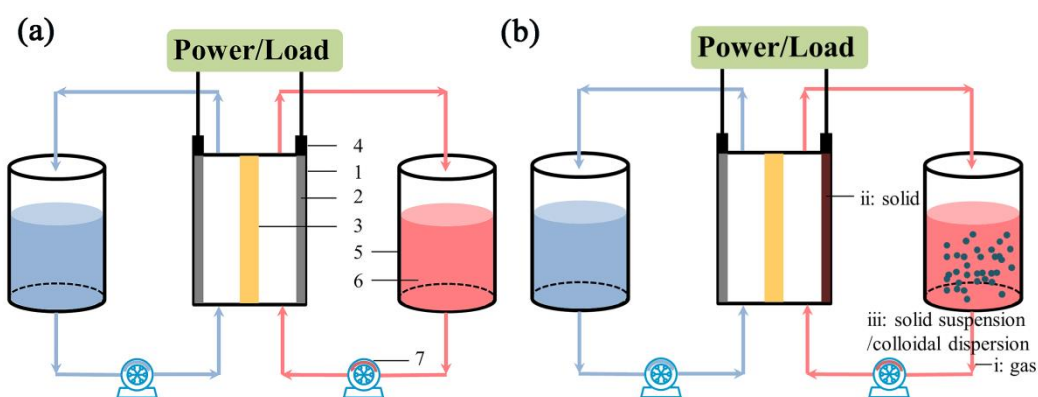


Figure 1.1 Schematic illustration of (a) typical RFB system, 1. flow cell, 2. electrode, 3. ion exchange membrane, 4. current collector, 5. reservoir, 6. electrolyte, 7. pump; (b) a hybrid RFB system with (i) gas, (ii) solid or (iii) solid suspension/colloidal dispersion as redox active species.

As illustrated in Figure 1.1a, in a RFB system, liquid-state electrolytes are circulated between the cell stacks and reservoirs by pumps, the catholyte and anolyte are separated by ion exchange membranes (IEMs) to prevent cross-contamination. During charge/discharge process, the electric energy is stored/released by electrochemical reactions of redox active species in the flowing electrolytes.^[9] The cathode and anode of a RFB are the sites electrochemical reactions take place but not where the energy stores/releases, unlike conventional rechargeable batteries and supercapacitors. Alternatively, solid materials (e.g. zinc metal), gases (e.g. oxygen gas), solid suspensions and colloidal dispersions are also introduced as active species for hybrid flow batteries, as shown in Figure 1.1b.^[1,10] To overcome the limitation of concentration as well as crossover of active species, insoluble solid suspensions in liquid media are utilized as redox electrolytes for semi-solid flow batteries (SSFBS);^[11]

similarly, redox active colloidal dispersions have also been proposed to cope with issues of concentration and crossover.^[12]

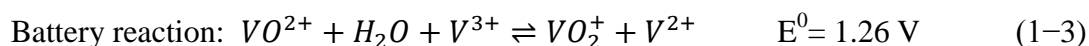
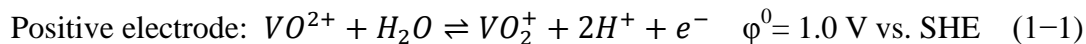
The key parts of a RFB are electrolytes, membranes and electrodes. Generally, active materials are dissolved to prepare aqueous or non-aqueous electrolytes; insoluble active materials are dispersed in liquid media homogeneously as electrolytes for SSFBs. Cation exchange membranes (CEMs, e.g. perfluorosulfonic acid ionomer (Nafion) membrane)^[13,14] or anion exchange membranes (AEMs, e.g. methylated polybenzimidazole membrane or polymeric membranes with abundant quaternary ammonium groups)^[15,16] are utilized to prevent crossover of catholyte and anolyte in RFBs. Zhang et al. developed a series of porous membranes for VRFBs, by means of induced phase inversion technique (PIT) to immerse casted polymer solution in water or organic solvents.^[17] It is noteworthy that these cost-effective membranes are non-ion-selective separators essentially, thus they are only applicable in specific RFBs which can cope with crossover of electrolytes by the battery systems themselves, for instance, VRFBs. Details of these flow battery systems will be discussed in chapter 1.2 later. Carbon felts after thermal treatment, chemical oxidation or surface modification are universal electrode materials for RFBs.^[18,19] To improve the electrochemical kinetics of active species, modified graphite felts^[20] and nanoporous carbon materials^[21] are also introduced as electrode materials for flow batteries. The surface treatment of carbon felts enhances the wettability for electrolytes. Sun and Skyllas-Kazacos suggested that the improved wettability and electrochemical activity can be ascribed to the abundant C–OH and C=O functional groups on the carbon felts after surface treatment.^[22]

1.2 Typical redox flow batteries

1.2.1 All vanadium redox flow battery

All vanadium redox flow battery (VRFB) is currently the most popular flow battery system in both academia and industry.^[22] Vanadyl sulfate (or vanadium oxysulfate) is dissolved in sulfuric acid to serve both as catholyte and anolyte. Multivalent

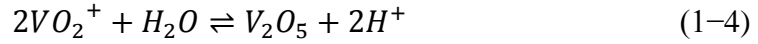
vanadium ions are the redox active species in the same supporting electrolyte on cathode side and anode side. During charge/discharge, electrochemical reactions of high valent VO_2^+/VO^{2+} species in the catholyte and low valent V^{3+}/V^{2+} species in the anolyte take place, respectively. The redox reactions and the redox potentials (vs. standard hydrogen electrode, SHE) can be found below.^[22]



The mutual transformation of these multivalent vanadium ions enables them to cope with crossover. Once crossover occurs, for instance, when the high valent VO_2^+/VO^{2+} ions in catholyte migrate into anolyte, they can be reduced to low valent V^{3+}/V^{2+} ions accordingly, and vice versa. This interesting phenomenon can be also found in some other flow battery systems which use sole-element-based redox active species with the same supporting electrolyte, e.g. all iron based flow battery,^[23] all chromium based flow battery^[8] and soluble lead-acid flow battery.^[24] However, rebalance of the electrolytes in maintenance is the most effective way to solve crossover in practical stationary flow battery system, owing to the different diffusion rates of the redox active species with varied chemical valences.

Nevertheless, the performance of VRFBs is strongly dependent on the concentration of vanadium ions, ion exchange membranes and electrode materials. The vanadium concentration is limited by the low solubility of $VOSO_4$ below $-5 \text{ }^\circ\text{C}$ and precipitation of V_2O_5 above $40 \text{ }^\circ\text{C}$.^[25] The side reaction of V_2O_5 precipitation at high temperature is shown in equation 1-4. Considering the different solubility of V^{II} , V^{III} , V^{IV} and V^V species in sulfuric acid, an optimized vanadium concentration of 1.6~2 M and a total sulfate concentration of 4~5 M in the electrolyte are preferred for VRFBs, with operating temperature range of 10~40 $^\circ\text{C}$.^[26] Therefore, the general energy density of VRFBs is quite low (25~30 Wh L^{-1}). Yang et al. reported a new VRFB with a mixture of sulfuric acid and hydrochloric acid as supporting electrolytes, enabling a concentration of 2.5 M vanadium ions. This new VRFB achieved an energy density of 43 Wh L^{-1} with increase of 70%, and could operate at wide

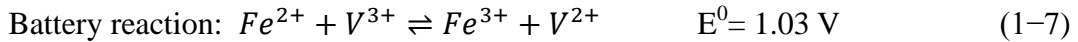
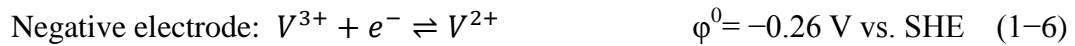
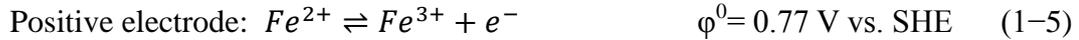
temperature range from -5 to 50 °C.^[25]



Since VRFBs use vanadium compounds in aqueous strong acid as electrolytes, hydrogen evolution on negative side in charge process can be a potential risk. The possibly carcinogenic vanadium ions and corrosive acid raise a safety concern. Furthermore, the high-cost Nafion membrane ($600\sim 800$ \$ m^{-2})^[17] and vanadium compounds it utilizes also retard the universal application of VRFBs.

1.2.2 Iron–vanadium redox flow battery

Yang and colleagues reported iron–vanadium redox flow battery (Fe–V RFB), taking Fe^{3+}/Fe^{2+} and V^{3+}/V^{2+} redox active species, respectively, similar to Fe–Cr redox chemistry proposed by the NASA.^[27] In contrast to Cr^{3+}/Cr^{2+} species, V^{3+}/V^{2+} species shows much higher redox activity.^[28] In their Fe–V RFB system, equal molar ratio of $FeCl_2$ and VCl_3 are dissolved in hydrochloric acid together to serve both as catholyte and anolyte to cope with crossover. The redox reactions are shown below:

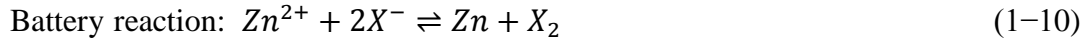


Later they made further optimization of Fe–V RFB with mixed hydrochloric acid and sulfuric acid to achieve a higher concentration of 1.5 M both for Fe^{3+}/Fe^{2+} and V^{3+}/V^{2+} redox active species.^[29] The utilization of low-cost microporous separator and iron (II) chloride in Fe–V RFB reduced the capital cost significantly, and further accelerated the market penetration of Fe–V RFB.

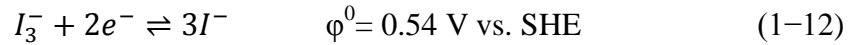
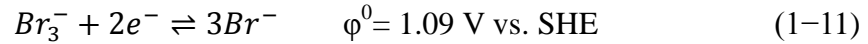
1.2.3 Zinc–halogen flow battery

Zinc–halogen flow battery (ZHFB), e.g. zinc–bromine flow battery (ZBFB),^[21] zinc–iodine flow battery (ZIFB),^[30] is a group of hybrid flow batteries which provoke widespread interest, owing to the natural abundance and high solubility of zinc halides (ZnX_2 , $X=Cl, Br, I$). In a ZHFB, the zinc halide solution is used both as catholyte and anolyte, therefore, ZHFB is regarded as a group of representatives

which can mitigate against crossover problem by themselves. By means of zinc plating/stripping on anode side and redox reaction of halides on cathode side, respectively, the redox reactions are elucidated below:



Considering the complexing behavior of bromide and iodide, possible cathode reactions are also shown in equations 1-11 and 1-12, which have comparable redox potentials with corresponding active species in equation 1-8.

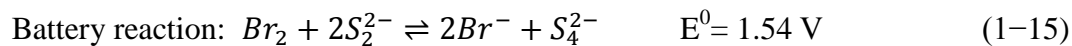
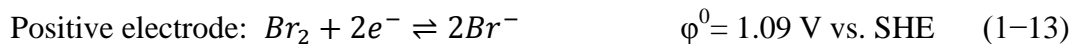


Due to the toxicity and gaseous nature of chlorine gas, current research about ZHFB mainly focuses on ZBFB and ZIFB. Zhang et al. introduced cage-like porous carbon materials to entrap Br_2 -complex and enhance the redox activity, realizing a Coulombic efficiency of 98% and an energy efficiency of 81% at a current density of 80 mA cm^{-2} , which were among the highest values for ZBFB to date.^[21] Wang et al. demonstrated a discharge energy density of 167 Wh L^{-1} in an aqueous zinc-polyiodide flow battery, with near-neutral 5.0 M ZnI_2 electrolyte.^[30] Afterwards, Lu and colleagues exploited bromide ions (Br^-) as a complexing agent to form soluble iodine–bromide ions (I_2Br^-), achieving a higher energy density of 202 Wh L^{-1} based on the volume of catholyte.^[31] Inspired by zinc electrochemical plating/stripping in basic solutions, Chen and coworkers designed an all-aqueous zinc–iodine redox flow battery, presenting a high voltage of 1.8 V and an unprecedented energy density of 330.5 Wh L^{-1} .^[32] Recently Li et al. proposed a self-healing zinc–iodine flow battery, in which the zinc dendrites can react with absorbed I_3^- ions in the microporous membrane, consequently the energy efficiency achieved as high as 82% at a current density of 80 mA cm^{-2} .^[33]

1.2.4 Polysulfide–bromine flow battery

Polysulfide–bromine flow battery (PSBFB) was invented in 1984. The sulfide in

anolyte and bromine in catholyte are naturally abundant and highly soluble in water. The PSBFB has a voltage of 1.5 V according to the following equations: ^[8,34]



The energy efficiency of PSBFB is around 60~65%, with an energy density of 20~30 Wh L⁻¹. The performance can be improved with WS₂ as an electrocatalyst for polysulfide to enhance its redox activity in aqueous alkaline solutions.^[1] However, the PSBFB suffers from serious cross-contamination of electrolytes and precipitation of sulfur species over cycles. Furthermore, the release of toxic vapor such as Br₂ and H₂S remains a safety concern.^[8,34] Similar to PSBFB, Lu and coworkers reported a polysulfide–iodide redox flow battery,^[35] in which the conventional volatile bromine was replaced with iodine species. This flow battery demonstrated an average voltage of 1 V and an overall energy density of 43.1 Wh L⁻¹ based on the total volume of catholyte and anolyte.

1.2.5 New-concept flow batteries

Conventional RFBs take liquid-state solutions containing soluble redox active species as electrolytes. In recent years, some new-concept flow batteries are put forward to address the conundrums of crossover and low energy density.

(a) Semi-solid flow battery

The energy density of commercial LIBs can reach as high as 600 Wh L⁻¹, almost 20 times higher than that of RFBs. Providing that the active materials of LIBs can be flowable like RFBs to achieve the capacity at solid state, an ultrahigh energy density would be realized theoretically. Taking advantage of the active electrode materials, electrolytes and separators of LIBs, Chiang et al. proposed semi-solid flow batteries (SSFBS).^[11] Commercial cathode materials such as lithium cobalt oxide (LiCoO₂), lithium iron phosphate (LiFePO₄) and spinel lithium nickel manganese oxide (LiNi_{0.5}Mn_{1.5}O₄), as well as anode materials like graphite powder, lithium titanium oxide (Li₄Ti₅O₁₂) and mesocarbon microbeads (MCMB) were mixed with conductive

carbon black, then dispersed in non-aqueous electrolytes as suspensions. Both lithium metal anode and suspensions of commercial anode materials were paired with suspensions of cathode materials for the prototype SSFBs. Recent progress of SSFBs has been reported by Lu^[36] and Biendicho^[37] et al. Even though the theoretical energy density of SSFB is quite high, it can only operate at very low current densities since it involves sluggish ion diffusion in the solid-state active materials.^[38]

(b) Redox-targeting reactions based flow battery

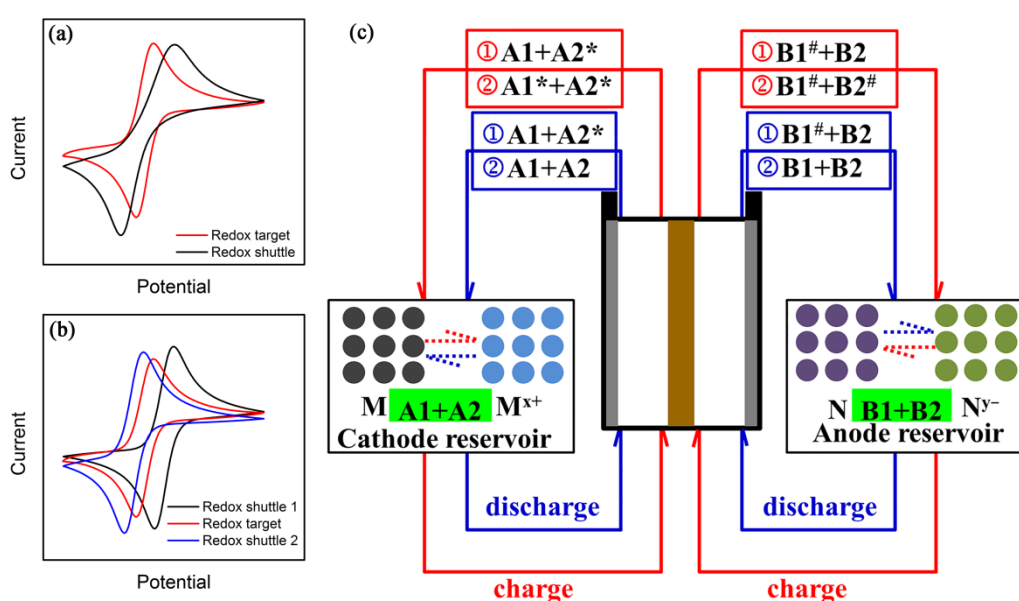


Figure 1.2 Redox-targeting reactions with (a) one redox shuttle mediator and (b) two redox shuttle mediators; (c) illustration of a flow battery via redox-targeting reactions with two redox shuttle mediators. Red line represents the charge process, while blue line represents the discharge process. An asterisk (*) represents the oxidized state and an octothorpe (#) represents the reduced state, respectively.

Wang and Grätzel et al. introduced redox-targeting reactions to realize batteries with high energy density, a dissolved redox shuttle mediator in the electrolyte is oxidized by charging, and chemically reduced back to its original state when transferring the charges to the solid active material (“target”) by bulk diffusion.^[39,40] However, the redox-targeting reactions can be quite complicated, for each solid active material, one or two redox shuttle mediators are needed to complete charge and discharge process, respectively. As illustrated in Figure 1.2a, if the redox shuttle

mediator has higher oxidative potential and lower reduced potential than the target, only one redox shuttle mediator is required;^[41] otherwise two redox shuttle mediators are required to complete the redox-targeting reactions (Figure 1.2b).^[42] In the latter case, to complete a roundtrip process, redox molecule A1 with a high formal potential chemically oxidizes the solid active material, while redox molecule A2 with a lower formal potential chemically reduces the solid active material.^[43]

Table 1.1 Redox-targeting reactions with two redox shuttle mediators in a flow battery.

	Positive electrode	Negative electrode
charge	$A2 \rightarrow A2^* + ae^-$ $\left(\begin{array}{l} A1 \rightarrow A1^* + be^- \\ A1^* + M \rightarrow A1 + M^{x+} \end{array} \right)$ $A1 \rightarrow A1^* + be^-$	$B1 + ce^- \rightarrow B1^\#$ $\left(\begin{array}{l} B2 + de^- \rightarrow B2^\# \\ B2^\# + N \rightarrow B2 + N^{y-} \end{array} \right)$ $B2 + de^- \rightarrow B2^\#$
discharge	$A1^* + be^- \rightarrow A1$ $\left(\begin{array}{l} A2^* + ae^- \rightarrow A2 \\ A2 + M^{x+} \rightarrow A2^* + M \end{array} \right)$ $A2^* + ae^- \rightarrow A2$	$B2^\# \rightarrow B2 + de^-$ $\left(\begin{array}{l} B1^\# \rightarrow B1 + ce^- \\ B1 + N^{y-} \rightarrow B1^\# + N \end{array} \right)$ $B1^\# \rightarrow B1 + ce^-$

The scheme of a flow battery via redox-targeting reactions with two redox shuttle mediators is demonstrated as Figure 1.2c. A1, A2, B1 and B2 are soluble redox shuttle mediators, while M and N are the insoluble solid active materials. The redox potentials of A1, M, A2 are E_1, E_M, E_2 , respectively, in an order of $E_2 < E_M < E_1$; the redox potentials of B1, N, B2 are E'_1, E_N, E'_2 , respectively, in an order of $E'_2 < E_N < E'_1$. The overall reactions can be found in Table 1.1. On the cathode side, A1 and A2 are circulated between the flow cell and reservoir, during charge process, A2 is first oxidized to A2*, then continuous redox-targeting cycles between A1 and active cathode (M) fulfill the charge transfer from A1* to M; while during discharge process, A1* is first reduced to A1, continuous redox-targeting cycles between A2*

and M^{x+} complete the electron transfer from A2 to M^{x+} .^[42-44] Similar process occurs on the anode side. While in the discharge process, it runs vice versa.

Wang and coworkers developed several flow battery systems based on redox-targeting reactions.^[40] A redox flow lithium battery with LiFePO_4 cathode and TiO_2 anode could reach a volumetric energy density of 500 Wh L^{-1} , but the applied current density is quite low (under 0.1 mA cm^{-2}).^[42] Redox-targeting lithium oxygen flow batteries have also been reported by Wang group.^[44,45] Nevertheless, the crossover of soluble redox mediators is still a big problem.

(c) Multiple ion exchange membranes based redox flow battery

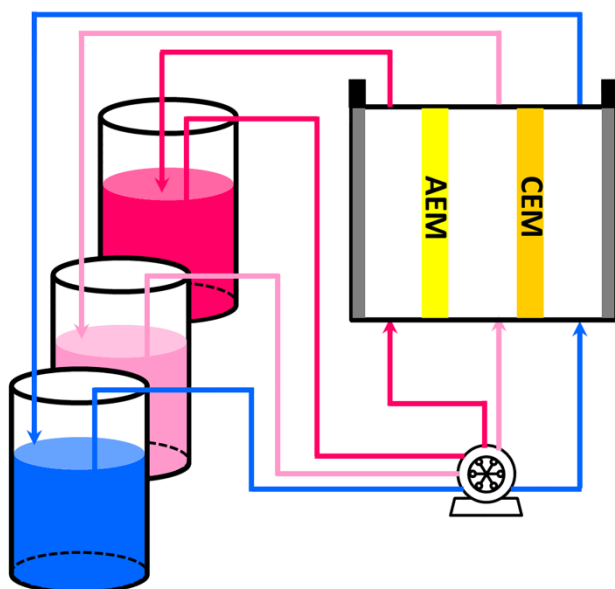


Figure 1.3 A scheme of multiple ion exchange membranes based redox flow battery.

Yan et al. put forward an innovative design with multiple ion exchange membranes for redox flow batteries.^[46,47] In contrast to traditional flow batteries, this flow battery system has three reservoirs for catholyte, anolyte and middle electrolyte, respectively. It utilizes CEM and AEM concurrently on the two sides of the middle chamber in the flow cell, to isolate the catholyte and anolyte from the middle electrolyte containing soluble chemical of A_xB_y , as illustrated in Figure 1.3. Cations of A^{a+} and anions of B^{b-} are served as charge carriers separately to complete the circuit. An aqueous zinc-cerium flow battery with a voltage of 3.0 V was realized, in which a NaCl solution

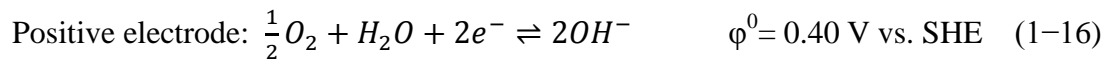
was used as the middle electrolyte. Afterwards, a low capital cost zinc–iron redox flow battery with a voltage of 2.0 V was also reported by Yan group.^[47] It is noteworthy that cross-contamination of the redox active species will still occur mainly in the middle reservoir, rather than in the catholyte reservoir or anolyte reservoir.

(d) Membrane-free flow battery

The high price of membranes hinders the massive commercialization of redox flow batteries. In a typical 4 MWh-scale VRFB, Nafion membrane accounts for 27% of the capital cost.^[10] Therefore, membrane-free flow batteries have been proposed in recent years.^[48-52] Cui et al. explored a membrane-free lithium/polysulfide semi-liquid battery, based on non-aqueous polysulfide catholyte and lithium metal anode. With 5 M Li₂S₈ catholyte, the energy density can achieve 97 Wh kg⁻¹ and 108 Wh L⁻¹, respectively.^[48] Taking advantage of an immiscible water-acetate system, aqueous zinc chloride and non-aqueous ferrocene in butyl acetate were used as anolyte and catholyte, respectively, to realize a membrane-less zinc–iron flow battery with a Columbic efficiency about 82%.^[51] Recently, similar research has been reported with a soluble all-iron flow battery.^[52]

(e) Metal–air flow battery

Rechargeable metal–air batteries, for instance, lithium–air batteries (LABs)^[53] and zinc–air batteries (ZABs)^[54] have drawn considerable attention over the past decades. The research on rechargeable ZABs becomes a hotspot owing to the high theoretical energy density (1086 Wh kg⁻¹ including oxygen), low cost and environmental benignity.^[55] During discharge process, the oxidation of zinc metal generates soluble zincate ions (i.e. Zn(OH)₄²⁻) which further decompose to insoluble zinc oxide (ZnO) at supersaturated Zn(OH)₄²⁻ concentration in the electrolyte.^[55,56] The redox reactions of ZABs with alkaline electrolytes are shown below:



Bockelmann and coworkers designed a rechargeable zinc–oxygen flow battery, with copper foam for zinc deposition, a commercial silver electrode and nickel foam for oxygen reduction and evolution, respectively. The cell could deliver a peak power density of 270 mW cm^{-2} , and continuously work for more than 600 cycles at 50 mA cm^{-2} .^[57] Heinzl et al. demonstrated a new zinc–air flow battery with different zinc-slurry compositions, in which zinc particles were suspended in alkaline solution (30 wt% KOH) and stabilized by polyacrylic acid, exhibiting discharge current densities higher than 4 kA m^{-2} .^[58] Comparing with ZABs, LABs have a higher working voltage ($2\text{Li}^+ + \text{O}_2 + 2e^- \rightleftharpoons \text{Li}_2\text{O}_2$, $\phi^0 = 2.96 \text{ V vs. Li}^+/\text{Li}$) and energy density (3458 Wh kg^{-1}).^[55] Soavi et al. introduced a semi-solid lithium–air redox flow battery, this proof-of-concept lithium–air flow battery demonstrated high discharge capacity ($>175 \text{ mAh cm}^{-2}$), energy density ($>500 \text{ mWh cm}^{-2}$) and power density ($>7 \text{ mW cm}^{-2}$).^[59]

1.3 Current progress and challenges of redox flow batteries

1.3.1 Typical active species for redox flow batteries

There are abundant redox active species for flow batteries, inorganic redox active species especially transition metal ions (e.g. $\text{Fe}^{3+}/\text{Fe}^{2+}$, $\text{V}^{3+}/\text{V}^{2+}$, Zn^{2+}/Zn) and halides are the main active species in early research of redox flow batteries.^[1,6] Representative redox active species are given in Figure 1.4. $\text{Fe}^{3+}/\text{Fe}^{2+}$ active species and their complexes (e.g. ferricyanide and ferrocyanide) are dominant inorganic active species for positive electrolyte due to the stability and low cost.^[60-62] Tremendous efforts have been made to achieve high energy density and mitigate against crossover through optimization of redox behavior of metal ions with ligands and additives.^[62] Glycine is a suitable ligand to stabilize $\text{Fe}^{3+}/\text{Fe}^{2+}$ ions to alleviate crossover and prevent $\text{Fe}^{3+}/\text{Fe}^{2+}$ ions from precipitation.^[1,23,63] Wen et al. investigated the redox behavior of $\text{Fe}^{3+}/\text{Fe}^{2+}$ ions with different ligands, e.g. ethylenediaminetetraacetic acid (EDTA), citrate and oxalate to shift the redox potentials to negative potential.^[64] The Fe (III)/(II)–TEA complex showed reversible

redox peaks at -1.0 V (vs. saturated calomel electrode, SCE) to be alternative negative active species,^[65] then an all-soluble all-iron aqueous redox flow battery was reported when paired with sodium ferricyanide and ferrocyanide.^[62]

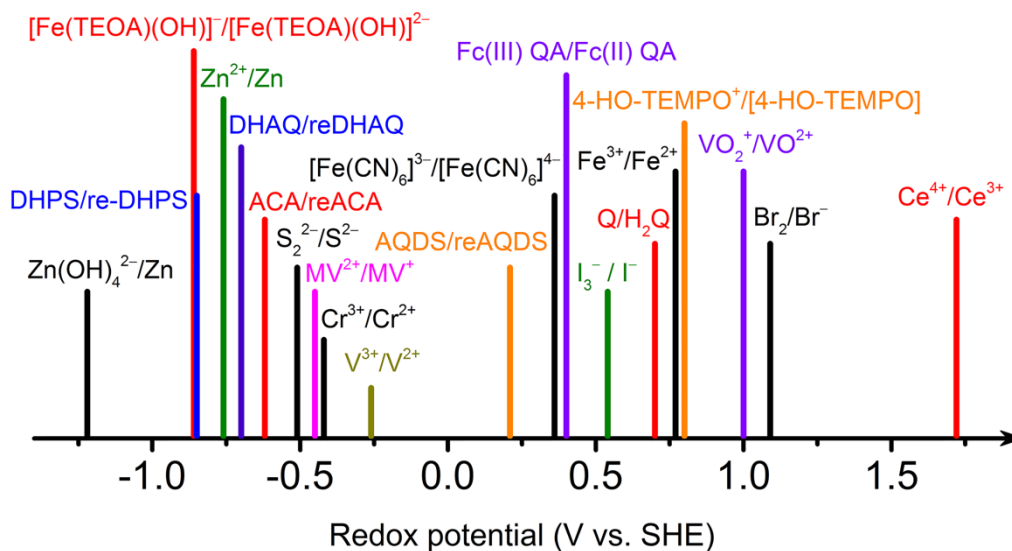


Figure 1.4 Redox potentials of active species versus standard hydrogen electrode (SHE). Abbreviations: 7,8-dihydroxyphenazine-2-sulfonic acid (DHPS); triethanol-amine (TEOA); 2,6-dihydroxyanthraquinone (DHAQ); alloxazine 7/8-carboxylic acid (ACA); methyl viologen (MV); 9,10-anthraquinone-2,7-disulfonic acid (AQDS); ferrocene (Fc); quaternary ammonium salts (QA); 1,4-benzoquinone/p-hydroquinone (Q/H₂Q); 4-hydroxy-2,2,6,6-tetramethylpiperidin -1-oxyl (4-HO-TEMPO).

Polyoxometalates (POMs) have structural diversities, large sizes and multi-electron redox properties, showing great potential in flow batteries.^[66-68] Tungsten-based POMs are attractive because they could be synthesized in high yield and high purity with relatively low-cost precursors.^[66] A tungsten-cobalt heteropolyacid (H₆[CoW₁₂O₄₀]) based aqueous electrolyte has been reported both as catholyte and anolyte for redox flow battery to address crossover.^[69] This flow battery exhibited an energy efficiency of 86% and an energy density of 15.4 Wh L⁻¹ with a voltage of ~ 1.1 V. Recently Cronin and colleagues reported a polyoxoanion [P₂W₁₈O₆₂]⁶⁻, which can be reversibly reduced and protonated by 18 electrons/H⁺ per anion in an aqueous solution.^[68] When paired with HBr/Br₂ based catholyte, it presented an ultrahigh discharge capacity of 230 Ah L⁻¹ and an energy density of 225 Wh L⁻¹.

However, there are limited choices of soluble inorganic redox active species,

organic redox active species are suggested to be new alternatives.^[7,70-75] Quinones,^[60,76] organometallic compounds,^[42,77-79] 2,2,6,6-tetramethylpiperidine-1-oxyl (TEMPO) derivatives,^[80-82] viologens^[16,77] and phenazines^[83] are prevalent active species for organic redox flow batteries. The molecular diversities of organic compounds enrich the battery chemistries for RFBs, and further accelerate the development of RFBs.^[7,71] Molecular modifications have been proposed to increase the solubility and tune the redox potentials of organic species in the corresponding supporting electrolytes.^[13,84,85] Nevertheless, the possible side reactions of organic active species during charge/discharge process result in capacity decay over cycles.^[86]

Quinone based organic molecules are promising active materials owing to the fast electron transfer properties and molecular diversities.^[13,60,87,88] Computational strategy facilitates the screening process of quinone and hydroquinone derivatives to rationally design quinone based flow batteries.^[76] Para-hydroquinone (p-H₂Q),^[89] ortho-hydroquinone (o-H₂Q)^[90,91] and their sulfonate derivatives (molecular structures in Figure 1.5a) are reported for aqueous organic RFBs. Anthraquinone (AQ) derivatives were systematically studied for flow batteries. Aziz et al. reported a metal-free organic–inorganic aqueous flow battery, 9,10-anthraquinone-2,7-disulfonic acid (AQDS) was dissolved in sulfuric acid as anolyte, a HBr/Br₂ solution was used as catholyte, this flow battery exhibited unprecedentedly high power density of 0.6 W cm⁻² at 40 °C.^[13] They also suggested a new pathway to tune the redox potentials and solubilities of redox organic molecules by introducing functional groups. A RFB with 2,6-dihydroxyanthraquinone (2,6-DHAQ) based anolyte and ferrocyanide based catholyte presented an energy efficiency of 84% over 100 cycles at 100 mA cm⁻².^[60]

Organometallic compounds are special redox representatives, in which redox active metal ions are coordinated with organic species to form stable compounds. Metallocenes are typical organometallic compounds which have similar molecular structures, two cyclopentadienyl rings are bounded on opposite sides of a central metal atom.^[79,92] Cobaltocene (CoCp₂) and ferrocene (FeCp₂ or Fc) as well as their derivatives have been utilized as redox active species for non-aqueous RFBs.^[79,93] An all-metallocene-based, non-aqueous RFB was reported with FeCp₂ cathode and

CoCp₂ anode to show a voltage of 1.7 V and an energy efficiency above 85%.^[79] Wang et al. proposed a flow battery with CoCp₂ based on redox-targeting reactions,^[42] details can be found in chapter 1.2.5b. Lu and coworkers reported 1,1-dimethylferrocene (DMFc) in non-aqueous solution and paired with lithium metal to achieve a high volumetric capacity of ~68 Ah L⁻¹ based on catholyte.^[94] To address the crossover of metallocene in non-aqueous electrolytes, Stimming et al. prepared metallocene derivatives grafting on fullerene, which were found to be soluble in various organic solvents for non-aqueous RFBs.^[95] Ionic modification has been proposed to increase the solubility of ferrocene derivatives. Wang et al. found that after functionalization with an ionic charged tetraalkylammonium pendant arm with a bis(trifluoromethanesulfonyl)imide counter anion, the solubility was improved by 20 times in carbonate solvents.^[84]

On account of the poor solubility of metallocenes in aqueous solutions, quaternary ammonium groups are introduced to improve the solubility (Figure 1.5b). Liu et al. synthesized highly water-soluble ferrocene derivatives (Figure 1.5b (i) and (ii)), (ferrocenylmethyl)trimethylammonium chloride (FcNCl, 4.0 M in H₂O, 3.0 M in 2.0 M NaCl) was used as cathode material and paired with MV anode to build a neutral aqueous RFB.^[77] This organic RFB revealed a long life over 700 cycles with capacity retention of 91% and a Coulombic efficiency of 99% at 60 mA cm⁻². Afterwards Aziz et al. reported a similar ferrocene derivative, bis((3-trimethyl-ammonio)-propyl)-ferrocene dichloride (BTMAP-Fc), as shown in Figure 1.5b (iii), with quaternary ammonium groups on both cyclopentadienyl rings to enlarge the molecular size.^[78] Although the concentration decreased to 1.9 M in H₂O, unprecedented capacity retention of 99.9943%/cycle and 99.90%/day was achieved at a reactant concentration of 1.3 M. The calendar life was estimated up to 14 years, with 50% of its energy storage capacity remained, thus to meet the practical requirement for grid-scale flow batteries, which usually have long lifespan about 10 years.

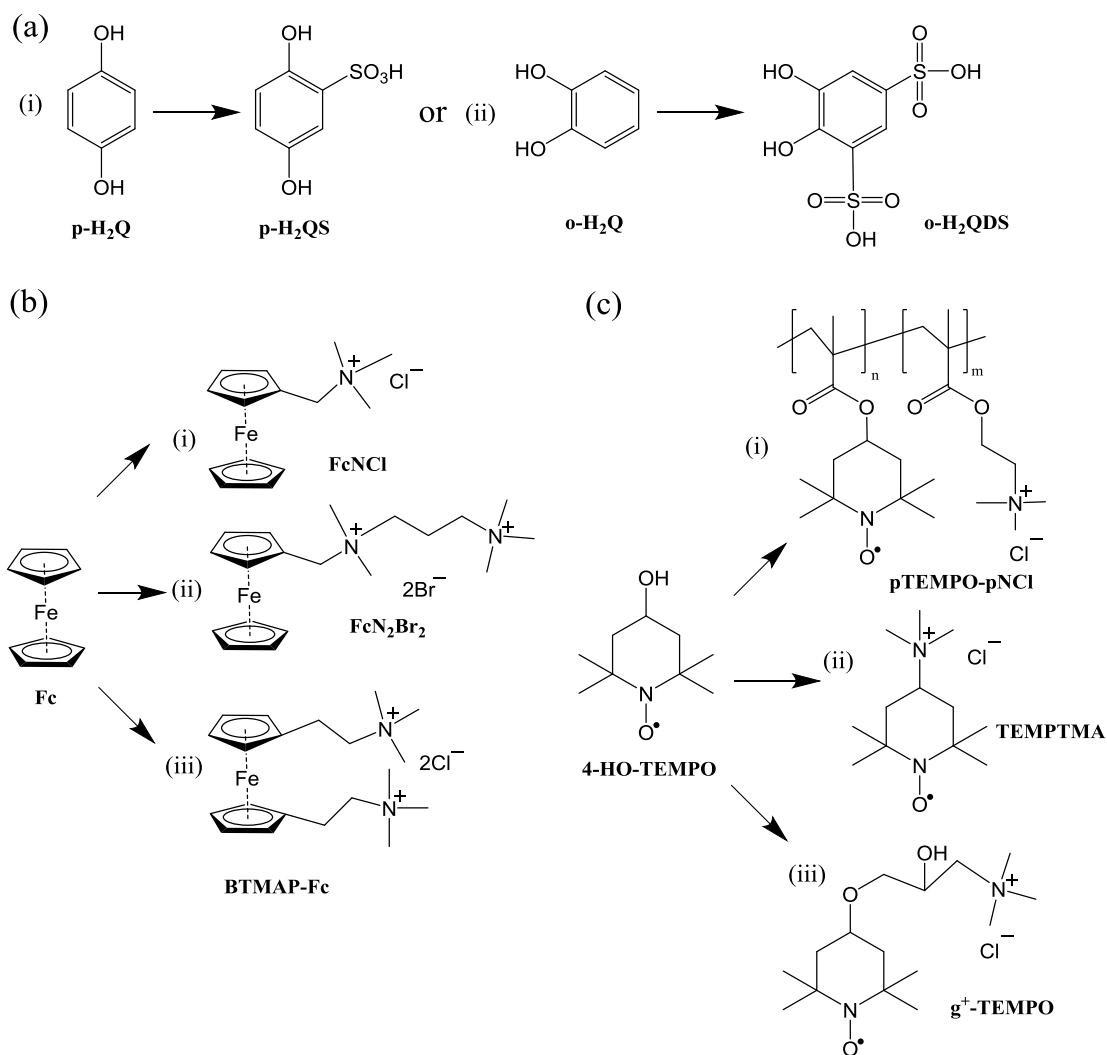


Figure 1.5 Molecular modifications of (a) para-hydroquinone ($p\text{-H}_2\text{Q}$) and ortho-hydroquinone ($o\text{-H}_2\text{Q}$); (b) ferrocene (Fc) and the corresponding derivatives, FcNCl and FcN_2Br_2 (Ref. [77]), BTMAP-Fc (Ref. [78]); (c) 4-HO-TEMPO and the corresponding derivatives, $p\text{TEMPO-pNCl}$ (Ref. [81]), TEMPTMA (Ref. [82,96]) and $g^+\text{-TEMPO}$ (Ref. [15]).

TEMPO and its derivatives have high redox activity and reversibility at positive potential (vs. SHE), making them promising candidates for catholyte.^[16,80] Schubert and coworkers demonstrated a polymer-based redox flow battery, in which TEMPO based polymer ($p\text{TEMPO-pNCl}$ in Figure 1.5c (i)) and viologen based polymer were dissolved in aqueous NaCl solution and used as catholyte and anolyte, respectively, a piece of dialysis membrane was adopted as the separator.^[81] This flow battery showed an average Coulombic efficiency of 97% and capacity retention of 80% over 100 cycles at 40 mA cm^{-2} . Due to the low concentration of 4-HO-TEMPO ($\sim 0.5 \text{ M}$ in 1.0

M of aqueous NaCl solution), it was sulfonated by concentrated sulfuric acid and then neutralized with KHCO_3 to prepare TEMPO-4-sulfonate potassium salt.^[97] This sulfonated TEMPO derivative is oxygen-insensitive and can reach a concentration above 1.0 M. Molecular modifications of TEMPO and its derivatives (TEMPTMA and g^+ -TEMPO in Figure 1.5c (ii) and (iii)) have also been reported by introduction of quaternary ammonium groups.^[15,82,96] These researches open new avenues to develop low-cost and non-corrosive aqueous flow batteries.

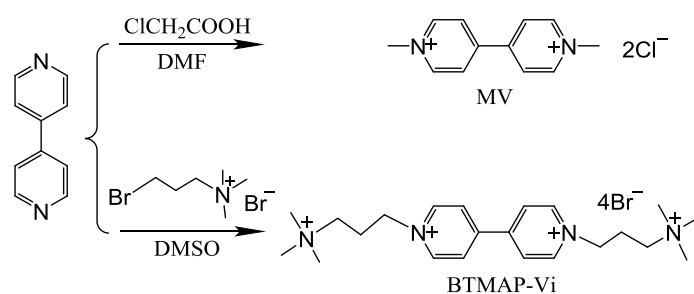


Figure 1.6 Synthesis routes of viologens (top: MV, Ref.^[82]) and its two-electron-reaction derivative (bottom: viologen derivative, Ref.^[78,98]).

Viologens, for instance, benzyl viologen (BV), ethyl viologen (EV), heptyl viologen (HV) and methyl viologen (MV, warning: MV is extremely toxic!) are a group of highly water-soluble redox organics.^[99] A representative synthesis route of viologens is shown in Figure 1.6. Liu and Wang et al. reported a total organic aqueous redox flow battery (OARFB), employing MV anolyte and 4-HO-TEMPO catholyte in NaCl supporting electrolyte. This flow battery with 0.5 M redox active species showed a high Coulombic efficiency of $\sim 100\%$ and capacity retention of 89% over 100 cycles.^[16] MV and its various derivatives were synthesized by Schubert et al.^[82] and Liu et al.^[98] independently. When paired MV with TEMPTMA (N,N,N,2,2,6,6-heptamethylpiperidinyloxy-4-ammonium chloride), the flow battery exhibited an energy efficiency of 70% and capacity retention of 99% over 100 cycles at 80 mA cm^{-2} .^[82] Owing to the insolubility of the neutral-charge-state MV^0 in aqueous solution, MV takes one-electron reaction in flow battery.^[98] Quaternary ammonium groups were introduced to the molecular chains of viologens to liberate the other electron, thus enable a two-electron redox reaction of viologens.^[96,98,100]

Besides quinones, metallocenes, TEMPO derivatives and viologens, alloxazine^[74] and phenazine^[83] as well as imide derivatives^[85] have also been reported as organic redox active species for high-performance RFBs.

1.3.2 Liquid media for redox flow batteries

Water and organic solvents are universal liquid media for RFBs. Aqueous electrolytes based RFBs are non-flammable, cost-effective and feasible, but suffer from low voltage due to the narrow electrochemical stability window (ESW) of water (thermodynamically 1.23 V), as well as risk of hydrogen evolution and/or oxygen evolution during operation;^[13] non-aqueous electrolytes based RFBs enable high voltage, but they are usually moisture-sensitive, volatile and flammable.^[85,101] However, either deionized water or conventional organic solvents (e.g. carbonates, acetonitrile) is ion-conductive, supporting conductive additives are usually required for the electrolytes. Brushett and coworkers demonstrated a supporting-salt-free non-aqueous RFB, in which the redox ionic species exhibited high conductivities in acetonitrile (12~19 mS cm⁻¹).^[102]

If redox active species are liquid state at room temperature, only slight solvent and conductive additives are needed to dilute them in case of being viscous rather than dissolve them with certain amount of solvent, thus increase the concentration obviously. For the first time, Zhang et al. presented a room-temperature liquid-state catholyte with an organic redox active molecule, 2,5-di-*tert*-butyl-1,4-bis-(2-methoxyethoxy)benzene (DBBB) was incorporated with poly ethylene oxide (PEO) chains to get liquid-state redox active species.^[103] The ideal goal is to use liquid redox active species as electrolytes directly in the absence of solvents, since the “concentration” could be quite high. Fontaine et al. synthesized liquid-state biredox ionic liquids, combining AQ and TEMPO based molecules, to build supercapacitors with an energy density of 70 Wh kg⁻¹ and a working voltage of 2.8 V.^[104] Almost at the same time, similar research results have also been reported for organic RFBs based on poly(ionic liquid)s, combining AQ and TEMPO redox active molecules.^[105] These reports provide new pathways for the development of RFBs.

Ionic liquids and deep eutectic solvents (DESs) are considered as alternative liquid media since they are usually non/low-toxic and non-volatile, and they have high ignition points for safety concern.^[50,106,107] Details will be introduced in chapter 1.4.

1.3.3 Current issues for redox flow batteries

Despite plentiful achievements in the development of RFBs over past decades, there are still some tough issues. For instance, in the prevalent VRFBs and ZBFBs, vanadium compounds and halogen have risk of toxicity; the possibly corrosive electrolyte brings environmental concerns; Nafion membranes remain high price if being adopted. Nevertheless, the main challenges of current RFBs are the low energy density and crossover of electrolytes during operation. The energy density of a RFB is dependent on the electrolytes, as shown in equation 1–20:

$$E = \frac{(\varphi_c - \varphi_a)F}{\frac{1}{n_c C_c} + \frac{1}{n_a C_a}} \quad (1-20)$$

where φ_c and φ_a are the redox potentials of active species in catholyte and anolyte, respectively, F is Faraday constant ($96,485 \text{ C mol}^{-1}$), n_c and n_a are the electron transfer numbers in redox reactions of catholyte and anolyte, respectively, C_c and C_a are the concentrations of active species in catholyte and anolyte, respectively.

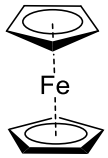
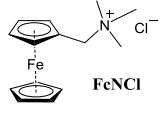
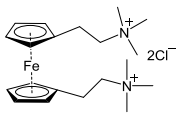
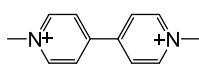
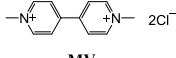
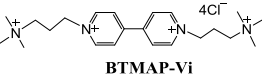
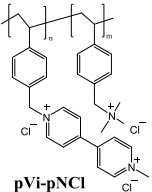
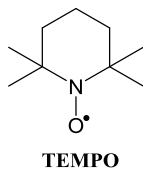
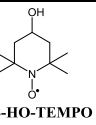
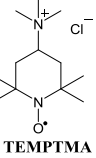
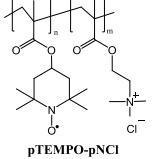
Therefore, there are mainly three pathways to increase the energy density of a RFB:

- broaden the redox potential gap of active species in catholyte and anolyte,^[32,46,47]
- develop redox active species involving more transferred electrons in half reactions (n_c and n_a);^[68]
- increase the concentration of redox active units in catholyte and anolyte (C_c and C_a). Note: suppose one redox active molecule (RAM) contains k (number) redox active units (RAU), then $C_{RAU} = k * C_{RAM}$ ^[25].

Crossover of the electrolytes is responsible for the capacity loss during charge/discharge, which causes contamination of the active species. Generally, prevention of crossover is relied on electrostatic charge repulsion from the polymeric backbones of ion exchange membranes (IEMs). However, there are nanochannels in the IEMs which are available for the slow permeability of redox active species owing to osmotic pressure during circulation. Nafion, a commercial CEM with high stability,

is reported to have nanochannels with an average diameter around 2 nm by simulation^[14] and experimental study,^[108] depending on the specific models. Commercial AEMs, e.g. Selemion, a chloride-ion-conducting membrane produced by AGC chemicals (Japan), has an average pore size of 1 nm.^[16,77]

Table 1.2 Molecular modifications of active species for redox flow batteries.

Redox active species	Modified redox molecules	RFBs and capacity retention	References
 Fc (+)	(m1)  FcNCl	0.5 M (m1) vs. 0.5 M (m4); ~91% after 700 cycles	J. Am. Chem. Soc., 2017, 139, 1207–1214.
	(m2)  FcN₂Br₂	0.5 M (m2) vs. 0.5 M (m4); long-cycle test is not reported	J. Am. Chem. Soc., 2017, 139, 1207–1214.
	(m3)  BTMAP-Fc	1.3 M (m3) vs. 1.3 M (m5); ~98.5% after 250 cycles	ACS Energy Lett., 2017, 2, 639–644.
 MV (-)	(m4)  MV		
	(m5)  BTMAP-Vi		
	(m6)  pVi-pNCl		
 TEMPO (+)	(m7)  4-HO-TEMPO	0.5 M (m7) vs. 0.5 M (m4); ~89% after 100 cycles	Adv. Energy Mater. 2016, 6, 1501449
	(m8)  TEMPTMA	2.0 M (m8) vs. 2.0 M (m4); ~99% after 100 cycles	Angew. Chem. Int. Ed. 2016, 55, 14427–14430.
	(m9)  pTEMPO-pNCl	(m9) vs. (m6); ~80% after 100 cycles (utilization of simple dialysis membranes)	Nature, 527, 78–81.

Appropriate ligands have been sought to mitigate against crossover of inorganic

metal ions, as discussed before, glycine and triethanolamine have been used to alleviate diffusion of $\text{Fe}^{3+}/\text{Fe}^{2+}$ ions.^[23,62,63] Molecular modifications are found to be effective approaches to alleviate crossover of organic active species. Figures 1.5 and 1.6 show some examples of modification of organic redox molecules. As the molecular sizes are enlarged, it becomes more difficult for the active species to diffuse through the nanochannels in a membrane to the counterpart to cause crossover, thus realize high capacity retention.^[77,78,109] As shown in Table 1.2, for a given redox active molecule, when the molecular size is enlarged to some extent, the capacity retention could be satisfactory. Consequently, there should be a compromise between molecular size and concentration for redox active species, to achieve high energy density as well as high capacity retention.

Several representative methods are summarized here to mitigate against crossover:

- (a) utilize (i) sole-element-based positive and negative active species which can transform mutually if crossover happens, and (ii) same supporting electrolyte in catholyte and anolyte, e.g. all vanadium redox flow batteries (chapter 1.2.1), all iron flow battery^[1];
- (b) mix positive and negative active species in the same supporting electrolyte to serve both as catholyte and anolyte for symmetric RFBs,^[27,29,101] e.g. Fe/V RFB, Fe/Cr RFB (chapter 1.2.2);
- (c) use one active unit contains both positive and negative active species for symmetric RFBs, e.g. (i) zinc-halogen flow battery (chapter 1.2.3); (ii) organic species with [A-R-C] structures, in which positive active species C and negative active species A are grafted on the same molecular chain (R),^[110-112]
- (d) size exclusion effect: $r_A < r_B < r_C$, where r_A , r_B , r_C are the radius of charge carrier, pore size of membrane and radius of active species, respectively;^[12,113]
- (e) utilize ion-conducting ceramic membranes,^[79,107] e.g. LISICON or NASICON membranes rather than polymer-based membranes.

Nevertheless, there are only a few suitable battery chemistries for method (a). While in method (b) and (c), crossover is addressed at the sacrifice of capacity which could be reduced to half, since the positive redox active species in anolyte contribute

little to capacity of RFBs, neither do negative redox active species in catholyte. Method (d) can be effective if polymeric redox active species are utilized, but the concentration may be quite low. Moreover, the ion-conducting ceramic membranes used in method (e) are quite expensive and not as flexible as polymer-based membranes, and the applied current densities are too low for practical application. Therefore, overall consideration should be taken when tackle with the crossover issues in specific RFBs.

1.4 Ionic liquids and their applications in redox flow batteries

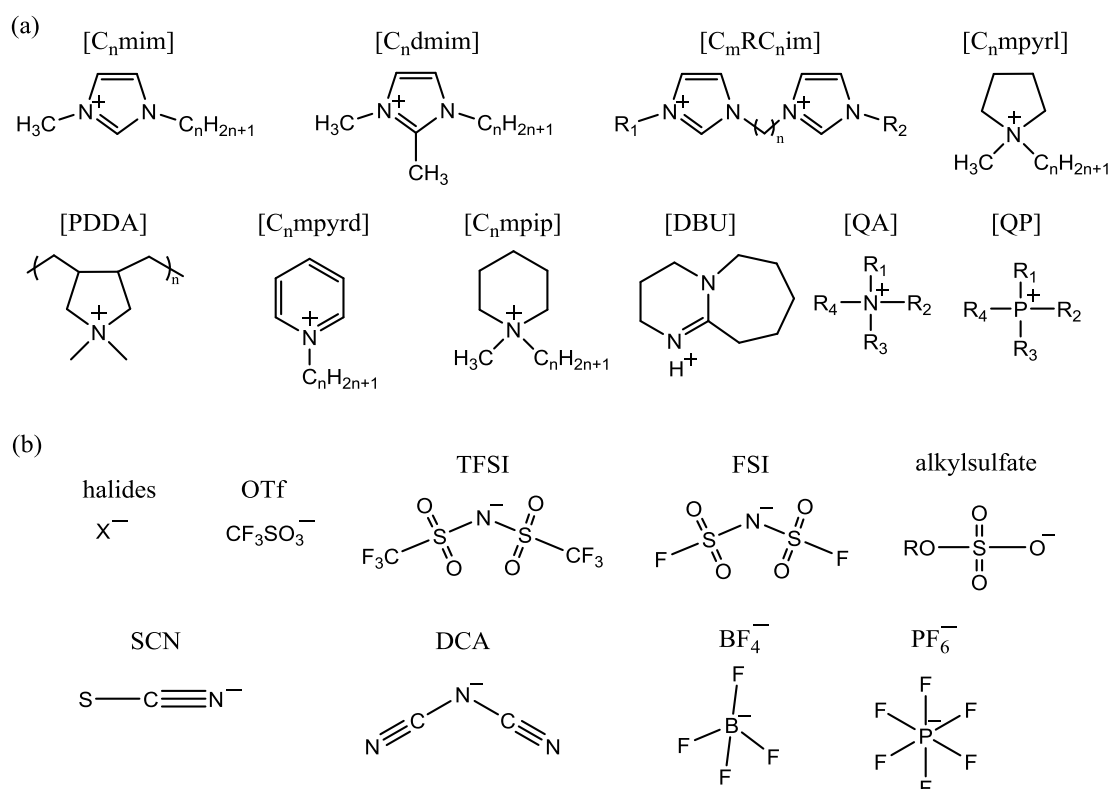


Figure 1.7 Representative (a) cations and (b) anions of ionic liquids. Abbreviations: PDDA (poly dimethyl diallyl ammonium); DBU (1,8-di-aza bicyclo-[5.4.0]undec-7-ene); QA (quaternary ammonium); QP (quaternary phosphonium); OTf (trifluoromethanesulfonate, triflate); TFSI (bis(trifluoromethane)sulfonylimide); FSI (bis(fluorosulfonyl)imide); DCA (dicyanamide).

Ionic liquids (ILs) are defined as molten salts with melting points lower than

100 °C. They are formed by discrete cations and anions, some typical cations (imidazolium, pyrrolidinium, pyridinium, quaternary salts etc.) and anions (halides, triflate, bis(trifluoromethane)sulfonimide etc.) of ILs are given in Figure 1.7.^[114,115] The first IL, ethylammonium nitrate (EAN) was reported in 1914 by Walden.^[116] It is worth mentioning here that deep eutectic solvents (DESs) are now widely recognized as IL analogues, since they have many similar properties with ILs. However, DESs are homogeneous eutectic mixtures of Lewis or Brønsted acids and bases which can contain various anionic and/or cationic groups.^[117]

ILs are widely used as reaction media, lubricants and heat-transfer fluids due to their non/low-toxicity, non-flammability, low vapor pressure and high thermal stability.^[118] The unique dissolution capability makes them promising alternatives to water and conventional organic solvents, for instance, cellulose is non-meltable and non-soluble in conventional solvents owing to its highly ordered structure and strong hydrogen bonding networks, but it can achieve a concentration up to 10 wt% in 1-butyl-3-methylimidazolium chloride (BMImCl) and even higher to 25 wt% under microwave heating.^[119] Moreover, water-sensitive metals and semiconductors which cannot be electroplated from aqueous electrolytes can be realized in ILs.^[120,121] Therefore, the advent of ILs accelerates the research progress on liquid/fluid chemistry and electrochemistry.

Considering the ion-conductive properties and wide ESWs, ILs have also shown remarkable potential as electrolytes in electrochemical applications,^[120] such as fuel cells,^[120] membranes,^[114] electrodeposition,^[122,123] supercapacitors^[104] and batteries.^[121] Particularly, ILs are universally conductive additives for non-aqueous electrolytes. Nevertheless, many ILs exhibit high viscosities even some of them are liquids at room temperature, therefore, ILs are usually dissolved/diluted with water or organic solvents as supporting electrolytes for RFBs.^[124-126] Besides, ILs are also adopted to dissolve organic and inorganic redox active species^[126,127] and regulate the redox behavior of active species.^[128,129]

To explore the application of ILs in redox flow batteries, Walsh et al. investigated the redox behavior of metal acetylacetonate (acac) complexes in room-temperature

ILs, $V(\text{acac})_3$ showed multi reversible redox peaks both in positive and negative potential regions in imidazolium based ILs. A symmetric RFB was tested in a static H-type cell with a Coulombic efficiency of 72%.^[124] Takechi and colleagues reported a solvated IL for RFB, 4-methoxy-2,2,6,6-tetramethylpiperidine-1-oxyl (MeO-TEMPO) was mixed with lithium bis(trifluoromethanesulfonyl)imide (LiTFSI) to form a concentrated non-aqueous catholyte, realizing a concentration over 2 M and low viscosity after being diluted by slight acetonitrile.^[127] Most ILs with TFSI anions have the nature of superior hydrophobicity, therefore, fluid dynamic engineering techniques can be applied to maintain a laminar flow to form an aqueous/non-aqueous biphasic system, thus minimize the mixture of the electrolytes. Marcilla et al. designed a prototype of membrane-free RFB based on immiscible aqueous solution and hydrophobic IL.^[50] Hydroquinone (H_2Q) in 0.1 M HCl was used as aqueous catholyte, while para-benzoquinone (pBQ) in hydrophobic 1-butyl-1-methylpyrrolidinium bis(trifluoromethanesulfonyl)imide ($\text{PYR}_{14}\text{TFSI}$) was used as non-aqueous anolyte. The proof-of-concept flow battery has an open circuit voltage (OCV) of 1.4 V, and a theoretical energy density of 22.5 Wh L^{-1} .

1.5 Scope of this thesis

The past few decades have witnessed the commercial progress of VRFBs and ZBFBs in the United States, European countries, China, Australia and some other countries. However, the drawbacks of toxicity, high capital cost and corrosion of the electrolytes slow down their universal deployment. Considering the urgent demand and huge market for highly efficient energy storage technologies, as well as unique advantages of RFBs, it is of significant desire to develop new RFB systems with low cost, high safety and high performance.

The overall development and investigation of electrolytes, membranes and electrode materials for RFBs could be a huge and challenging task, since RFBs are complicated battery systems. Therefore, the primary research in this thesis focuses on the development of electrolytes as well as screening of appropriate ion exchange

membranes for the newly developed RFB systems. Although there are initial trials and reports of ILs based electrolytes for RFBs, the potential of ILs in RFBs is still under further exploration, so it is quite necessary to investigate the application of ILs in RFBs.

To make the research more efficient, this thesis mainly introduces aqueous electrolytes for RFBs. There are numerous ILs as reported hitherto. Hydrophilic ILs are screened initially according to the public literature and the available information from chemical suppliers. In Chapter 3, six representative ILs are selected to prepare aqueous electrolytes, the interaction between water and cation/anion groups of ILs on the influence of electrochemical stability windows as well as ionic conductivities etc. is characterized. An aqueous titanium dioxide–iron (II) chloride hybrid battery is proposed accordingly. In Chapter 4, Fe-based and Zn-based redox active species are selected as active species to prepare electrolytes to build an aqueous zinc–iron hybrid flow battery, the compositions of catholyte and anolyte are regulated and optimized. Kinetic analyses are conducted to investigate the redox activity of $\text{Fe}^{3+}/\text{Fe}^{2+}$ active species as well as zinc plating/stripping process. In Chapter 5, an organic–inorganic hybrid flow battery is designed with hydroquinone and zinc species, in which the concentration of hydroquinone can be increased by eight folds to achieve ultrahigh energy density.

2 Characterization methods

2.1 Physical properties

The physical properties of electrolytes (e.g. ionic conductivity and viscosity) are of great importance for the performance of RFBs. Most ILs have low ionic conductivities and high viscosities, which are detrimental for RFBs. Herein, ionic conductivities are measured by a WTW Cond 3110 conductivity meter (Xylem, Germany) with a TetraCon® 325 cell. Before the ionic conductivity measurements, the conductivity meter is calibrated with a reference solution ($0.01 \text{ mol L}^{-1} \text{ KCl}$) provided by the supplier. For each test, the ionic conductivities are recorded five times to get an average value. The rheological properties of electrolytes are tested by a MCR 301 rheometer (Anton Paar GmbH, Graz, Austria) equipped with a DD41 dish (diameter: 41 mm) and a PP25 measuring plate (diameter: 25 mm). For each sample, 30 viscosity data are recorded to get an average value.

2.2 Anodic oxidation

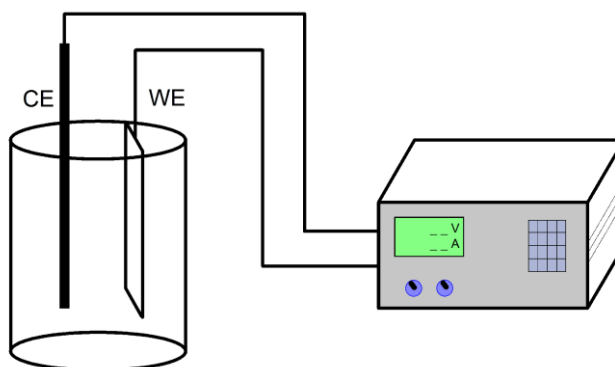


Figure 2.1 Scheme of anodic oxidation.

Anodic oxidation is a facile technique to fabricate active layer on the surface of metal foils. In a typical setup for anodic oxidation in Figure 2.1, a DC power supply is

connected with a two-electrode system, in which the working electrode (WE, e.g. Al foil or Ti foil) and counter electrode (CE, graphite or platinum) are immersed in the electrolyte. During anodic oxidation, the working electrode can be electrochemically corroded. Anodic aluminium oxide (AAO) and anodic titanium oxide (ATO) nanoarrays can be prepared by anodic oxidation according to previous reports.^[130-132] Two-step anodic oxidation methods have been further developed to prepare highly ordered ATO and AAO nanoarrays.^[132] In this thesis, feasible anodic oxidation is used to prepare ATO as an ion host, to exploit the initial application of electrochemical stability windows of aqueous ionic liquid solutions.

2.3 Electrochemical tests

2.3.1 Electrochemical impedance spectroscopy

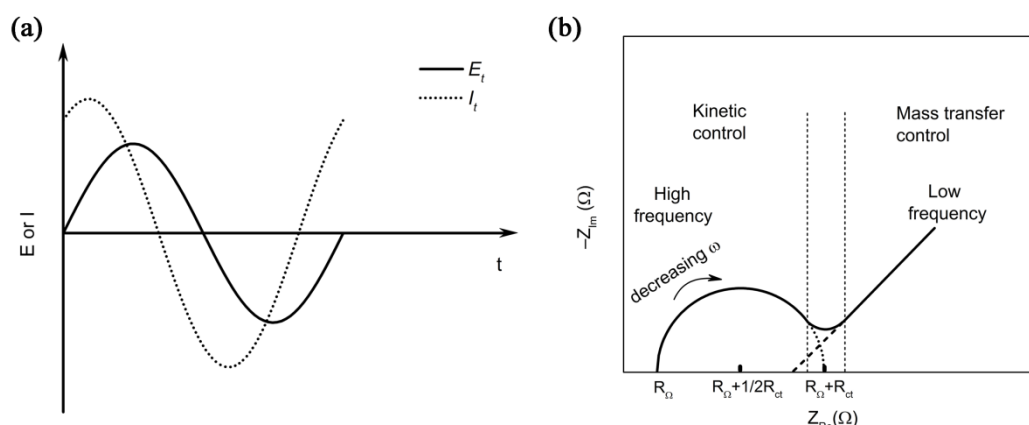


Figure 2.2 (a) Relationship between the alternating voltage signal and response current, (b) typical Nyquist plot.

Electrochemical impedance spectroscopy (EIS) is widely used in anodic corrosion, electroplating, batteries and fuel cells etc. EIS is a perturbative characterization of the dynamics process in an electrochemical cell. When a sinusoidal excitation signal (E_t) with a small amplitude (~ 10 mV) is applied on the cell, a response current signal (I_t) appears accordingly, generally with a shifted phase angle (ϕ), as shown in Figure 2.2a.

$$E_t = E_0 \sin(\omega t) \quad (2-1)$$

$$I_t = I_0 \sin(\omega t + \phi) \quad (2-2)$$

where E_t is the voltage at time t , E_0 is the voltage amplitude of the signal, ω is the angular frequency ($\omega = 2\pi f$, f is the conventional frequency in Hz), I_t is the response current at time t , I_0 is the current amplitude.

In a vector diagram, it is convenient to represent phasors in terms of complex notation. The general presentation of impedance is given in equation 2-3.

$$Z(\omega) = Z_{Re} + jZ_{Im} \quad (2-3)$$

Note: here we take a usual definition of impedance, different with the equation in Allen Bard's book,^[133] in which it is $Z(\omega) = Z_{Re} - jZ_{Im}$.

where $j = \sqrt{-1}$, Z_{Re} and Z_{Im} are the real and imaginary parts of the impedance, respectively, a typical Nyquist plot is shown in Figure 2.2b. The Nyquist plot displays Z_{Im} vs. Z_{Re} at the corresponding values of ω , R_Q is the series resistance of the whole equivalent circuit, including the resistance of electrolyte, separator, surface films and leads in an electrochemical cell which is connected to the testing system, R_{ct} is the charge transfer resistance. The slope line in the low frequency region is associated with the Warburg impedance. At high frequencies, the Warburg impedance is quite small as diffusion of reactants cannot influence the current at such short time period; while at low frequencies, the reactants have to diffuse farther, thus increasing the Warburg impedance.^[133]

2.3.2 Cyclic voltammetry

Cyclic voltammetry (CV) is used to investigate the electron transfer process and redox behavior of the electrochemical reactions. In CV measurements, the potential of electrode increases (or decreases) linearly versus time in a potential range during the forward scan, then switches to backward scan to finish a cycle. The responses of current peaks reflect the redox reactions in an electrochemical cell. To diagnose a Nernstian reaction, the peak separation ΔE_p is always close to $\frac{2.3RT}{nF}$ (equation 2-4).^[133], E_{pa} and E_{pc} are the redox potentials in anodic and cathodic process, respectively.

$$\Delta E_p = |E_{pa} - E_{pc}| = \frac{2.3RT}{nF} \quad (2-4)$$

According to Randles–Sevcik equation, in a Nernstian system,

$$i_p = 0.4463 \left(\frac{F}{RT}\right)^{1/2} F n^{3/2} A D_0^{1/2} C_0 v^{1/2} \quad (2-5)$$

whereas in an irreversible system,

$$i_p = 0.4958 \left(\frac{\alpha F}{RT}\right)^{1/2} F n^{3/2} A D_0^{1/2} C_0 v^{1/2} \quad (2-6)$$

$$|E_p - E_{p/2}| = \frac{1.857RT}{\alpha nF} \quad (2-7)$$

where i_p is the peak current, F is Faraday constant (96,485 C mol⁻¹), R is the universal gas constant (8.314 J K⁻¹ mol⁻¹), T is the absolute temperature (298.15 K), n is the number of transferred electrons, A is the active area of the electrode (cm²), D_0 is the diffusion coefficient of redox active species (cm² s⁻¹), and C_0 is the concentration of redox active species (mol cm⁻³), v is the scan rate (V s⁻¹), α is the charge transfer coefficient, E_p is the potential of the peak, $E_{p/2}$ is the half-peak potential (potential at $i_p/2$).

2.3.3 Galvanostatic charge/discharge test

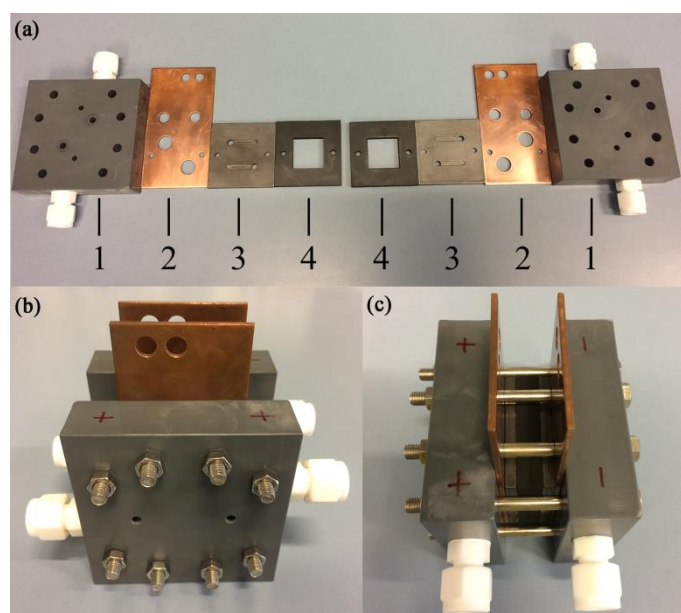


Figure 2.3 A laboratory-scale flow cell, (a) components, 1. end plate, 2. copper current collector, 3. graphite bipolar plate, 4. gasket; (b) front view and (c) top view of an assembled flow cell.

Galvanostatic charge/discharge test is commonly used to evaluate the electrochemical performance of rechargeable batteries. Figure 2.3 shows a typical laboratory-scale flow cell for charge/discharge test, inlets and outlets are connected with flowing channels in the end plates, copper plates are used as current collectors, graphite bipolar plates are drilled with serpentine flowing field, and corrosive-resistant gaskets are used to hold the electrodes.

The Coulombic efficiency (CE), voltage efficiency (VE), and energy efficiency (EE) can be calculated according to the following equations:

$$CE = \frac{\int_0^{t_1} I_{dis} dt}{\int_0^{t_2} I_{ch} dt} \times 100\% \quad (2-8)$$

$$VE = \frac{\bar{E}_{dis}}{\bar{E}_{ch}} \times 100\% = \frac{\frac{\int_0^{t_1} E_{dis} dt}{t_1}}{\frac{\int_0^{t_2} E_{ch} dt}{t_2}} \times 100\% \quad (2-9)$$

$$EE = CE \times VE \quad (2-10)$$

where I_{dis} and I_{ch} are the discharge current and charge current at time t , respectively; t_1 and t_2 are the discharge time and charge time, respectively; \bar{E}_{dis} and \bar{E}_{ch} are the average voltage in discharge and charge process, respectively; E_{dis} and E_{ch} are the voltage at time t in discharge and charge process, respectively.

3 Screening of ionic liquids for aqueous electrolytes

Aqueous electrolytes play a critical role in safe batteries due to the non-flammability.^[134] Currently, commercial aqueous rechargeable batteries, e.g. lead–acid batteries and vanadium redox flow batteries take corrosive sulfuric acid as supporting electrolyte,^[135] whereas nickel–cadmium batteries utilize a basic solution, moreover, the utilization of toxic heavy metal compounds as electrode materials brings environment concerns.^[136] Owing to the limitation of electrochemical stability window (ESW) of water (thermodynamically 1.23 V), the output voltages of aqueous rechargeable batteries are usually less than 1.5 V.^[60,137-139] Aqueous high-voltage batteries have been realized via suppression of the hydrogen and oxygen evolution reactions in specific cases: in lead–acid batteries, a PbSO₄ layer on the lead anode which is electronically insulating but ionically conducting suppresses hydrogen evolution, to reach an output voltage of 2 V;^[140,141] while in nickel–cadmium batteries, a passivation layer of Ni(OH)₂ increases the overpotential of oxygen evolution.^[141] Recently, Suo et al. introduced a “water-in-lithium-salt” electrolyte to build an aqueous lithium-ion battery with a voltage of 2.3 V.^[142] Yamada et al. demonstrated hydrate-melt electrolytes for aqueous batteries with voltages about 3.1 V.^[143] These breakthroughs provide new pathways to develop aqueous high-voltage rechargeable batteries.^[144]

Ionic liquids are universally studied in electrochemical applications on account of their unique non-volatility and stability.^[114,120,121,145] The wide ESWs of ionic liquids make them good alternatives as supporting electrolytes for rechargeable batteries.^[15,114] Hydrophilic ionic liquids can be adopted to prepare mild “water-in-ionic-liquid” electrolytes,^[125] as they permit higher ionic conductivity and lower viscosity comparing with pristine ionic liquids. Therefore, it is highly desirable to investigate the influence of cation and anion groups of ionic liquids on the ionic conductivities as well as ESWs in “water-in-ionic-liquid” solutions. Furthermore, it can exploit applications of ionic liquids combining with suitable redox active species to develop aqueous high-voltage lithium-ion batteries^[114] and redox flow

batteries.^[125,146]

In this chapter, we investigate the ESWs and ionic conductivities of “water-in-ionic-liquid” solutions with six representative ionic liquids at different molalities, and propose an aqueous TiO₂-FeCl₂ hybrid battery with high voltage and high areal capacity. As is known, TiO₂ polymorphs have been widely studied as anode materials for lithium insertion/extraction due to their natural abundance, low cost and structural stability;^[147] while iron-based redox active species draw great attention since they are usually cheap, non-toxic and electrochemically reversible to serve as cathode materials.^[60,128] Taking advantage of “water-in-ionic-liquid” supporting electrolytes, we demonstrate reversible lithium insertion/extraction in anatase TiO₂ with LiCl as lithium source, as well as enhanced redox kinetics of iron active species.

3.1 Experimental

3.1.1 Preparation and characterization of “water-in-ionic-liquid” solutions

Six ionic liquids (EMImCl, BMImCl, TEACl, TBACl, TriMImMeSO₄ and EMMImEtSO₄, abbreviations in the Chemical list of Appendix) were dissolved in deionized water at different molalities as “water-in-ionic-liquid” solutions, i.e. molality of 5 mol kg⁻¹ means 5 mmol of ionic liquid dissolved in 1 g of water (mol kg⁻¹ is abbreviated as “m” hereafter). The ionic conductivities of “water-in-ionic-liquid” solutions were measured by a WTW Cond 3110 conductivity meter equipped with a TetraCon® 325 cell (Xylem, Germany), after calibration with a reference solution (0.01 mol L⁻¹ KCl) provided by the supplier. The rheological properties of the electrolytes were tested by a MCR 301 rheometer (Anton Paar GmbH, Graz, Austria). The ESWs were investigated by cyclic voltammetry (CV) with a Biologic VMP3 potentiostat in a three-electrode setup. A glassy carbon (GC) rod, a Pt foil and an Ag/AgCl electrode were used as working electrode (WE), counter electrode (CE) and reference electrode (RE), respectively.

3.1.2 Preparation and characterization of anodic titanium dioxide

Anodic titanium dioxide (ATO) was prepared in ethylene glycol containing 0.3 wt% NH_4F and 2 v% H_2O under DC 60 V for 6 h at room temperature. A titanium foil and a graphite electrode were used as working electrode and counter electrode, respectively.^[148] Afterwards, the titanium foil was rinsed, dried and then calcined at 450 °C for 2 h in air. The resulted titanium foil was anodized again under 60 V for 10 min, and immersed in H_2O_2 (30 wt%) for 4 h to peel off the ATO film. X-ray diffraction (XRD) measurement was conducted with X'Pert Pro diffractometer (PANalytical) using $\text{Cu } K\alpha_{1,2}$ radiation. The morphology of ATO film was characterized by scanning electron microscopy (SEM, FEI Quanta FEG 250). CV were tested in a three-electrode cell, ATO film, Pt foil and Ag/AgCl electrode were used as working electrode, counter electrode and reference electrode, respectively. The electrolytes were “water-in-ionic-liquid” solutions containing different amounts of LiCl additive.

3.1.3 Electrochemical test of titanium dioxide–iron (II) chloride hybrid battery

In a hybrid battery configuration, one half cell contains typically liquid active species, while the other compartment could be gas or solid active materials.^[1] The ATO film was attached to a graphite rod (diameter of 3 mm) with a copper tape as anode and immersed in 1 mL of BMImCl/ H_2O (10 m) containing 1.0 M LiCl. The catholyte is 1 mL of BMImCl/ H_2O (10 m) containing 0.1 M Fe^{2+} ions and 1.0 M HCl, with another graphite rod as cathode terminal lead. A piece of crosslinked and methylated polybenzimidazole anion exchange membrane (chloride form, about 40 μm thick)^[15] was used to separate them. This $\text{TiO}_2\text{--FeCl}_2$ hybrid battery was tested in a home-made static H-cell, and activated for two times before cycling, considering the sluggish diffusion of Li^+ ions in solid-state TiO_2 ($\sim 10^{-13} \text{ cm}^2 \text{ s}^{-1}$).^[149]

3.2 Characterization of electrochemical stability windows

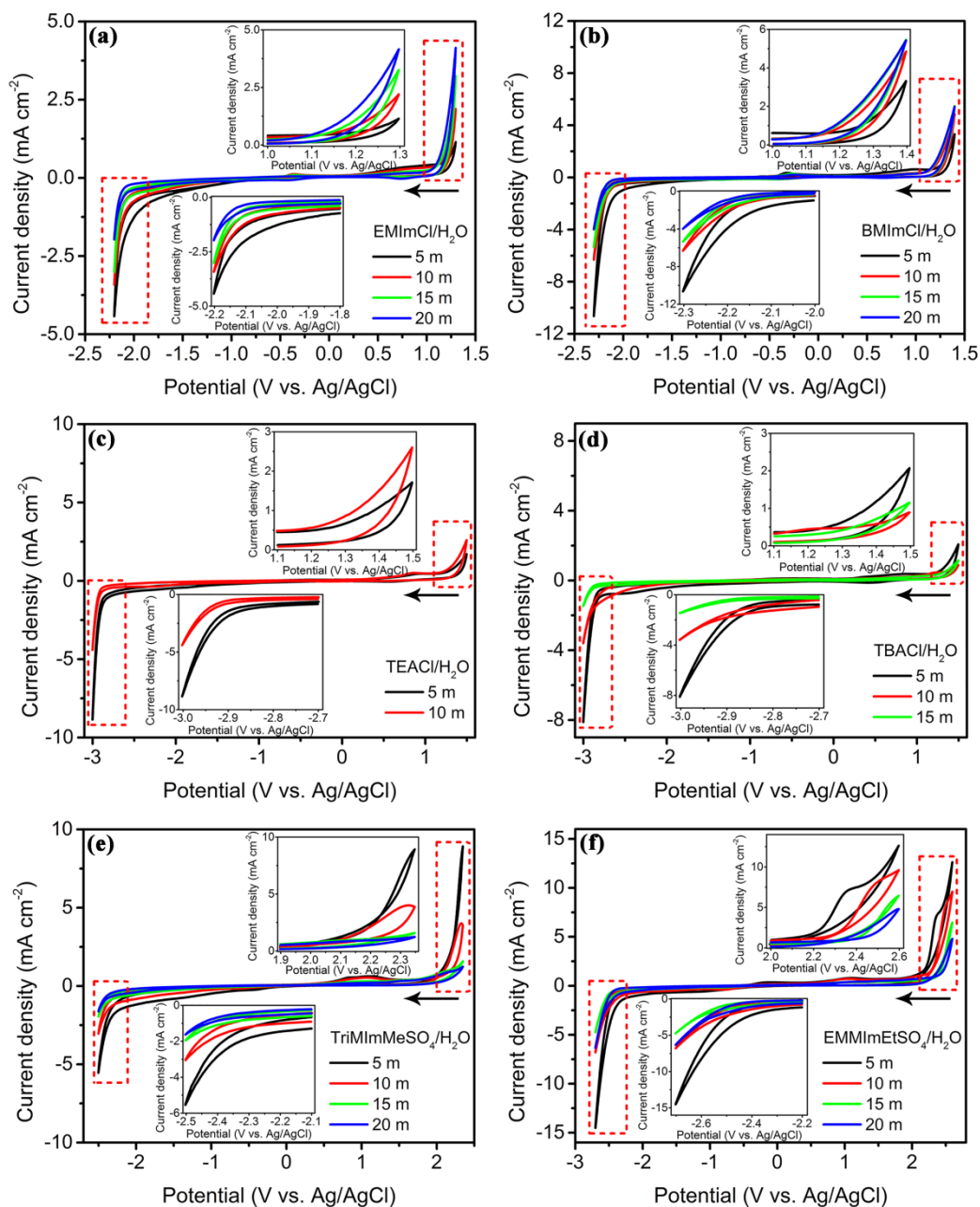


Figure 3.1 CV curves of (a) EMImCl/H₂O, (b) BMImCl/H₂O, (c) TEACl/H₂O, (d) TBACl/H₂O, (e) TriMImMeSO₄/H₂O and (f) EMMImEtSO₄/H₂O at 20 mV s⁻¹, arrows indicate scan direction.

Imidazolium chloride based ionic liquids such as EMImCl and BMImCl at different molalities from 5 m to 20 m were tested by CV measurements accordingly. As shown in Figure 3.1a and b, when the molality reaches 20 m, the onset potential in the

negative region decreases gradually to -2.0 V vs. Ag/AgCl owing to hydrogen evolution,^[150] whereas in the positive region the onset potential shifts to 1.0 V vs. Ag/AgCl, presenting an overall ESW of about 3.0 V.

Quaternary ammonium chloride based ionic liquids are universal conductive additives for electrolytes. Herein, TEACl and TBACl were chosen to study the ESWs of “water-in-ionic-liquid” solutions. A TEACl/H₂O solution at molality of 5 m shows an onset potential of hydrogen evolution at about -2.7 V vs. Ag/AgCl (Figure 3.1c), which is much more negative than that of imidazolium chloride based ionic liquids in Figure 3.1a and b, whereas the onset potential in the positive region is almost identical with that of aqueous imidazolium chloride solutions. Therefore, aqueous quaternary ammonium chloride solutions exhibit a much broader ESW than aqueous imidazolium chloride solutions, which is further confirmed in the CV curves of TEACl/H₂O and TBACl/H₂O at higher molalities (10 m and 15 m) in Figure 3.1c and d. During the cathodic scan, the onset potential shifts to -2.8 V vs. Ag/AgCl in TBACl/H₂O (15 m), revealing an overall ESW of ~ 4.0 V (Figure 3.1d). Notably, a TBACl/H₂O (15 m) solution is still flowable at room temperature, whereas TEACl/H₂O (15 m) gelatinizes after resting for two weeks.

Imidazolium based ionic liquids with large-size alkyl sulfates as anions, e.g. TriMImMeSO₄ and EMMImEtSO₄ were selected thereafter. Comparing with imidazolium chloride solutions (Figure 3.1a and b), as expected, the onset potential of TriMImMeSO₄/H₂O solution in the cathodic scan shifts to -2.3 V vs. Ag/AgCl when the molality increases to 20 m (Figure 3.1e), while the EMMImEtSO₄/H₂O solution (20 m) presents an even lower onset reduction potential of -2.4 V vs. Ag/AgCl (Figure 3.1f). In these chloride-free solutions, the onset potential in the anodic scan reaches as high as 2.0 V vs. Ag/AgCl, exhibiting an overall ESW of 4.4 V in EMMImEtSO₄/H₂O solution (20 m).

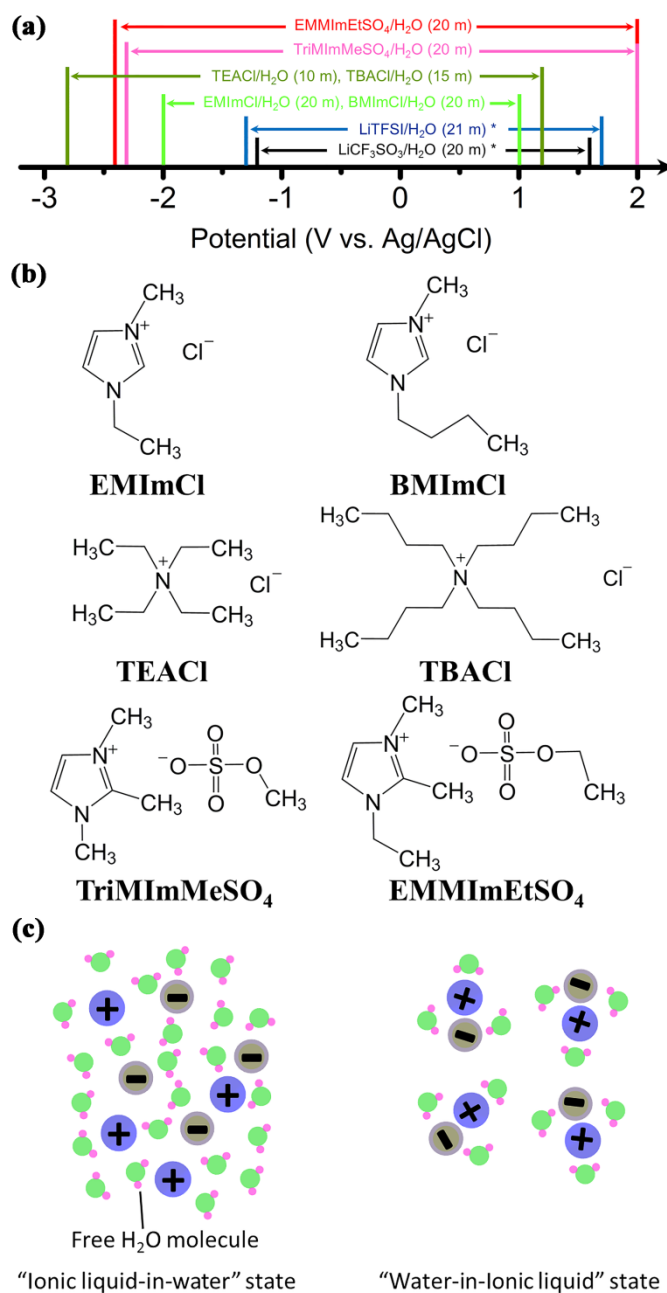


Figure 3.2 (a) Summary of ESWs of “water-in-ionic-liquid” solutions and lithium salt solutions, * data from Ref. ^[142], potential values are now referenced to the Ag/AgCl. (b) Molecular structures of the selected ionic liquids. (c) Scheme of interaction between water molecules and ionic liquids.

The ESWs of the six ILs based “water-in-ionic-liquid” solutions are summarized in Figure 3.2a. The EMImCl/H₂O and BMImCl/H₂O solutions display broad ESWs close to lithium bis(trifluoromethanesulfonyl)imide (LiTFSI) and lithium trifluoromethanesulfonate (LiCF₃SO₃, LiOTf),^[142] whereas the whole ESW shifts negatively by about 0.7 V. The different ESWs presented in “water-in-ionic-liquid” solutions can

be attributed with the molalities of solutions, the sizes of cationic and anionic groups of ionic liquids, as well as the interaction between ionic liquids and water molecules. Considering the different chemical structures of ionic liquids (Figure 3.2b), the distribution of charge density varies due to the different composition and steric orientation of cations and anions in ionic liquids, resulting in different extent of hydration of the ionic liquids.^[151]

As is known, thermodynamically, the overall water splitting (equation 3-1) is determined by the Gibbs free energy change, as given by equations below:



$$\Delta G^0 = nF\Delta E^0 \quad (3-2)$$

where ΔG^0 is the Gibbs free energy change for overall water splitting (at 298.15 K and 1 atm), n is the number of transferred electrons, F is Faraday constant (96,485 C mol⁻¹), ΔE^0 is the thermodynamic ESW of water (1.23 V).^[152] Notably, the practical ESWs of aqueous/hydrated electrolytes are associated with their concentration and composition, which are usually broader than the thermodynamic ESW of water, owing to the kinetic overpotentials for hydrogen and oxygen evolution.^[142,143]

When the molality increases from 5 m to 20 m, the molar ratio of ionic liquids to water increases from 1:11 to 1:2.7, more ionic liquids are involved in the hydration process with water molecules to form strong “ionic sheaths”^[142] (Figure 3.2c), consequently, the ratio of free water decreases sharply. In this case, more energy is needed for desolvation to break the “ionic sheaths”, and then overcome the barrier for kinetic activation to split water molecules.

$$\Delta G^* = \Delta G^0 + \Delta G_{desol} + \Delta G_a \quad (3-3)$$

$$\Delta G^* = nF\Delta E^* \quad (3-4)$$

As shown in equations 3-3 and 3-4, ΔG^* and ΔG^0 are the Gibbs free energy change for overall water splitting in practice and thermodynamics, respectively, ΔG_{desol} and ΔG_a are the Gibbs free energy change for desolvation and kinetic activation, respectively, n is the number of transferred electrons, F is Faraday constant (96,485 C mol⁻¹), ΔE^* is the practical ESW of water.

However, the kinetic process in the interface between aqueous electrolyte and electrode surface is still unclear. Computational simulation regarding interaction between the solutes (LiTFSI and LiOTf) and water molecules have been conducted to clarify the solvation process^[142,151] and water exclusion from the interface of the electrodes.^[153] They are considered to be responsible for the extension of ESW of water. However, the TFSI anions adsorb whereas OTf anions desorb accompanying positive electrode polarization to show discrepant behavior in “water-in-salt” solutions,^[153] but their super-concentrated aqueous solutions show consistent tendency in extended ESWs.^[142,154] A protective layer of solid-electrolyte interphase is suggested in aqueous fluoride solution,^[143,155] nevertheless, it is unsupportive in aqueous LiNO₃ solution.^[156] By contrast, in “water-in-ionic-liquid” solutions, simulation results indicate that water molecules accumulate within sub-nanometer from charged electrodes,^[145] thus making the general elucidation for extension of ESWs a tough conundrum. Furthermore, experimental understanding of water splitting in the interface between aqueous electrolyte and electrode surface at microscale still remains a great challenge.

3.3 Physical properties of aqueous ionic liquid electrolytes

The compositions of “water-in-ionic-liquid” solutions are given in Table 3.1. As the molarity (mol L⁻¹) increases slightly with molality (mol kg⁻¹) owing to remarkable volume expansion after dissolution of ionic liquids, the discussion of ESWs is based on variation of molality rather than molarity of “water-in-ionic-liquid” solutions.

Table 3.1 Compositions of the “water-in-ionic-liquid” solutions.

Molality (mol kg ⁻¹)	EMImCl (Mw=146.62 g mol ⁻¹)			BMImCl (Mw=174.67 g mol ⁻¹)		
	V/V ₀	C (mol L ⁻¹)	wt%	V/V ₀	C (mol L ⁻¹)	wt%
5	1.6	3.13	42.3%	1.4	3.57	46.6%
10	2.2	4.55	59.5%	2.6	3.85	63.6%
15	2.8	5.36	68.7%	3.2	4.69	72.4%
20	3.4	5.88	74.6%	4.0	5.00	77.7%

3 Screening of ionic liquids for aqueous electrolytes

Molality (mol kg ⁻¹)	TEACl (Mw=165.7 g mol ⁻¹)			TBACl (Mw=277.92 g mol ⁻¹)		
	V/V ₀	C (mol L ⁻¹)	wt%	V/V ₀	C (mol L ⁻¹)	wt%
5	1.9	2.63	45.3%	2.25	2.22	58.2%
10	2.6	3.85	62.4%	3.85	2.60	73.5%
15	3.1	4.84	71.3% (gel)	5.0	3.00	80.7%

Molality (mol kg ⁻¹)	TriMImMeSO ₄ (Mw=222.27 g mol ⁻¹)			EMMImEtSO ₄ (Mw=250.32 g mol ⁻¹)		
	V/V ₀	C (mol L ⁻¹)	wt%	V/V ₀	C (mol L ⁻¹)	wt%
5	1.8	2.78	52.6%	2.0	2.50	55.6%
10	2.7	3.70	69.0%	3.0	3.33	71.5%
15	3.5	4.29	76.9%	4.0	3.75	79.0%
20	4.4	4.55	81.6%	5.0	4.00	83.4%

Note: V/V₀ is the volume ratio of “water-in-ionic-liquid” solution to initial water, estimated with micropettes to minimize error. Solvent refers to water.

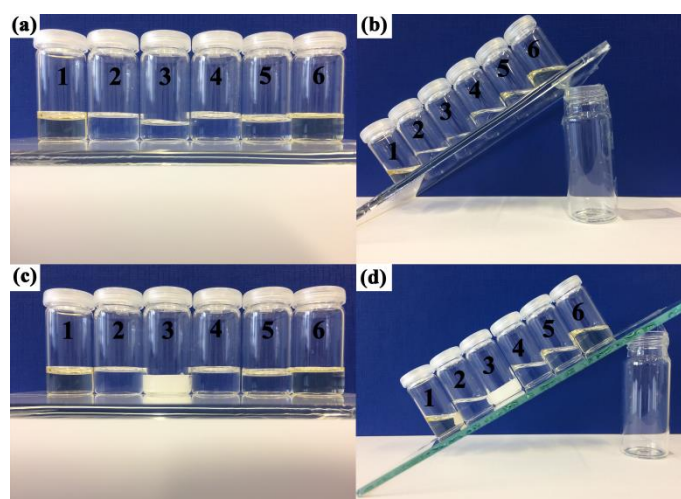


Figure 3.3 Digital photographs of the “water-in-ionic-liquid” solutions: fresh prepared solutions (a, b) and solutions rested for two weeks (c, d). **1:** EMImCl/H₂O (20 m); **2:** BMImCl/H₂O (20 m); **3:** TEACl/H₂O (15 m); **4:** TBACl/H₂O (15 m); **5:** TriMImMeSO₄/H₂O (20 m); **6:** EMMImEtSO₄/H₂O (20 m).

As shown in Figure 3.3, the solution of TEACl/H₂O (15 m) gels after rest for two weeks, whereas other “water-in-ionic-liquid” solutions remain flowable. The viscosities were measured at different temperature (Table 3.2). Among them, the solution of BMImCl/H₂O (20 m) has the highest viscosity of 56.07 mPa s at 25 °C. In higher temperature test, water evaporates obviously during temperature equilibrium process, since the amounts of ionic liquid solutions are quite low (volume of testing

cell: 2 mL), the viscosity values become abnormal at higher temperature above 35 °C.

Table 3.2 Viscosities of the “water-in-ionic-liquid” solutions.

Temperature (°C)	EMImCl 20 m	BMImCl 20 m	TEACl 15 m	TBACl 15 m	TriMImMeSO ₄ 20 m	EMMImEtSO ₄ 20 m
25	17.95	56.07	–	–	38.29	33.06
35	17.09	44.02	–	–	33.31	30.67

* Unit: mPa s, the solution of TBACl/H₂O (15 m) gels in the initial temperature equilibrium before viscosity test. Referenced viscosities of typical liquids at 25 °C (water: 0.89 mPa s; ethanol: 1.09 mPa s; ethylene glycol: 17.3 mPa s).

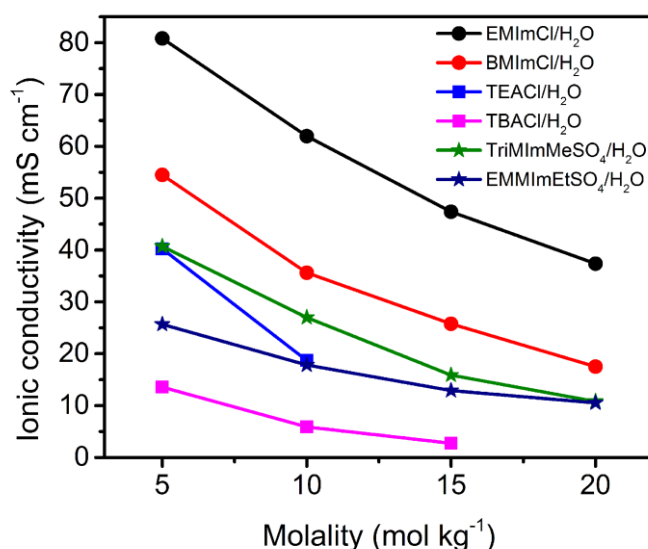


Figure 3.4 Ionic conductivities of the “water-in-ionic-liquid” solutions at different molalities (solvent refers to water).

The EMImCl/H₂O solutions show the highest ionic conductivities among all tested molalities (Figure 3.4). The ionic conductivity of EMImCl/H₂O (5 m) reaches as high as 80.8 mS cm⁻¹ but decreases to 37.4 mS cm⁻¹ at 20 m owing to the interaction of cations and anions in the solutions.^[157] The values are much higher than those of commercial non-aqueous electrolytes (7~12 mS cm⁻¹) for lithium-ion batteries^[158] and the earlier reported “water-in-lithium-salt” electrolyte (~10 mS cm⁻¹ at 21 m).^[142] However, the ionic conductivities of BMImCl/H₂O solutions (54.5 mS cm⁻¹ at 5 m and 17.5 mS cm⁻¹ at 20 m) are much lower than those of EMImCl/H₂O at the same

molalities. By contrast, the quaternary ammonium chloride aqueous solutions exhibit much lower ionic conductivities than imidazolium chloride solutions. TEACl/H₂O (5 m) presents an ionic conductivity of 40.3 mS cm⁻¹, while TBACl/H₂O (5 m) reaches only 13.6 mS cm⁻¹ and further decreases to 2.7 mS cm⁻¹ at the molality of 15 m. The ionic conductivity of TriMImMeSO₄/H₂O reaches 40.7 mS cm⁻¹ at 5 m and decreases to 10.8 mS cm⁻¹ at 20 m, which is close to the commercial non-aqueous electrolytes for lithium-ion batteries.^[158] The decreased ionic conductivity of “water-in-ionic-liquid” solutions at high concentrations could be associated with the reduced concentration of free counterions, since the interaction between cations and the surrounding anions enhances, thus restricts the mobility of cations and anions in the solutions.^[159]

3.4 Prototype of a titanium dioxide–iron (II) chloride hybrid battery

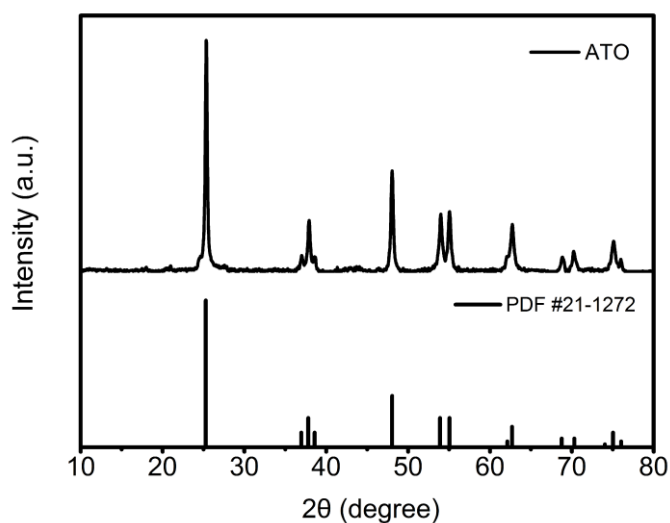


Figure 3.5 XRD pattern of anodic titanium dioxide (ATO).

The “water-in-ionic-liquid” solutions reveal wide ESWs and high ionic conductivity, making them quite suitable as supporting electrolytes for aqueous rechargeable batteries. Based on the high ionic conductivity and purity, BMImCl/H₂O solution was chosen as an example to demonstrate the feasibility to be an effective supporting electrolyte for an aqueous high-voltage battery. TiO₂ is an ideal anode

material as a host for metal ions to develop aqueous high-voltage batteries, owing to the stable structure and low redox potential.^[139,160-162] An ATO film was prepared according to previous reports.^[148,162] The crystal structure of ATO sample can be ascribed to anatase TiO_2 , which is in good accordance with the standard X-ray diffraction pattern (PDF No.21–1272, Figure 3.5). The as-obtained ATO film is about 70 μm thick, comprised of uniform TiO_2 nanotubes (average diameter: 130 nm) with one-side-open structure (Figure 3.6). Lithium insertion/extraction of the ATO at low negative potential is tested in BMImCl/ H_2O supporting electrolyte thereafter.

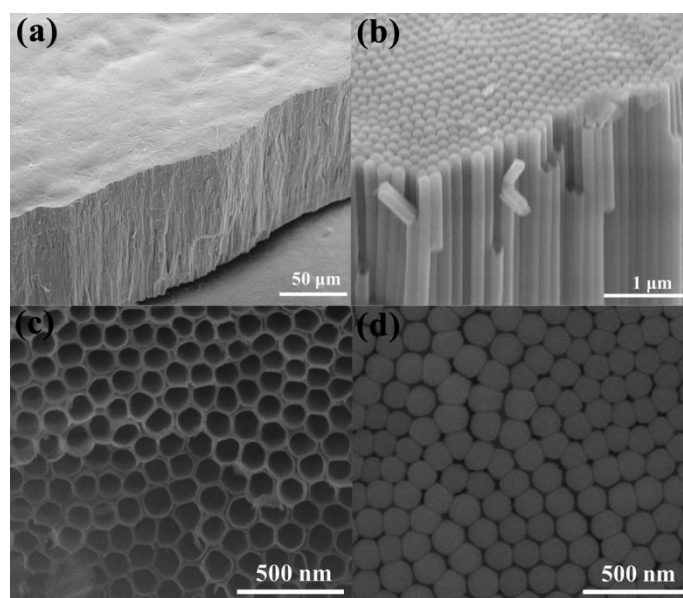


Figure 3.6 SEM images of ATO, (a) cross-section of ATO film, (b) enlarged cross-section of ATO film, (c) front-view of ATO film, (d) back-view of ATO film.

The concentrated LiCl solutions exhibit much narrower ESWs in Figure 3.7a, comparing with the “water-in-ionic-liquid” solutions. During the investigation of redox behavior of ATO film, no redox peaks can be observed in the concentrated LiCl solutions (Figure 3.7b). In the absence of LiCl in BMImCl/ H_2O , weak peaks appear at around -1.7 V, which may be associated with the interaction between TiO_2 and BMImCl (Figure 3.7c).

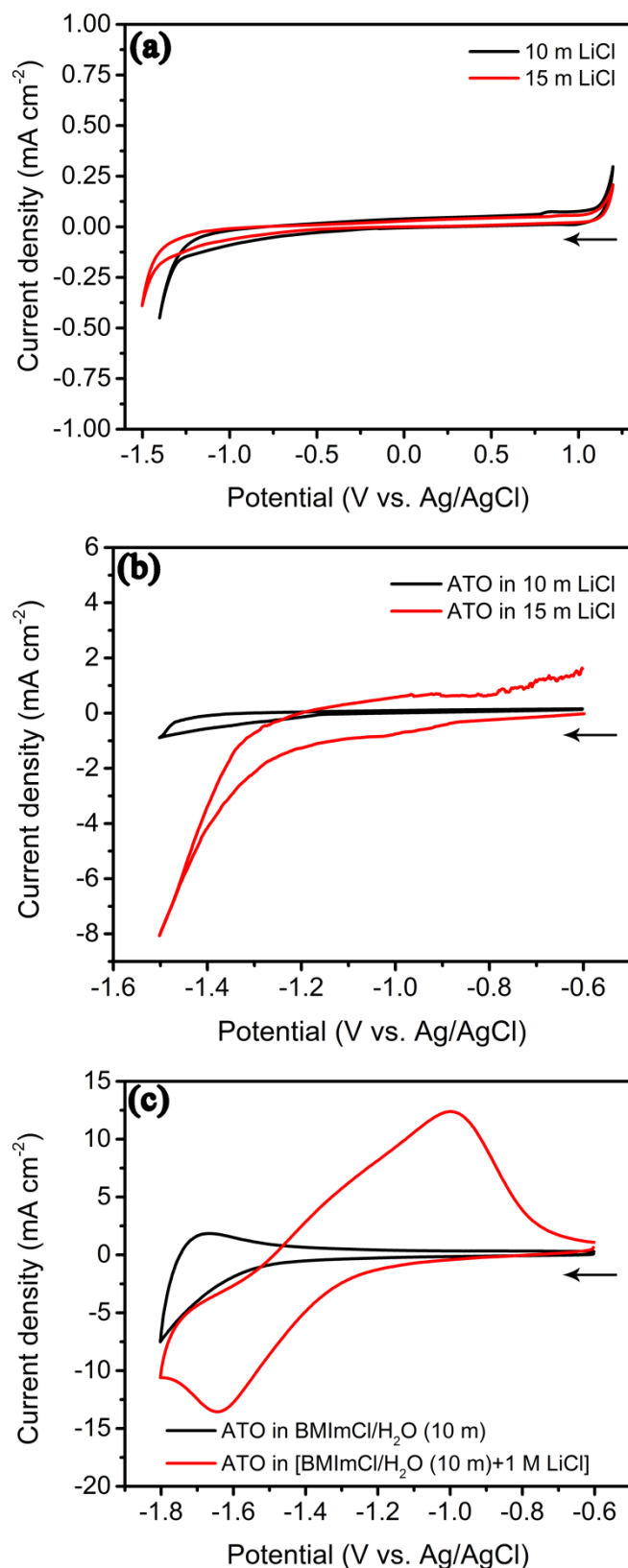


Figure 3.7 (a) Electrochemical stability windows of aqueous LiCl solutions at 20 mV s⁻¹. CV curves of ATO in (b) aqueous LiCl solutions, (c) BMImCl/H₂O (10 m) with or without LiCl at 10 mV s⁻¹, arrows indicate scan direction.

After LiCl was added into BMImCl/H₂O as lithium source, obvious redox peaks between -1.8 and -0.6 V vs. Ag/AgCl can be found (Figures 3.7c and 3.8), indicating that “water-in-ionic-liquid” solutions are feasible alternatives as supporting electrolytes to provide stable ESWs for insertion/extraction of Li⁺ ions in TiO₂ at low negative redox potentials. The redox peak separation increases along with the scan rates and concentration of LiCl in the BMImCl/H₂O (10 m) solution as shown in Figure 3.8a and b. Similar (de)lithiation behavior of ATO can also be found when EMImCl/H₂O (10 m) and EMMImEtSO₄/H₂O (10 m) were utilized as supporting electrolytes (in Figures 3.9 and 3.10, respectively).

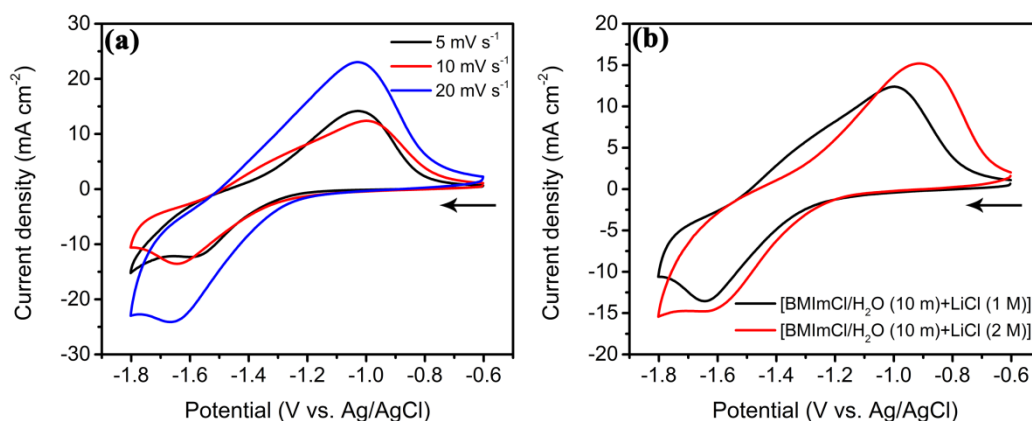


Figure 3.8 CV curves of ATO in (a) BMImCl/H₂O (10 m) with 1.0 M of LiCl at different scan rates and (b) BMImCl/H₂O (10 m) containing different amounts of LiCl at 10 mV s⁻¹, arrows indicate scan direction.

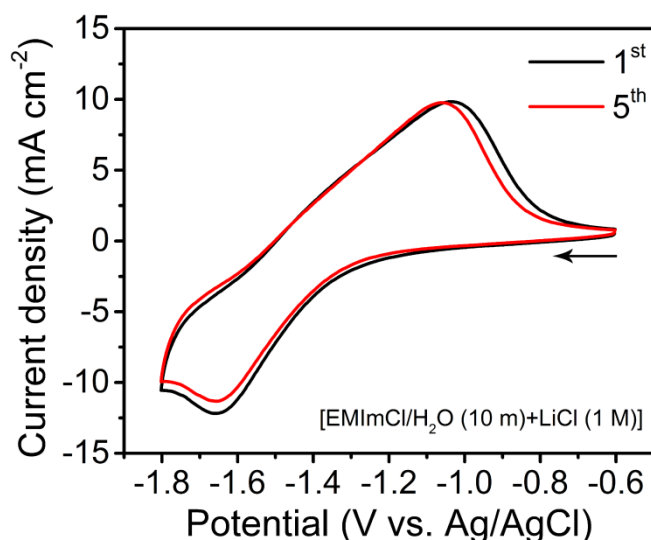


Figure 3.9 CV curves of ATO in EMImCl/H₂O (10 m) containing 1.0 M of LiCl at 10 mV s⁻¹, arrow indicates scan direction.

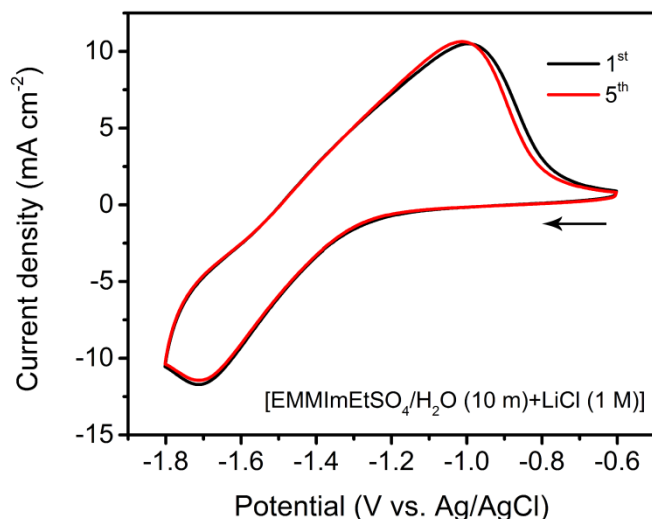


Figure 3.10 CV curves of of ATO in EMMImEtSO₄/H₂O (10 m) containing 1.0 M of LiCl at 10 mV s⁻¹, arrow indicates scan direction.

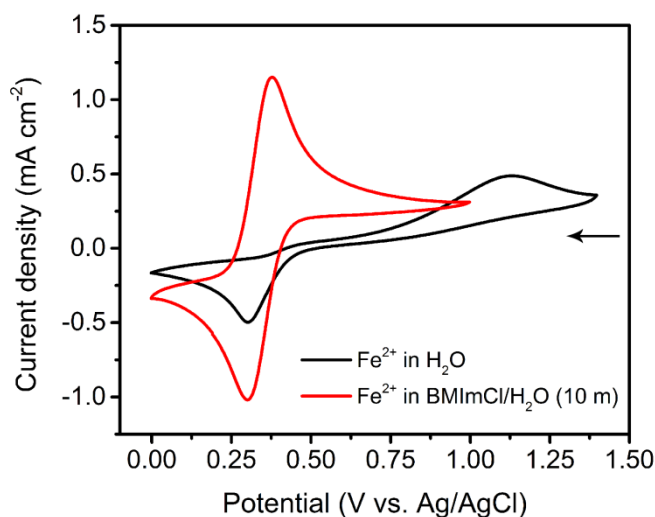


Figure 3.11 CV curves of iron active species in water and BMImCl/H₂O (10 m) at 10 mV s⁻¹, arrow indicates scan direction.

The redox activity of iron ions can be obviously improved in BMImCl/H₂O solution.^[128] As shown in Figure 3.11, reversible redox peaks appear at about +0.4 V vs. Ag/AgCl with a small potential separation around 75 mV, which is much lower than that of 800 mV in deionized water. Therefore, the iron active species is used as active species in the catholyte. Consequently, an aqueous TiO₂-FeCl₂ hybrid battery is designed with a home-made H-cell (Figure 3.12), according to the following redox reactions based on the dominant active species, as iron complexes of FeCl₄²⁻, FeCl₄⁻,

Fe_3Cl_7^- and Fe_2Cl_7^- may form in BMImCl/ H_2O solutions, but the accurate molar ratio and stability under charge/discharge is unable to determine yet^[128,163]:

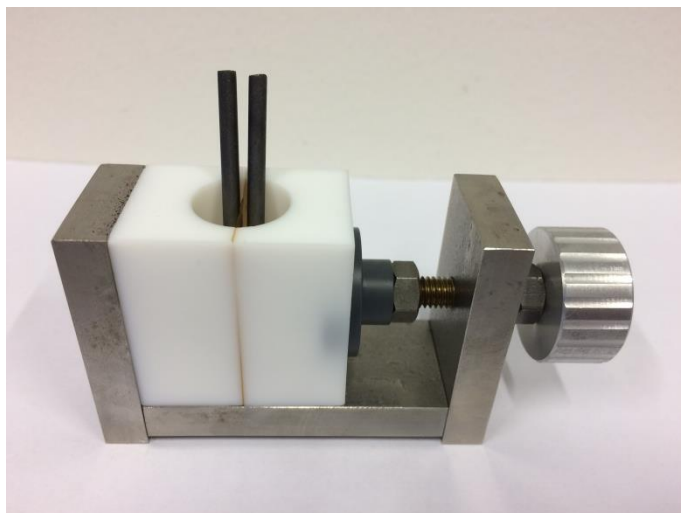
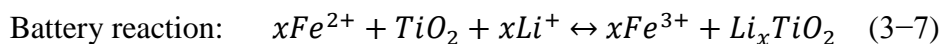
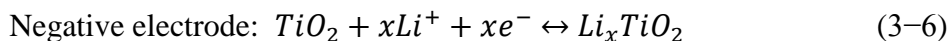
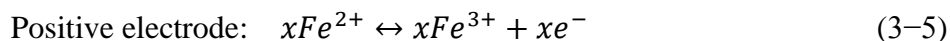


Figure 3.12 A digital photograph of home-made H-cell.

A prototype TiO_2 - FeCl_2 hybrid battery is illustrated in Figure 3.13a, using an anion exchange membrane with chloride counterions as the separator.^[15] As shown in Figure 3.13b, the cathodic and anodic peaks appear at -1.65 V and -1.0 V, which can be ascribed to the insertion and extraction of Li^+ ions in the lattice of anatase TiO_2 , respectively. Accordingly, the iron active species show redox peaks at 0.4 V with good redox reversibility in Figure 3.13c. The CV curves in Figure 3.13b and c almost overlap after 5 cycles, confirming the stability of the redox reactions on the anode side and cathode side, respectively.

The aqueous hybrid battery exhibits a clear discharge voltage plateau at about 1.7 V at a current density of 10 mA cm^{-2} in a static H-cell (Figure 3.13d). The average Coulombic efficiency is around 75%, which is much higher than that in mixed aqueous alkaline electrolyte (below 60%).^[139] Suo et al. argued that rechargeable batteries with TiO_2 anode in the aqueous LiTFSI electrolyte take about 60 cycles to form a stable solid electrolyte interphase, along with accumulative lithium

consumption and a progressive increase of Coulombic efficiency from 58% to 97%.^[160] The discharge capacity of the prototype hybrid battery keeps stable at about 0.2 mAh cm^{-2} during the first 15 cycles, which is obviously higher than related reports with TiO_2 anode.^[160,164,165] A comparison of areal capacity is given in Table 3.3, including full cells with aqueous electrolytes and half cells with non-aqueous electrolytes. Afterwards, a slight and progressive decrease in discharge curve is observed. Considering the small contact area (0.75 cm^2) of graphite rod and the catholyte, as well as sluggish diffusion of charge carriers in the solid ATO anode, catholyte and membrane in the static H-cell, further optimization is needed.

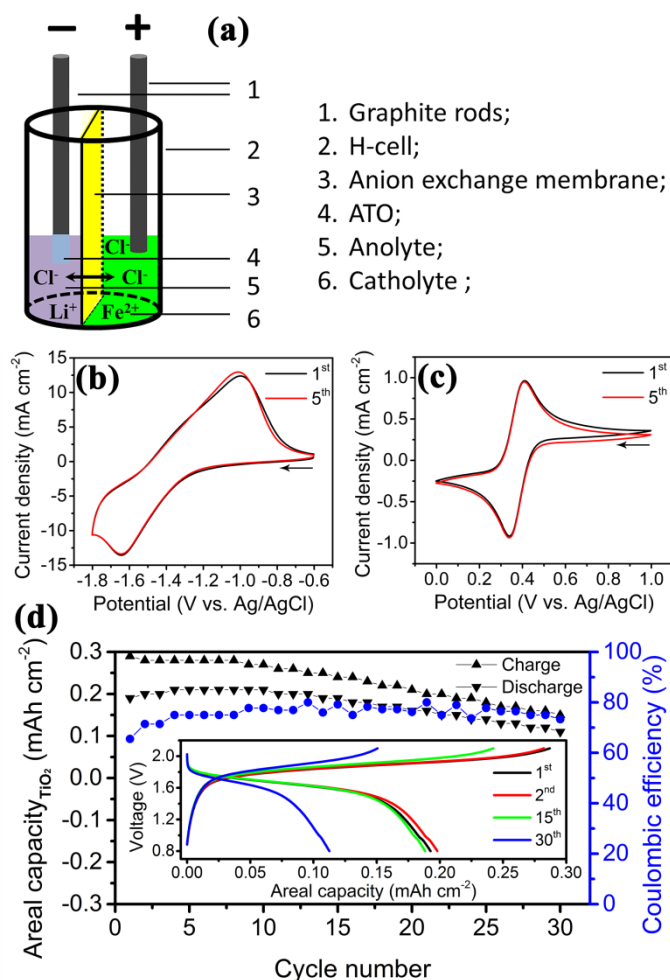


Figure 3.13 (a) Illustration of an aqueous TiO_2 - FeCl_2 hybrid battery. CV curves of (b) ATO in $\text{BMImCl}/\text{H}_2\text{O}$ (10 m) containing 1.0 M of LiCl , and (c) $\text{BMImCl}/\text{H}_2\text{O}$ (10 m) containing 0.1 M of FeCl_2 and 1.0 M of HCl at scan rates of 10 mV s^{-1} , arrows indicate scan direction. (d) Cycle performance of aqueous hybrid battery at 10 mA cm^{-2} , inset shows the charge/discharge curves.

Table 3.3 Capacity comparison of TiO₂ based rechargeable batteries.

Cathode// Anode	Electrolyte	Average discharge voltage (V)	Capacity (mAh cm ⁻²)	Coulombic efficiency	Ref.
FeCl ₂ solution// TiO ₂ nanotube arrays	1.0 M LiCl in BMImCl/H ₂ O (10 m)	1.7	0.2	~75%	This work
LiMn ₂ O ₄ // carbon coated TiO ₂	(21 m LiTFSI+7 m LiOTf) aqueous electrolyte	2.1	~0.054 ^[b]	58%~97%	Angew. Chem. 2016, 55, 7136– 7141
TiO ₂ microcones// Li metal (half cell)	1.0 M LiPF ₆ in PC: EC : DEC = 1:4:5 (v/v/v) ^[a]	1.8	0.16	90.30%	ACS Appl. Mater. Interfaces 2016, 8, 14558– 14563
Ni/TiO ₂ nanowires // Li metal (half cell)	1.0 M LiPF ₆ in EC/DMC (1:1 v/v) ^[a]	1.8	0.16	>97%	Nano Lett. 2012, 12, 655–660
α-Ni(OH) ₂ // TiO ₂ nanotube arrays	mixed LiOH (1.5 M)+KOH (4 M) aqueous electrolyte	1.7	~0.36 ^[b]	~60%	Energy Environ. Sci., 2010, 3, 1732–1735

*[a]: non-aqueous electrolytes; [b] estimated from the given information in the literature.

3.5 Conclusions

In conclusion, the ESWs and ionic conductivities of “water-in-ionic-liquid” solutions have been investigated based on their molalities in water. These aqueous ionic liquid solutions exhibit wide ESWs from 3 to 4.4 V due to interaction between different cationic/anionic groups of ionic liquids and water, as well as high ionic conductivities, which are considered to be satisfactory supporting electrolytes to build aqueous high-voltage rechargeable batteries. Electrochemical behavior of (de)lithiation reaction in TiO₂ and enhanced redox activity of iron active species have been observed in these aqueous supporting electrolytes. An aqueous TiO₂-FeCl₂ hybrid battery with a voltage of 1.7 V has been successfully realized to exhibit an areal capacity of 0.2 mAh cm⁻².

4 Ionic liquid based aqueous electrolytes for a zinc–iron hybrid flow battery

Iron based compounds have been widely studied as redox active species for catholyte and anolyte due to the high abundance and tunable redox potentials.^[60,62,83] Recently, zinc based hybrid flow batteries have revived the zinc halogen flow batteries, e.g. zinc–bromine flow battery^[21] and zinc–iodine flow battery,^[30,31,33] utilizing the cheap and non-toxic zinc compounds. The zinc–iron flow battery is considered to be promising based on the redox potentials of cheap iron and zinc species.^[47,63,166] A weak acidic solution of HAc/NaAc has been adopted to improve zinc plating/stripping.^[167] Inspired by a lower redox potential of zinc plating/stripping in basic solutions, a double-membrane and triple-electrolyte design has been realized in a zinc–iron flow battery with a discharge voltage of 1.8 V, in spite of the complicated cell structure.^[47] Li et al. reported a zinc–iron flow battery with neutral electrolytes to present high efficiencies, using a soluble iron complex and a microporous separator.^[63] It is noteworthy that the rate constant is dominant in redox reactions to improve the performance of RFBs. Surface modification of carbon felts has been reported to promote the kinetics of redox reaction of $\text{VO}_2^+/\text{VO}^{2+}$ in VRFBs,^[22] while the rate constants of bromide and sulfide in the electrolytes of polysulfide–bromide redox flow battery (PSBRFB) can be improved to 4×10^{-5} and $3 \times 10^{-6} \text{ cm s}^{-1}$ with activated carbon electrodes, respectively.^[168] In contrast, the poor redox activity and sluggish reaction rate of $\text{Cr}^{3+}/\text{Cr}^{2+}$ ions hindered the early development of Fe–Cr flow battery, the rate constant of $\text{Cr}^{3+}/\text{Cr}^{2+}$ ions can be increased to $1.35 \times 10^{-3} \text{ cm s}^{-1}$ with bismuth trihydride (BiH_3) electrode, three orders higher than that with Bi metal ($9.0 \times 10^{-7} \text{ cm s}^{-1}$),^[169] enhanced performance has been demonstrated with Bi^{3+} ions as catalysts in the electrolyte.^[170] However, there are few electrochemical kinetic analyses on the iron and zinc redox active species.

In this chapter, aqueous ionic liquid and calcium chloride solutions are used as supporting electrolytes for iron and zinc redox active species, respectively. These

supporting electrolytes exhibit wide ESWs to cope with gas evolution during charge process. The redox behaviors of iron and zinc active species are enhanced remarkably in the corresponding supporting electrolytes. The compositions of catholyte and anolyte are tuned systematically. Electrochemical kinetic analyses shed light on the redox activity of the iron active species as well as the zinc plating/stripping process. Afterwards, a zinc–iron flow battery is built by means of an anion exchange membrane with chloride counterions.^[15] This zinc–iron flow battery presents high electrochemical performance in flow cell and static H-cell, showing high potential in application based on the cheap and non-toxic iron and zinc species.

4.1 Experimental

4.1.1 Preparation and characterization of electrolytes

Herein aqueous ionic liquid solutions were prepared in deionized water at different molalities as required. As the molarity (mol L^{-1} , M) of aqueous ionic liquid solutions increases slightly along with molality (mol kg^{-1} , abbreviated as “m” hereafter), owing to the remarkable volume expansion after dissolution of ionic liquids, e.g. the molar concentrations of 5 m, 8 m and 10 m BMImCl/H₂O are ~3.57 M, 3.64 M and 3.85 M, respectively. Iron salt was dissolved in BMImCl/H₂O or deionized water; zinc salt was dissolved in CaCl₂/H₂O or deionized water. The liquid media for FeCl₂ solutions were purged with nitrogen or argon gas for 1 h before use. The redox activities of iron and zinc salts were investigated, respectively, to regulate the composition of corresponding supporting electrolytes. Cyclic voltammetry (CV) was conducted in a three-electrode system with a Biologic potentiostat (VMP3, France). A glassy carbon rod, a piece of Pt foil and an Ag/AgCl electrode were used as working electrode, counter electrode and reference electrode, respectively. The electrochemical stability windows (ESWs) of the aqueous electrolytes were investigated accordingly. The FeCl₂ solutions were further purged for 30 min before CV tests. The CV simulation was conducted with software of EC-Lab V10.44 version. A conductivity meter (WTW Cond 3110, Xylem, Germany) equipped with a measuring cell of TetraCon® 325 was

adopted to test the ionic conductivities of electrolytes. Before the test, the conductivity meter was calibrated with a reference solution (0.01 mol L⁻¹ KCl) provided by the supplier.

4.1.2 Assembly of symmetric Zn–Zn cells and characterization of zinc dendrites

Symmetric Zn–Zn cells were assembled with zinc plates and Whatman filter paper as electrodes and separator, respectively.^[171,172] The supporting electrolytes were E1: deionized water, E2: 0.2 M NH₄Cl, E3: 0.5 M NH₄Cl, E4: 1.0 M NH₄Cl; E5: BMImCl/H₂O (8 m), E6 : [BMImCl/H₂O (8 m)+0.5 M NH₄Cl]; E7: CaCl₂/H₂O (3.5 m), E8: [CaCl₂/H₂O (3.5 m)+0.5 M NH₄Cl], with pH values ranging from 5~8. These supporting electrolytes contain 0.1 M ZnCl₂. Charge/discharge cycles were conducted at 0.2 mA cm⁻² for 10 minutes for each step. Then the symmetric Zn–Zn cells were disassembled and characterized by scanning electron microscopy (SEM, FEI Quanta FEG 250).

4.1.3 Electrochemical tests of the zinc–iron flow battery

Graphite felts (GFD 4.6 EA, specific surface area of 0.4 m² g⁻¹, SGL Carbon Group, Germany) were thermally treated at 450 °C in air for 6 h before use. Two pieces of graphite felts (2×2 cm², one graphite felt is 0.2 g, the reactive area is calculated to be 800 cm²) were held with a thickness compression ratio of ~20% in Viton gaskets and used as electrodes on cathode side and anode side separately. A piece of anion exchange membrane (chloride form) as reported previously^[15] was sandwiched between the cathode and anode. Solution A of BMImCl/H₂O (8 m, i.e. 8 mmol of BMImCl dissolved in 1 g of H₂O) was mixed with solution B of HCl (10 M) (A/B =9/1, v/v) as supporting electrolyte for iron (II) chloride to prepare catholyte. The aqueous CaCl₂ solution containing 0.5 M NH₄Cl was used as supporting electrolyte for zinc salt to prepare anolyte. CaCl₂•2H₂O was dissolved in deionized water at a molality of 4 m to balance the osmotic pressure, the molality based on CaCl₂ is 3.5 m. The catholyte and anolyte were circulated between the flow cell and reservoirs by a

peristaltic pump (Ismatec REGLO, Germany) at a flowing rate of 30 mL min^{-1} . Each reservoir was filled with 10 mL of electrolytes. Static test was conducted in an H-cell as introduced in chapter 3, 1 mL of catholyte and anolyte was used, respectively, the reactive surface area of graphite rod terminal (diameter: 3 mm) is 0.75 cm^2 . Electrochemical impedance spectroscopy (EIS) and galvanostatic charge/discharge tests were conducted with a Biologic VMP3 potentiostat.

4.2 Design of the zinc–iron hybrid flow battery

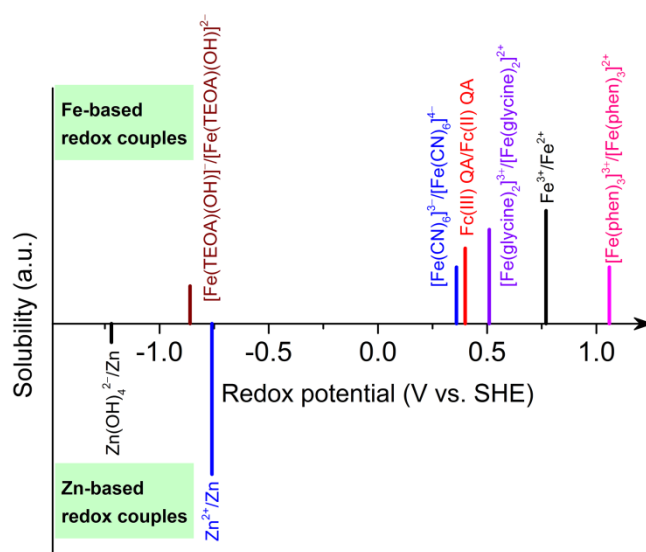


Figure 4.1 Redox potentials of Fe-based and Zn-based redox active species. Abbreviations: triethanolamine (TEOA); ferrocene (Fc); quaternary ammonium salts (QA); 1,10-phenanthroline (phen).

The redox potentials of Fe-based and Zn-based redox active species can be tuned in different supporting electrolytes.^[47,62,63] As shown in Figure 4.1, zinc plating/stripping behavior in strong basic solutions exhibits much lower redox potential than that in neutral or weak acidic electrolytes, to build high-voltage hybrid flow batteries.^[47] By contrast, the redox potentials of Fe-based active species can be varied with different ligands or supporting electrolytes. Ferrocyanides and ferrocene based quaternary ammonium salts have been widely studied in aqueous RFBs;^[60,77] triethanolamine, 1,10-phenanthroline and glycine have been introduced as effective ligands to regulate the redox behavior of Fe³⁺/Fe²⁺ active species.^[62,173] As previously reported, the redox

activity of $\text{Fe}^{3+}/\text{Fe}^{2+}$ active species can be obviously enhanced in aqueous ionic liquid solution of BMImCl/ H_2O .^[128] Considering the redox potentials of Fe-based and Zn-based redox active species, a feasible zinc–iron hybrid flow battery is designed with Zn^{2+}/Zn and $\text{Fe}^{3+}/\text{Fe}^{2+}$ active species.

4.3 Optimization of catholyte and anolyte

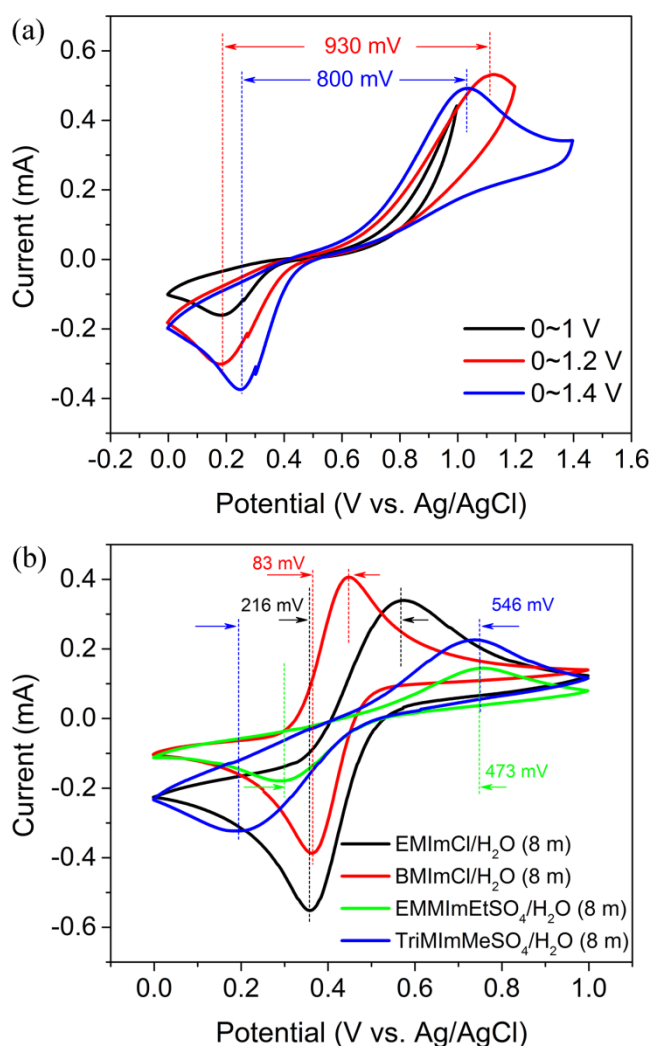


Figure 4.2 CV curves of 50 mM FeCl_2 in (a) H_2O ; (b) various aqueous ionic liquid solutions.

The redox behavior of iron active species was studied in a three-electrode setup by CV measurements. In deionized water, the redox activity of iron active species is quite poor and irreversible with peak separations up to 930 mV in different potential

regions (Figure 4.2a). The peak separations indicate large polarization which is detrimental for rate performance of RFBs. A polysulfide–iodide flow battery presented high peak separations in the CV curves as well as low efficiencies and high potential gaps in the charge/discharge rate test.^[35] In contrast, the redox behavior of iron active species can be remarkably improved in BMImCl/H₂O solutions, comparing with other ionic liquid solutions as shown in Figure 4.2b. Additionally, the sulfate-based ionic liquid solutions presented lower ionic conductivities^[174], therefore, BMImCl/H₂O is used as supporting electrolyte for iron species.^[128] As the molality of BMImCl/H₂O increases from 5 m to 10 m, the redox potentials of the iron species decrease obviously, with peak separations vary from 271 mV to 71 mV (Figure 4.3). Based on the CV results, an optimized molality of 8 m BMImCl/H₂O is adopted as the supporting electrolyte for the iron active species. To prevent the hydrolysis and precipitation of iron salts, hydrochloric acid was added into the catholyte. The ESWs of BMImCl/H₂O (8 m) containing different amount of HCl were characterized accordingly. When the concentration of HCl increases, the ESWs narrow gradually (Figure 4.4). However, even the concentration of HCl increases to 1.0 M, the ESWs are still affordable for the redox-active potential region of the iron active species.

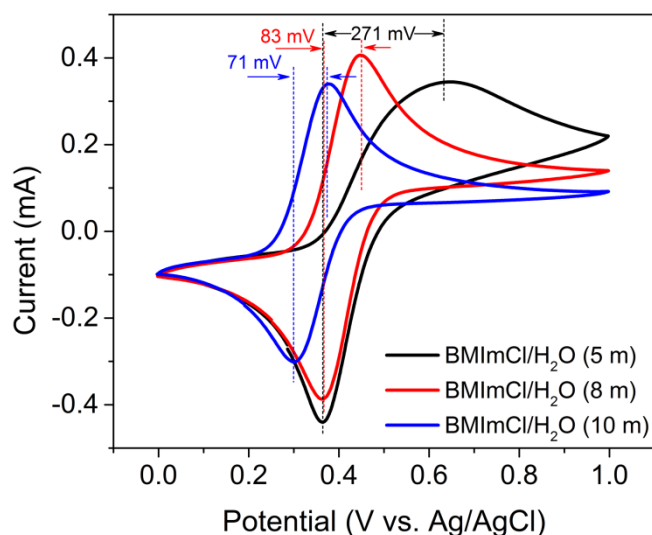


Figure 4.3 Different molalities of BMImCl/H₂O without HCl addition.

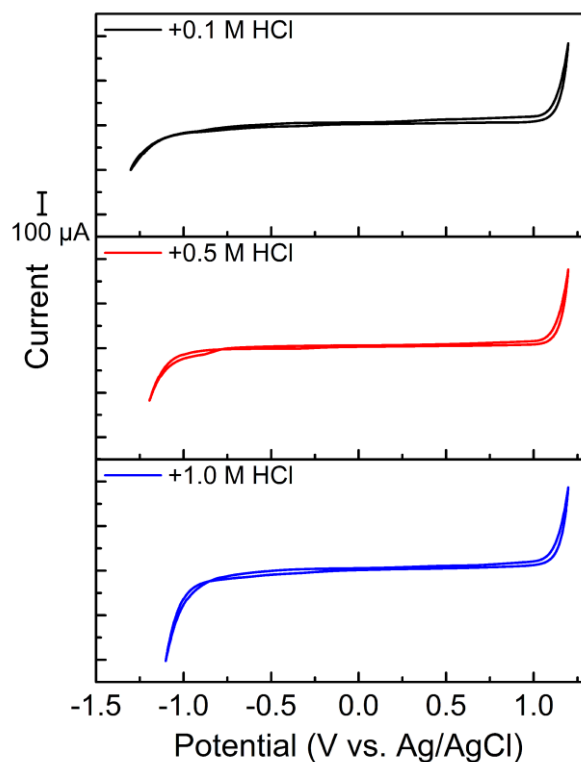


Figure 4.4 Electrochemical stability windows (ESWs) of BMImCl/H₂O (8 m) with different amount of HCl addition.

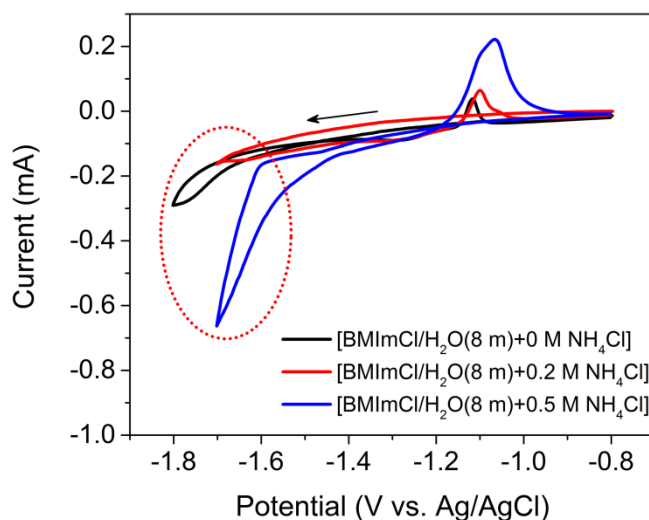


Figure 4.5 CV curves of (a) ZnCl₂ (50 mM) in BMImCl/H₂O (8 m) with different amount of NH₄Cl.

Super-concentrated aqueous electrolytes have been developed for zinc-metal rechargeable batteries to prevent the growth of zinc dendrites. Nevertheless, these viscous gel-like electrolytes with low ionic conductivities are not suitable for flow batteries.^[171] Alternatively, we took medium-concentrated supporting electrolytes for

zinc species, not only to balance the osmotic pressure from catholyte, but also improve zinc plating/stripping. Zinc plating/stripping in BMImCl/H₂O (8 m) containing different amounts of NH₄Cl shows poor redox reversibility with low peak currents and high overpotential of ~400 mV during plating process (Figure 4.5). Obvious nucleation loops can be found at negative potentials as indicated by a red circle. Even though the redox activities of zinc plating/stripping can be improved with higher peak currents when NH₄Cl is added, zinc nucleation hysteresis is inevitable, indicating that the nucleation barrier of ZnCl₂ in BMImCl/H₂O (8 m) is too high. The effect of NH₄Cl in zinc plating/stripping will be discussed in the kinetic analysis. Therefore, the BMImCl/H₂O solutions are not appropriate supporting electrolytes for zinc plating/stripping. Glycine betaine was used as supporting additive due to the high water-solubility, non-toxicity and low cost. Although the solutions show wide ESWs (Figure 4.6a) and improved zinc plating/stripping behavior (Figure 4.6b), the ionic conductivity is quite low ($< 1 \text{ mS cm}^{-1}$).

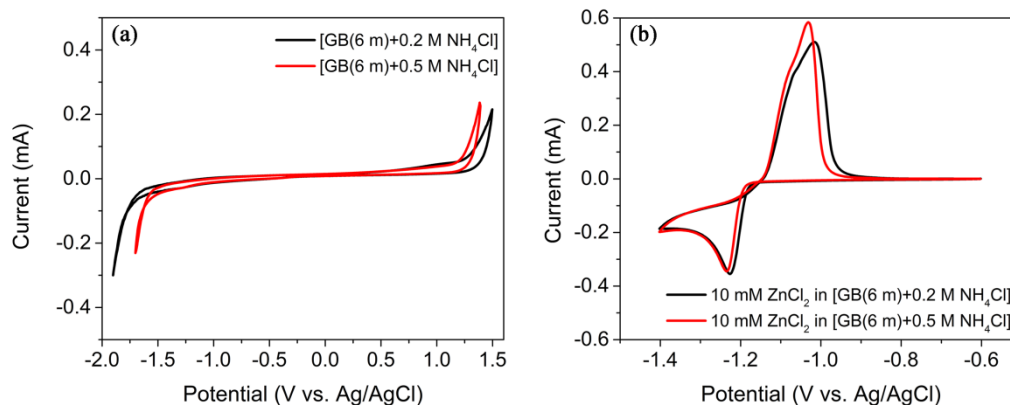


Figure 4.6 CV curves of (a) aqueous GB solution (6 m to balance the osmotic pressure from the catholyte) with NH₄Cl and (b) ZnCl₂.

Since BMImCl/H₂O solutions were not suitable as supporting electrolytes for zinc plating/stripping, alternative supporting electrolytes for anolyte were needed to balance the osmotic pressure from catholyte first. To meet the requirements (high ionic conductivity and wide ESW) as supporting electrolytes for zinc species, aqueous chloride solutions became a primary choice owing to the low cost, high solubility to

balance the osmotic pressure, and chemical stability in the anolyte.

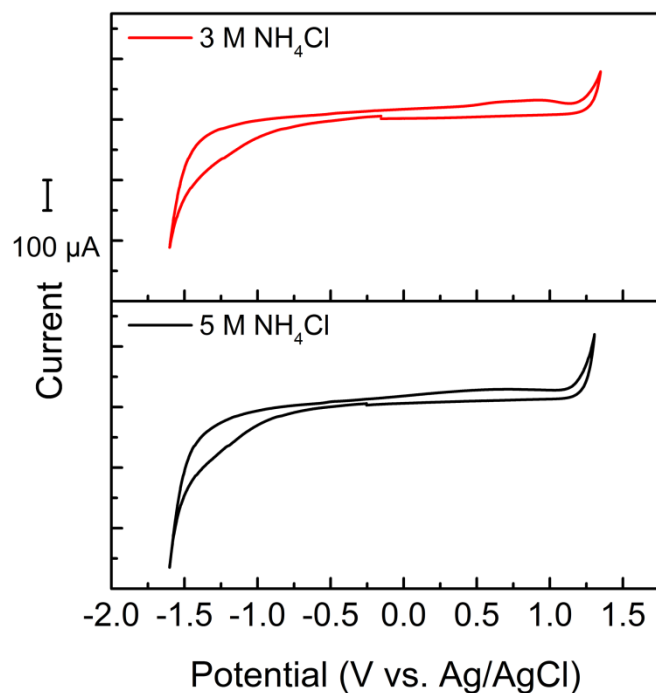


Figure 4.7 Electrochemical stability windows (ESWs) of NH_4Cl solutions.

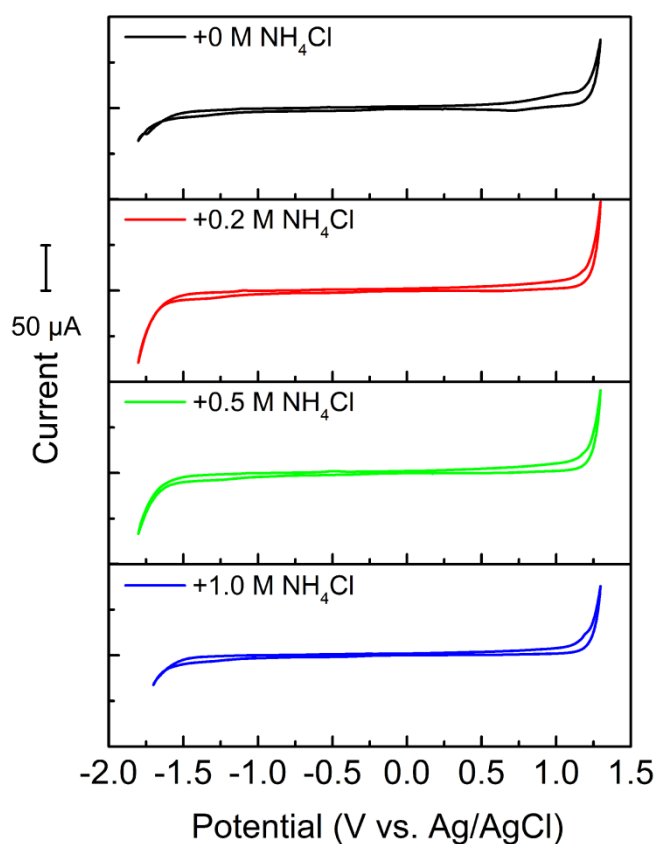


Figure 4.8 Electrochemical stability windows (ESWs) of $\text{CaCl}_2/\text{H}_2\text{O}$ (3.5 m) with different amount of NH_4Cl addition.

Concentrated aqueous NH_4Cl solutions were selected initially to balance the osmotic pressure from catholyte. The ESWs are shown in Figure 4.7, however, the narrow ESWs cannot afford stable potential region for zinc plating/stripping. Aqueous CaCl_2 solution has been taken into consideration thereafter. As expected, the aqueous CaCl_2 solutions reveal wide ESWs in Figure 4.8. Even after addition of different amount of NH_4Cl , the ESWs are still appropriate for zinc plating/stripping. Based on the high solubility, natural abundance and wide ESW, aqueous CaCl_2 solution (3.5 m) is utilized as supporting electrolyte for zinc species accordingly.

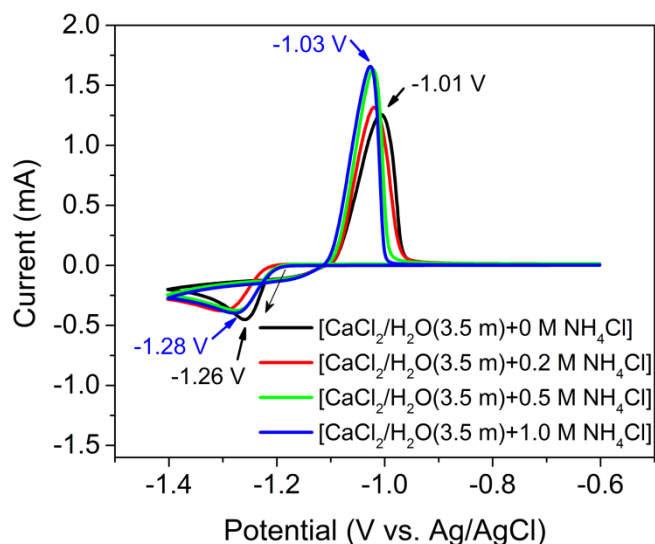


Figure 4.9 CV curves of ZnCl_2 (10 mM) in $\text{CaCl}_2/\text{H}_2\text{O}$ (3.5 m) with different amount of NH_4Cl addition.

The redox behavior of zinc plating/stripping in aqueous CaCl_2 solutions was characterized by CV measurements in a three-electrode setup as before. As shown in Figure 4.9, the overpotentials for nucleation are much smaller than those in $\text{BMImCl}/\text{H}_2\text{O}$ (8 m). Accordingly, the CV curves reveal similar nucleation loops with those in aqueous NH_4Cl solutions as indicated by the arrow inside. The nucleation hysteresis cannot be observed in the CV curves. The redox peak currents increase along with the addition amount of NH_4Cl . It should be noted that in the supporting electrolytes of aqueous CaCl_2 solutions containing 0.5 M and 1.0 M NH_4Cl , the CV curves almost overlap. After calculation and analysis on the total concentration of

dissociative ions in the catholyte, an aqueous CaCl_2 solution containing 0.5 M NH_4Cl is more suitable to balance the osmotic pressure. Therefore, an optimized supporting electrolyte of $\text{CaCl}_2/\text{H}_2\text{O}$ (3.5 m) with 0.5 M NH_4Cl is adopted for anolyte.

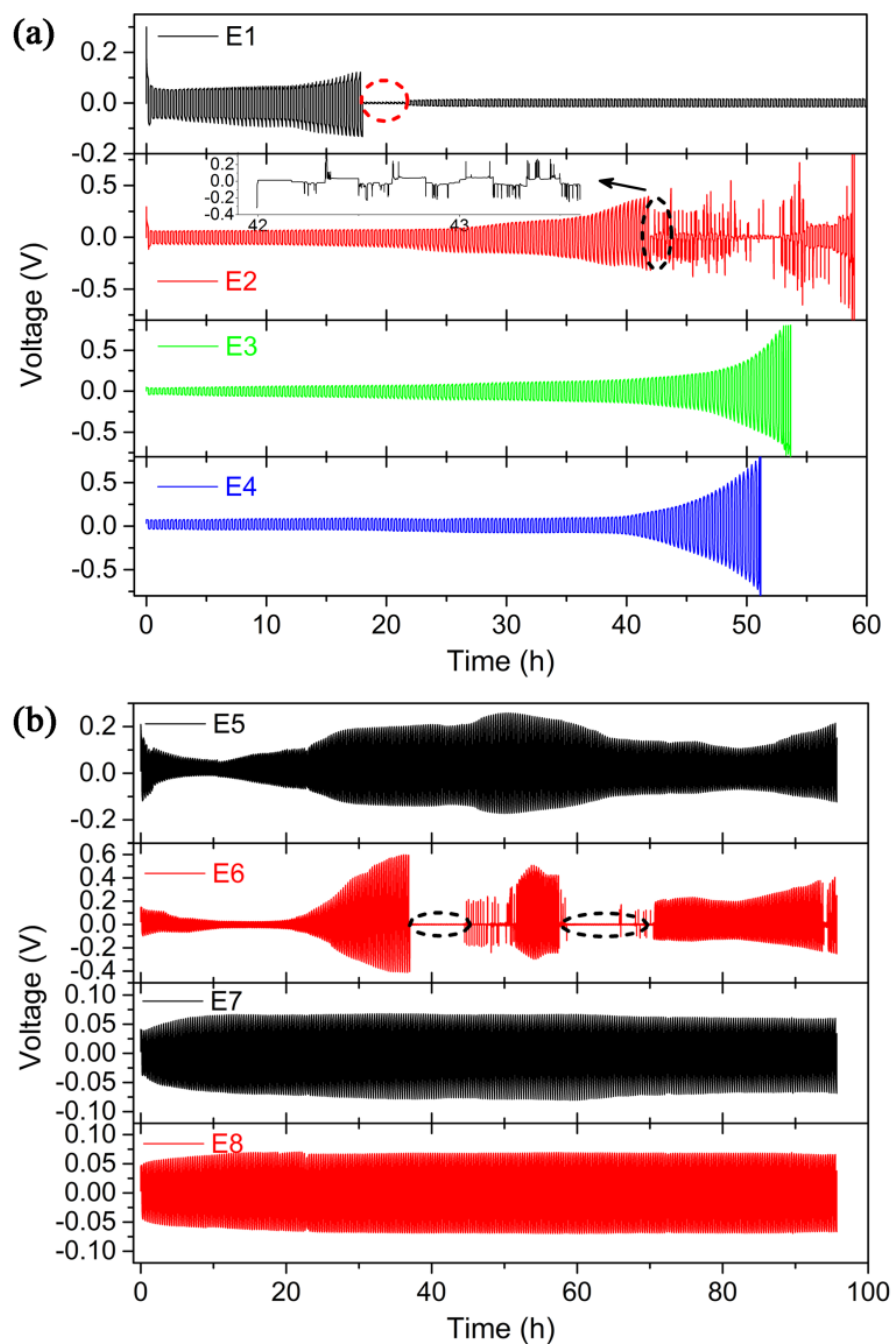


Figure 4.10 Charge/discharge curves of symmetric Zn–Zn cells with different aqueous supporting electrolytes, (a) NH_4Cl solutions range from 0~1.0 M; (b) BMImCl and CaCl_2 solutions with/without NH_4Cl . The circles inside indicate the short circuit during charge/discharge test.

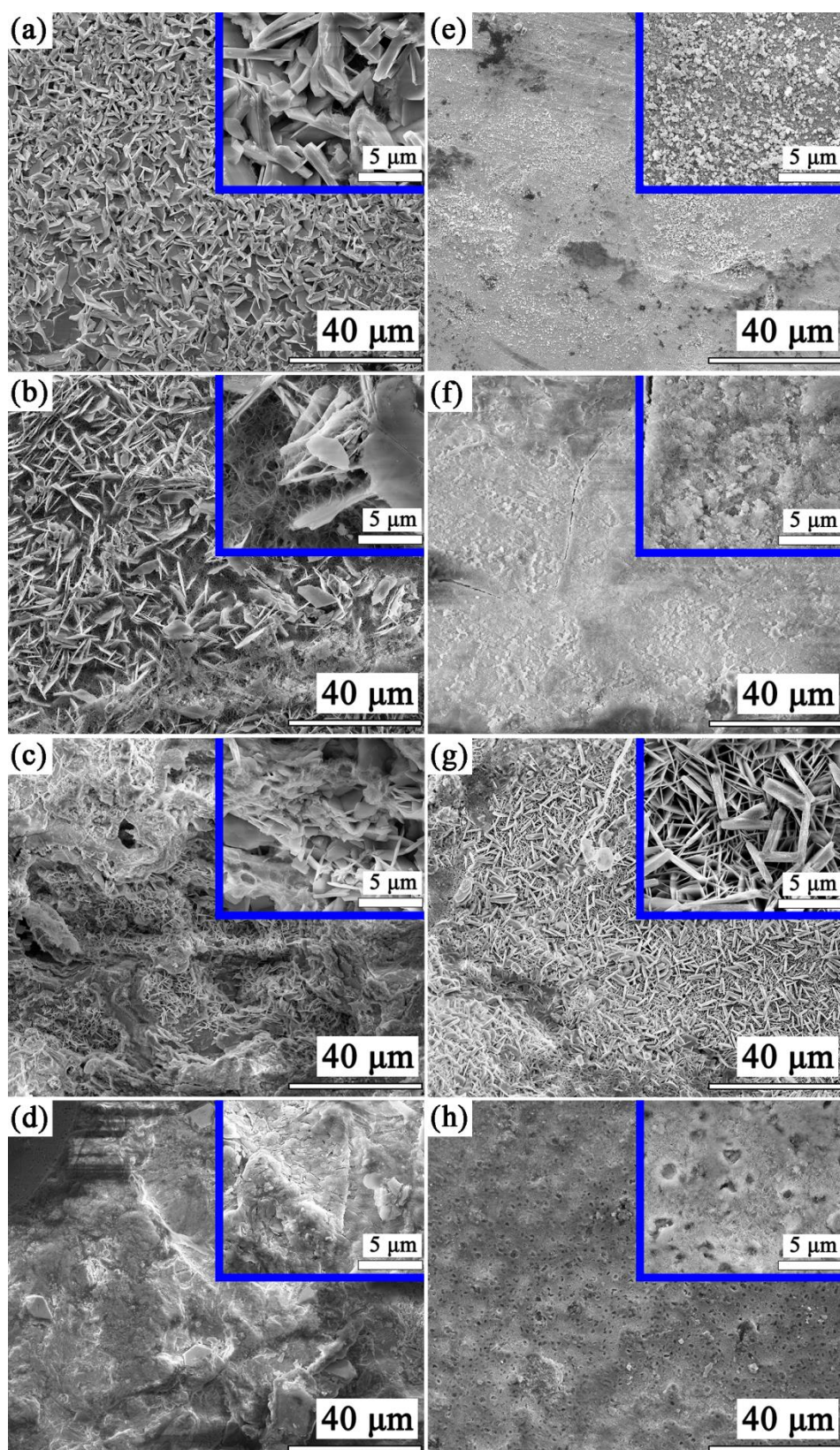


Figure 4.11 SEM images of the Zn metal in symmetric Zn–Zn cells after charge/discharge curves with different supporting electrolytes (E1~E8), (a) E1, (b) E2, (c) E3, (d) E4, (E) E5, (F) E6, (G) E7, (H) E8. Inset shows the corresponding enlarged images.

Zinc dendrites accumulated during the plating process remain a potential risk for short circuit in all zinc-based rechargeable batteries. Symmetric Zn–Zn cells have been applied to study the influence of different supporting electrolytes in zinc plating/stripping process. Short circuit happened after only 18 hours in the Zn–Zn cell with supporting electrolyte E1 (0.1 M ZnCl₂ in deionized water), as shown in Figure 4.10a. Severe zinc dendrites (Figure 4.11a) can be observed by SEM. After addition of NH₄Cl, the running time of Zn–Zn cell can last for more than two days. While lamellar zinc metal formed in supporting electrolytes of E2 (0.2 M NH₄Cl) and E3 (0.5 M NH₄Cl) in Figure 4.11b and c, only bulk zinc metal can be observed (Figure 4.11d) with supporting electrolyte (E4) of 1.0 M NH₄Cl. In the BMImCl/H₂O (8 m) supporting electrolyte, the initial potential gap can be as high as 0.3 V without NH₄Cl (E5 in Figure 4.10b), no lamellar zinc but only massive sub-micron zinc particles can be observed (Figure 4.11e). When 0.5 M NH₄Cl was added in BMImCl/H₂O (8 m) (E6 in Figure 4.10b), the potential gaps reduced clearly in the first 20 hours, whereas short circuit happened after 37 hours, slight zinc needles can be seen in Figure 4.11f. The Zn–Zn cells with aqueous CaCl₂ supporting electrolytes (E7 and E8) showed stable charge/discharge curves for more than 95 hours with potential gaps only 0.16 V (Figure 4.10b). When NH₄Cl-free CaCl₂ supporting electrolyte (E7) was utilized, zinc dendrites with smaller size comparing that with E1 are observed in Figure 4.11g. However, no obvious zinc dendrites but only bulk zinc metal with random “holes” can be observed in the electrode of Zn–Zn cell with E8 (Figure 4.11h). Therefore, aqueous CaCl₂ solution with NH₄Cl can be considered as preferable supporting electrolyte for zinc plating/stripping.

After optimization of the compositions of catholyte and anolyte, BMImCl/H₂O (8 m) with 1.0 M HCl and CaCl₂/H₂O (3.5 m) with 0.5 M NH₄Cl were used as supporting electrolytes for catholyte and anolyte, respectively. It should be noted that complexes of FeCl₄²⁻, FeCl₄⁻, Fe₃Cl₇⁻ and Fe₂Cl₇⁻ may form in solutions containing Fe(III)/(II) chloride and BMImCl. However, it is yet unable to determine the accurate molar ratios and how stable the complexes are.^[128,163] A zinc–iron hybrid flow battery is built with the Fe-based and Zn-based redox active species, as well as the

corresponding supporting electrolytes. The catholyte and anolyte are separated by an anion exchange membrane ($\sim 40 \mu\text{m}$ thick).^[15]

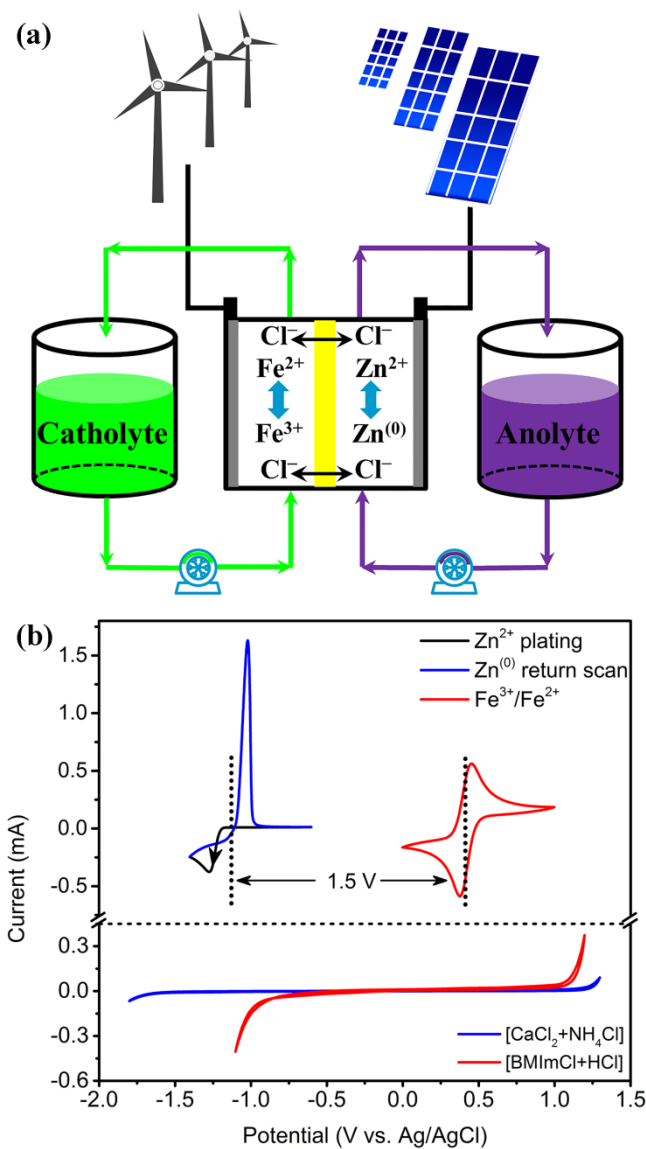
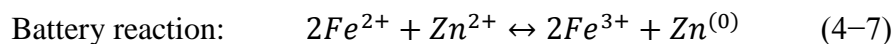
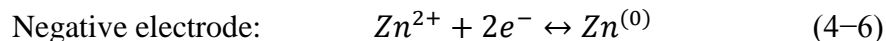
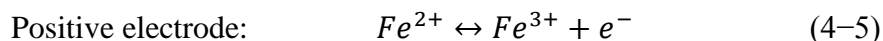


Figure 4.12 Schematic illustration of a Zn–Fe hybrid flow battery (a); (b) top: CV curves of 10 mM ZnCl_2 and 50 mM FeCl_2 in $\text{CaCl}_2/\text{H}_2\text{O}$ (3.5 m) with 0.5 M NH_4Cl and $\text{BMImCl}/\text{H}_2\text{O}$ (8 m) with 1.0 M HCl , respectively; bottom: ESWs of the supporting electrolytes, scan rates: 20 mV s^{-1} .

The scheme of a Zn–Fe hybrid flow battery is illustrated in Figure 4.12a. In the charge process, the Fe(II) ions are oxidized to Fe(III) ions, while the Zn^{2+} ions are reduced to Zn metal and deposited on the graphite felt, concurrently, the charge carriers of chloride ions transfer from anolyte to catholyte to complete the circuit, and

vice versa in the discharge process. The overall redox reactions are given below based on the dominant active species:



The redox activities of Fe-based and Zn-based redox active species in the corresponding supporting electrolytes are presented in Figure 4.12b. It can be found from the CV curves that both the Fe-based and Zn-based active species show high redox reversibility in the stable potential regions of their supporting electrolytes. Consequently, a Zn–Fe hybrid flow battery is designed with an average voltage of ~1.5 V, according to the difference between the redox potentials of Fe-based and Zn-based active species.

4.4 Kinetic analyses of Zn-based and Fe-based redox active species

The effect of NH_4Cl on zinc plating/stripping process in deionized water (without BMImCl) was investigated. As shown in Figure 4.13a, the CV curves of zinc plating/stripping in deionized water present much lower overpotential and stronger redox peaks than those in BMImCl/ H_2O (8 m), even without addition of NH_4Cl . Furthermore, the CV curves exhibit totally different nucleation loops (see the arrows in Figure 4.13a) with higher peak currents, indicating different nucleation behavior.^[175] After addition of different amount of NH_4Cl , the CV curves are almost overlapped, the nucleation hystereses decrease significantly, and the redox peaks sharpen obviously, confirming that the existence of NH_4Cl can facilitate zinc plating/stripping remarkably. The enhanced redox activity of zinc species can be ascribed to the weak acidic environment^[167,175] provided by NH_4Cl solutions (pH of 4.6 for 1.0 M NH_4Cl at room temperature).

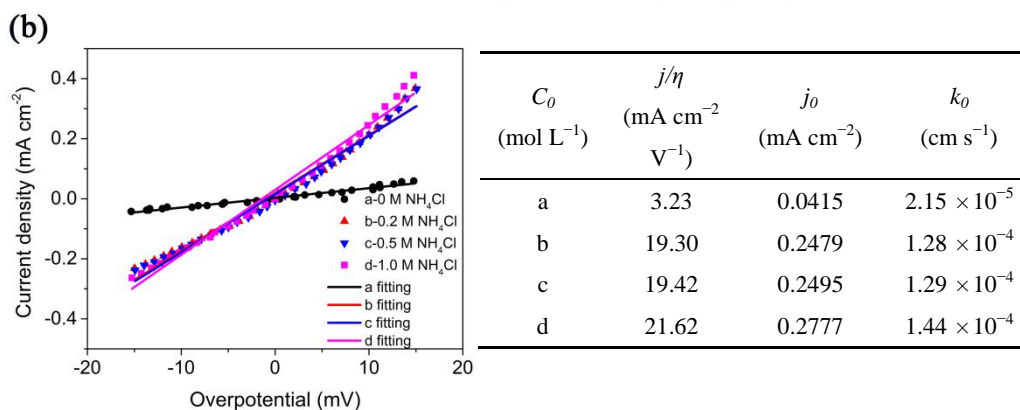
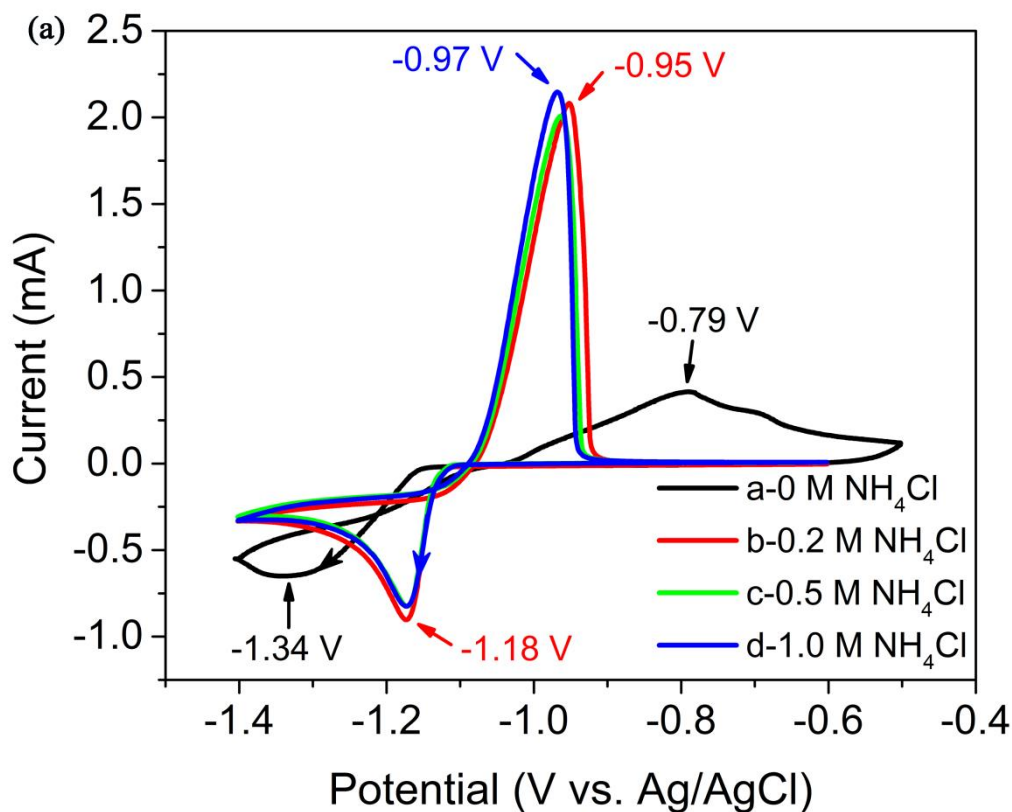


Figure 4.13 (a) CV curves of 10 mM ZnCl₂ in different aqueous NH₄Cl solutions; (b) current densities of zinc plating/stripping versus overpotentials and the corresponding standard rate constant (right table), a: 0 M NH₄Cl; b: 0.2 M NH₄Cl; c: 0.5 M NH₄Cl; d: 1.0 M NH₄Cl.

To investigate the kinetics of zinc plating/stripping, the relationship between overpotential (η) and current (i) is described according to the approximated Butler-Volmer equation, as shown in equation 4–1. *Note: in Allen Bard's electrochemistry book,^[133] reduction (cathodic) currents are taken as positive, here we take the popular way to define oxidation (anodic) currents as positive.*

$$i = i_0[e^{(1-\alpha)f\eta} - e^{-\alpha f\eta}] \quad (4-1)$$

where $f = nF/(RT)$, the current density (j) is defined as $j = i/A$,

At small overpotentials, $\eta \rightarrow 0$, then $e^\eta \rightarrow 1 + \eta$, equation 4-1 can be simplified as

$$i = i_0 f \eta = i_0 \eta n F / (RT) \quad (4-2)$$

At equilibrium potential, the net current is zero, where the exchange current

$$i_0 = n F A k^0 C_0 \quad (4-3)$$

$$\text{or } j_0 = n F k^0 C_0 \quad (4-4)$$

The parameters involved in the equations are defined as follows: α is the charge transfer coefficient, η is the overpotential (V), R is the universal gas constant (8.314 J K⁻¹ mol⁻¹), T is the absolute temperature (298.15 K), n is the number of transferred electrons, F is Faraday constant (96,485 C mol⁻¹), i_0 and j_0 are the exchange current (mA) and current density (mA cm⁻²) at the equilibrium potential, respectively, A is the active area of the electrode (cm²), k^0 is the standard rate constant (cm s⁻¹), and C_0 is the concentration of the active species (mol L⁻¹).

The current densities versus overpotentials are linearly fitted in Figure 4.13b, the standard rate constants can be calculated according to the equations above. The results are shown in the right table in Figure 4.13. Without addition of NH₄Cl, the exchange current density is quite low, with corresponding standard rate constant k^0 of 2.15×10^{-5} cm s⁻¹. By contrast, after addition of NH₄Cl, the standard rate constants are one order higher up to 1.44×10^{-4} cm s⁻¹, indicating much faster kinetics in zinc plating/stripping process.^[175] Therefore, the addition of NH₄Cl is favorable to reduce the nucleation barrier for zinc plating/stripping.

The electrochemical performance of the Zn–Fe hybrid flow battery is related to the redox activities of Fe-based and Zn-based redox active species. To study the kinetics of zinc plating/stripping in different aqueous supporting electrolytes, the kinetic analysis of zinc plating/stripping is conducted afterwards. As discussed before, the addition of NH₄Cl can promote zinc plating/stripping process. The comparison of current densities versus overpotentials in different supporting electrolytes containing 0.5 M of NH₄Cl for zinc plating/stripping is given in Figure 4.14. The corresponding standard rate constants are calculated according to the method as before. The standard

rate constant of zinc plating/stripping in BMImCl/H₂O is as low as $8.99 \times 10^{-6} \text{ cm s}^{-1}$, more than one order lower than that in aqueous NH₄Cl solution, as shown in the table below Figure 4.14. The sluggish nucleation of zinc can be attributed to the high nucleation barrier, leading to large overpotential,^[125] that is in accordance with the CV results in Figure 4.5. Nevertheless, the standard rate constant reaches $6.92 \times 10^{-5} \text{ cm s}^{-1}$ with aqueous CaCl₂ solution, about one order higher than that in BMImCl/H₂O containing the same amount of NH₄Cl. Even though the standard rate constant in aqueous CaCl₂ solution is slightly lower than that in NH₄Cl solution, the ESWs are much wider and more stable for zinc plating/stripping. Based on the above results, aqueous CaCl₂ solution containing NH₄Cl can be appropriate supporting electrolyte for zinc plating/stripping.

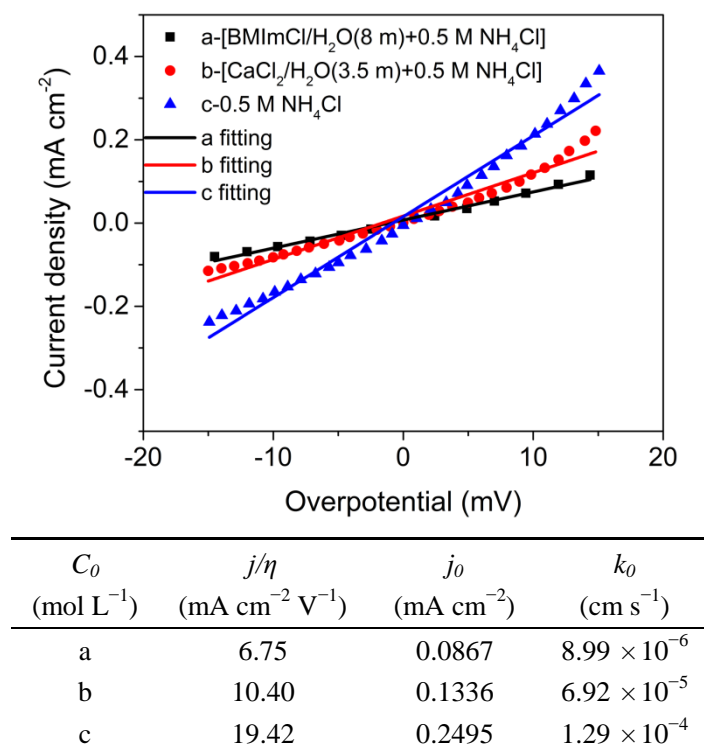


Figure 4.14 Current densities versus overpotentials in zinc plating/stripping with different supporting electrolytes containing 0.5 M NH₄Cl and the corresponding standard rate constants (table below).

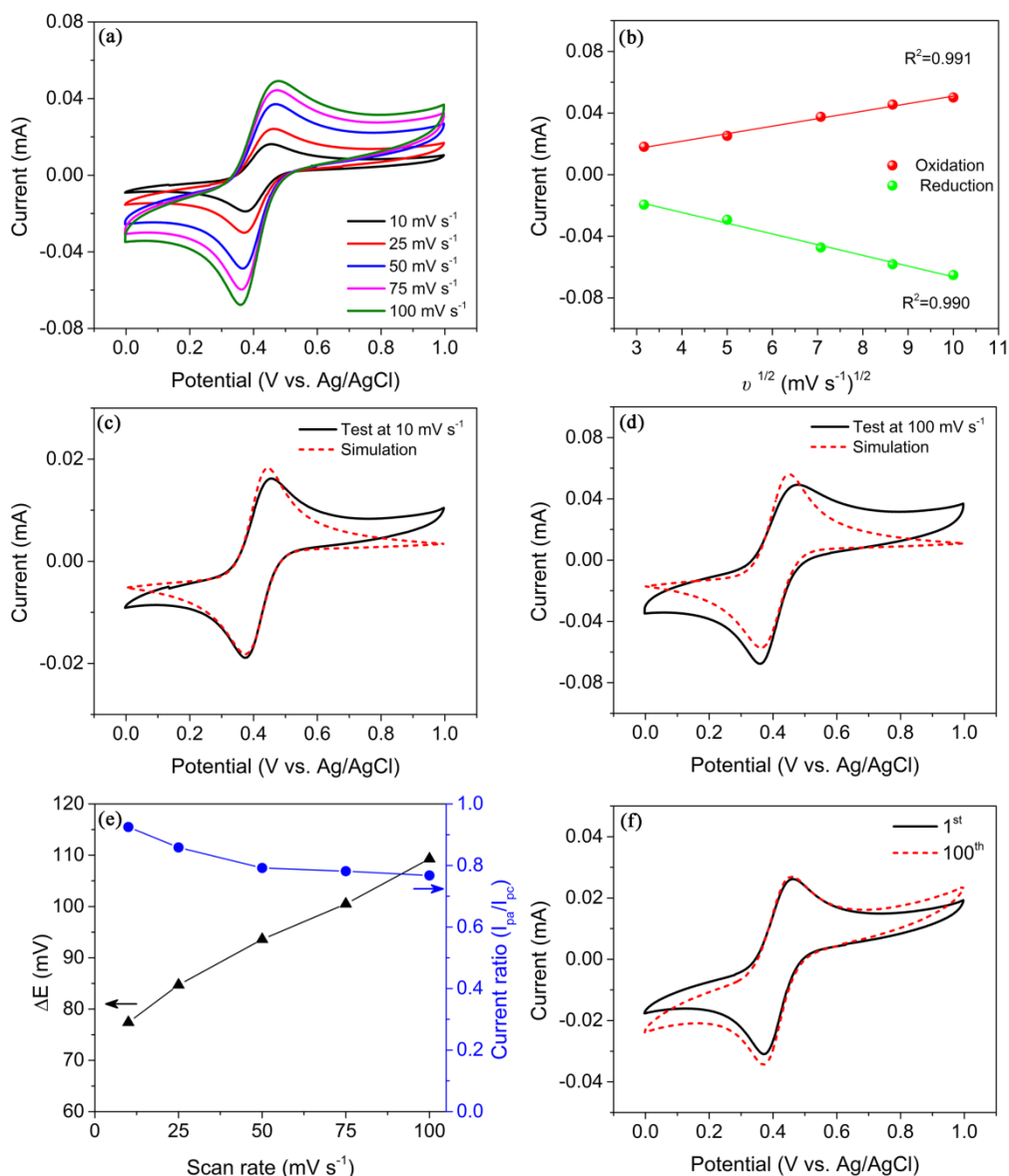


Figure 4.15 CV curves of 1 mM FeCl_2 and 1 mM FeCl_3 in $\text{BMImCl}/\text{H}_2\text{O}$ (8 m) with 1.0 M HCl (a) at various scan rates; (b) peak currents versus square roots of scan rates; (c) and (d) experimental and simulated CV curves at low and high scan rates; (e) peak separation and peak current ratio versus scan rates; (f) CV stability at 20 mV s^{-1} .

As discussed before, the iron active species demonstrate higher redox activity in $\text{BMImCl}/\text{H}_2\text{O}$ solutions than that in deionized water. The redox behavior is further analyzed at different scan rates, as shown in Figure 4.15a, the CV curves show small peak difference even at a high scan rate of 100 mV s^{-1} , indicating high redox reversibility of iron active species. The redox peak currents are linearly fitted with the square roots of scan rates in Figure 4.15b, confirming that the redox reaction of iron active species is dominated by ion diffusion in the electrolyte, according to Randles–

Sevcik equation,^[133] as introduced in chapter 2.3.2. The experimental and simulated CV results are compared in Figure 4.15c and d. At a low scan rate of 10 mV s^{-1} , the CV curves are almost overlapped. However, when the scan rate increases to 100 mV s^{-1} , the peaks in experimental curve shift obviously from the simulated curve, unveiling the evident influence from background currents.^[176]

The redox peak separation and peak current ratios are plotted in Figure 4.15e, it can be seen that the peak separation increases along with the scan rates, showing enlarged electrochemical polarization at higher scan rates. That is in accordance with the peak current ratios, which are close to 1.0 at low and medium scan rates, and decrease slightly to 0.77 at a high scan rate of 100 mV s^{-1} . The redox stability of iron active species is further studied in Figure 4.15f, it can be seen that the CV curves are almost overlapped after 100 cycles, revealing high redox stability in the long-term test.

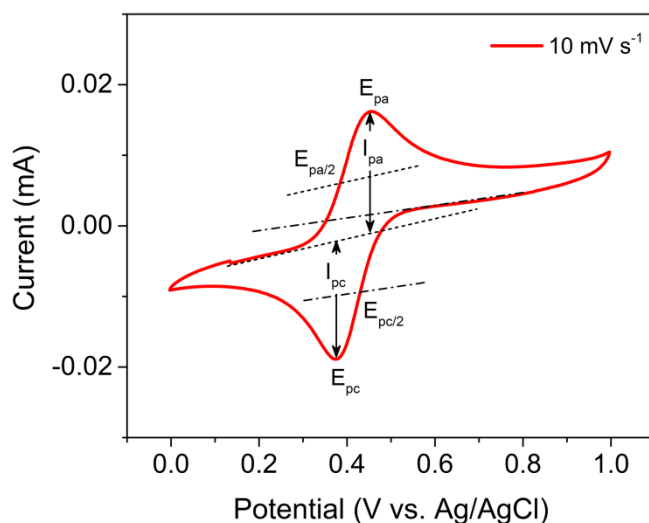


Figure 4.16 Representative CV curve of 1 mM FeCl_2 and 1 mM FeCl_3 in $\text{BMImCl}/\text{H}_2\text{O}$ (8 m) with 1.0 M HCl after calibration with baselines.

Since the redox activity of iron active species is associated with the ion diffusion in $\text{BMImCl}/\text{H}_2\text{O}$ solutions, the diffusion coefficients are calculated after calibration with baselines accordingly.^[176] Figure 4.16 shows the typical analysis method by subtraction of background currents at a scan rate of 10 mV s^{-1} . Similar process is conducted for the CV results at different scan rates. After subtraction of background

currents, the diffusion coefficients of Fe(II) and Fe(III) species are calculated to be $5.53 \times 10^{-6} \text{ cm}^2 \text{ s}^{-1}$ and $6.39 \times 10^{-6} \text{ cm}^2 \text{ s}^{-1}$, respectively, slightly higher than the previous results with ligands of glycine, malic acid, malonic acid and xylitol.^[23]

4.5 Performance of the zinc–iron hybrid flow battery

The ionic conductivities of the catholyte and anolyte were measured at room temperature. As shown in Figure 4.17, the supporting electrolyte for anolyte has the highest ionic conductivity of 190 mS cm^{-1} (0 M ZnCl_2), which is one fold higher than that of the supporting electrolyte for the catholyte (94 mS cm^{-1}). When the concentration of zinc and iron salts increase to 2 M, the ionic conductivities of anolyte and catholyte decrease progressively. The ionic conductivity of zinc species based anolyte is still high (140 mS cm^{-1}), by contrast, the ionic conductivities of FeCl_2 and FeCl_3 based catholytes decrease sharply to 47 mS cm^{-1} and 22 mS cm^{-1} , respectively, which may be associated with the formation of complexes in $\text{BMImCl}/\text{H}_2\text{O}$.^[128,163] Oil-like liquids of 1 v% and 33 v% can be found in the bottom in FeCl_2 and FeCl_3 based catholytes, respectively. However, the molar ratios of accurate compositions of the complexes are unable to determine yet.

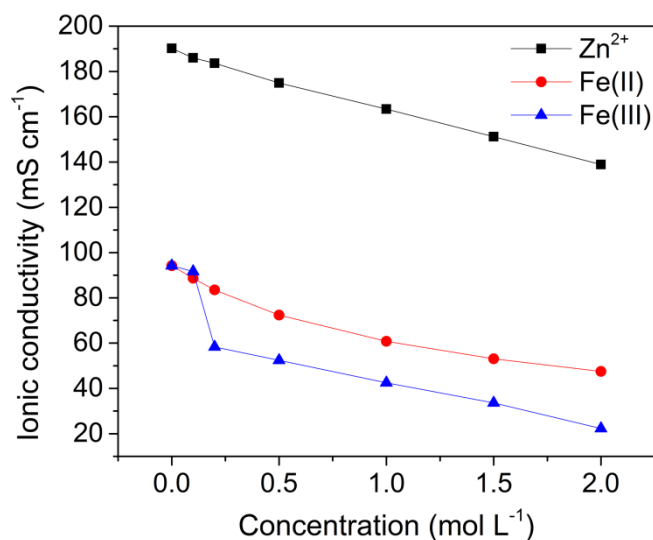


Figure 4.17 Ionic conductivities of iron (III)/(II) chloride in $\text{BMImCl}/\text{H}_2\text{O}$ (8 m) with 1.0 M HCl, and ZnCl_2 in $\text{CaCl}_2/\text{H}_2\text{O}$ (3.5 m) with 0.5 M NH_4Cl , respectively.

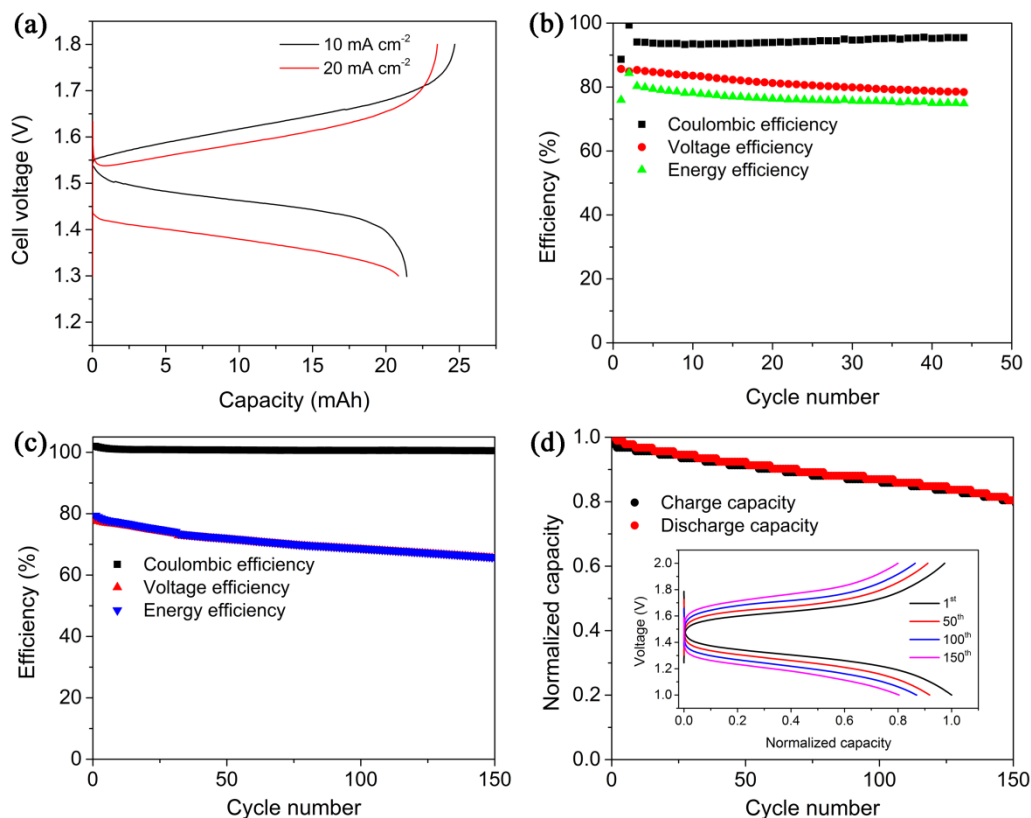


Figure 4.18 Galvanostatic charge/discharge performance of Zn–Fe hybrid flow battery. (a) charge/discharge curves and (b) efficiencies at 20 mA cm^{-2} ; (c) and (d) test in an H-cell at 10 mA (contact area of graphite rod and electrolyte: 0.75 cm^2), inset shows the charge/discharge curves of the Zn–Fe H-cell.

The charge/discharge performance of the Zn–Fe hybrid flow battery was tested with an anion exchange membrane as reported previously.^[15] The charge/discharge curves at different current densities in Figure 4.18a reveal clear plateau with an average voltage of 1.5 V , which is in accordance with the redox potential gap in Figure 4.12b. The cycle performance of the Zn–Fe hybrid flow battery was evaluated at 20 mA cm^{-2} . As shown in Figure 4.18b, the Coulombic efficiency keeps stable at 94% , slightly higher than that with a HAc/NaAc buffer solution;^[167] while the energy efficiency achieves 75% , which is comparable to the Zn–Fe hybrid flow battery with double-membrane and triple-electrolyte design.^[47] Nevertheless, after charge/discharge cycles, the overall resistance increases slightly, as is shown in Figure 4.19, while the slope in the low-frequency region decreases sharply, indicating that the diffusion of charge carriers in the membrane became inefficient along with cycles

in concentrated ionic liquid electrolyte under flushing. A fast charge/discharge test was conducted in a home-made H-cell at a high current of 10 mA (in respect to the reactive surface area of a graphite rod was just 0.75 cm²). The Coulombic efficiency keeps stable at 100% with an initial energy efficiency about 80% (Figure 4.18c). The capacity loss is 0.13% per cycle, to deliver capacity retention of 80% after 150 cycles (Figure 4.18d). The capacity fade can be attributed to the degradation of membrane, since its long-term stability in ionic liquid electrolytes is a problem. Moreover, self-discharge generally exists in RFBs, effective ligands for iron and zinc species can be considered to reduce the self-discharge rate of Zn–Fe hybrid flow battery.^[23] Common electrolytes have also been suggested for Zn–Fe flow battery to improve the performance.^[166] As the membrane is critical for RFBs, further optimization is needed in the future. It should be noted that the overall performance of Zn–Fe hybrid flow battery is dependent on the optimized electrolytes, electrodes, membranes and rational cell design to achieve a performance target which can balance system cost for potential application.

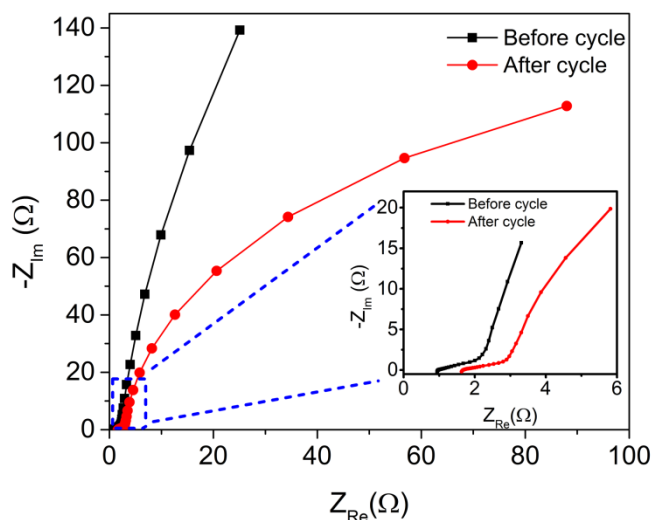


Figure 4.19 EIS of the Zn–Fe hybrid flow battery before and after cycle test at 20 mA cm⁻².

4.6 Conclusions

An aqueous zinc–iron hybrid flow battery has been built with an average voltage of 1.5 V. The optimized compositions of supporting electrolytes for catholyte and anolyte are BMImCl/H₂O (8 m) with 1.0 M HCl and CaCl₂/H₂O (3.5 m) with 0.5 M NH₄Cl, respectively. The corresponding supporting electrolytes exhibit wide ESWs to suppress gas evolution, as well as improve the redox activities of iron and zinc redox active species. The aqueous ionic liquid of BMImCl/H₂O in the catholyte can promote the redox behavior of iron active species with clearly reduced peak separation (71 mV). By contrast, a weak acidic aqueous CaCl₂ solution with NH₄Cl in the anolyte is proved to be a superior supporting electrolyte than BMImCl/H₂O for zinc plating/stripping with low polarization and dendrite-free zinc metal. When the pH of aqueous NH₄Cl (1.0 M) decreases to 4.6, bulk zinc rather than lamellar zinc metal can be observed in the symmetric Zn–Zn cells. Kinetic analysis shows that the standard rate constant of zinc plating/stripping can be increased by one order in aqueous NH₄Cl solution. This non-toxic Zn–Fe hybrid flow battery shows high potential to be next-generation redox flow battery.

5 Aqueous ionic liquid electrolytes towards an organic–inorganic hybrid flow battery

Organic–inorganic redox active species have been introduced for flow batteries.^[13] Hydroquinone (H₂Q) and its derivatives, a group of simple organic active molecules, have been introduced as active materials for static rechargeable batteries and RFBs previously.^[50,90,177] Nevertheless, the low solubility of H₂Q in water becomes a great obstacle to develop aqueous RFBs with high energy density.

In this chapter, aqueous ionic liquid solutions are found to be preferable solvents for H₂Q, in which 5 M of H₂Q can be prepared at room temperature, almost eight times higher than that in water. The redox behavior of H₂Q in aqueous ionic liquid solutions is characterized accordingly. An organic–inorganic hybrid flow battery is designed with H₂Q and zinc chloride in aqueous supporting electrolytes. This hybrid flow battery has an ultrahigh energy density over 220 Wh L⁻¹ theoretically, based on the total volume of catholyte and anolyte, which is among the highest values for aqueous flow batteries to date.^[31] Owing to the commercial availability of these low-cost chemicals, this flow battery system can be considered as a potential substitute for the current zinc–bromine (or zinc–iodine) hybrid flow battery.^[21] Furthermore, our research provides feasible approaches to prepare concentrated electrolytes for RFBs with high energy density.

5.1 Experimental

5.1.1 Preparation and characterization of the electrolytes

Aqueous ionic liquid solutions were prepared by dissolving BMImCl in deionized water at different molalities (unit: mol kg⁻¹, which is abbreviated as “m” hereafter). In the solubility test of H₂Q in BMImCl/H₂O solutions, after thorough dissolution of H₂Q, the total volume of the solution is estimated by a micropipette. A three-electrode system was used to investigate the redox behavior of active species by cyclic

voltammetry (CV) with a Biologic potentiostat (VMP3, France). The working electrode, counter electrode and reference electrode are glassy carbon rod, Pt foil and Ag/AgCl electrode, respectively. Before CV tests of H₂Q, the BMImCl/H₂O solutions were purged with argon or nitrogen gas for 30 min.

5.1.2 Flow battery tests

Graphite felts (GFD 4.6 EA, SGL Carbon Group, Germany) after thermal treatment at 450 °C in air for 6 h were utilized as working electrodes. The geometric area of each graphite felt is 2×2 cm². A composite membrane made of polyvinylidene difluoride (PVDF) and Nafion was used for this organic–inorganic hybrid flow battery. Briefly, a Nafion NR212 membrane was cut into pieces and dried at 70 °C overnight, then 0.18 g of Nafion NR212 was dissolved in dimethylformamide (DMF) at 80 °C, equal amount of PVDF (Nafion NR212:PVDF=1:1, weight ratio) was added accordingly. The homogeneous solution was then pour into a petri dish and dried at 140 °C thoroughly, after cooling down to room temperature, deionized water was added into the petri dish to peel off the composite membrane.^[42] The PVDF/Nafion membrane (~28 μm thick) was pretreated in 3 wt% H₂O₂ at 80 °C for 2 h, then in 0.5 M H₂SO₄ at 80 °C for 2 h, and lithiated in 1.0 M LiOH at 80 °C for 4 h. Afterwards the pretreated PVDF/Nafion membrane was used to assemble the flow cell. Each reservoir contained 10 mL of electrolytes. The electrolytes were circulated by a peristaltic pump (Ismatec REGLO, Germany) at a flowing rate of 30 mL min⁻¹.

5.2 Development of an organic–inorganic hybrid flow battery

As discussed in chapter 1, the energy density of a RFB is highly dependent on the concentration of redox active species, as well as transferred electron number in redox reactions. Despite the merits of low cost and fast redox kinetics of H₂Q, the energy densities of H₂Q-based RFBs in previous reports are still quite low, due to the low solubility of H₂Q in the supporting electrolytes.^[50,90,177] As can be seen in Figure 5.1, the concentration of H₂Q in water is ~0.6 M; by contrast, it can be easily increased to 4.3 M in BMImCl/H₂O (5 m) at room temperature. Surprisingly, the concentration of

H₂Q can be further increased to 5 M in BMImCl/H₂O (10 m) with good flowability, which is about eight folds higher than that in water. That is to say, the BMImCl/H₂O solutions can be preferable solvents for H₂Q. The ultrahigh solubility of H₂Q in BMImCl/H₂O solutions is associated with the solvation free energy change (ΔG_{sol}^0),^[76] as well as the interaction between H₂Q and imidazolium cations.^[119] As is known, BMImCl can dissolve conventionally-insoluble cellulose to reach a weight ratio up to 25%, by break the hydrogen bonding networks in cellulose.^[119] Similar disruption of intermolecular hydrogen bonds in H₂Q could occur in BMImCl/H₂O solutions.

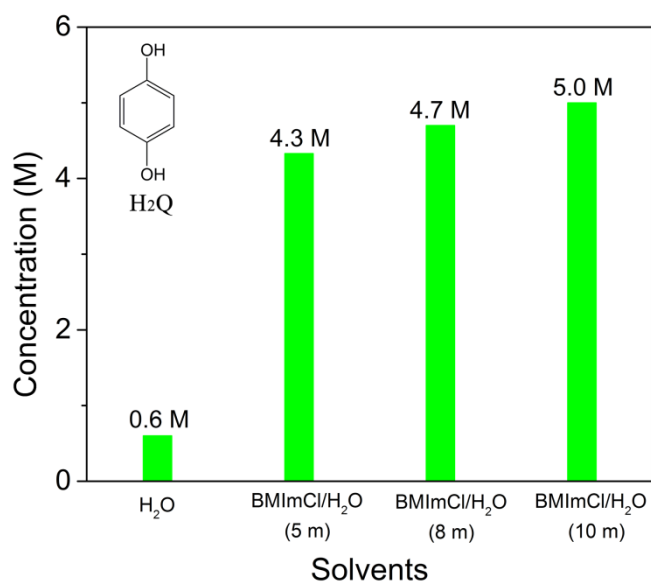


Figure 5.1 Concentration of H₂Q in different molalities of BMImCl/H₂O solutions. The concentration is calculated based on the total volume after thorough dissolution of H₂Q, e.g. 9 mmol H₂Q can be dissolved in 1 mL of BMImCl/H₂O (10 m) with total volume of 1.8 mL.

The redox behavior of H₂Q was characterized in different molalities of BMImCl/H₂O solutions accordingly. It can be observed that the redox potentials vary with the molalities of BMImCl/H₂O solutions in Figure 5.2. With the molalities of BMImCl/H₂O solutions increase, the redox peak currents of H₂Q decrease obviously, meanwhile the peak separation enlarges successively (Figure 5.2a). Previous reports indicate that the redox behavior of H₂Q is highly dependent on the pH of supporting electrolytes, the redox potentials shift negatively with the pH increases.^[177] The pH of

BMIImCl/H₂O solutions we use here is around 8. When the molality of BMIImCl/H₂O solution increases from 5 m to 10 m, the redox peak separation in the CV curves increases from 385 mV to 503 mV in Figure 5.2b, which can be ascribed to the increased electrochemical polarization in the corresponding electrolytes, since the ionic conductivities of the BMIImCl/H₂O solutions are much lower than the conventional inorganic salts based aqueous solutions, as measured in chapter 3.

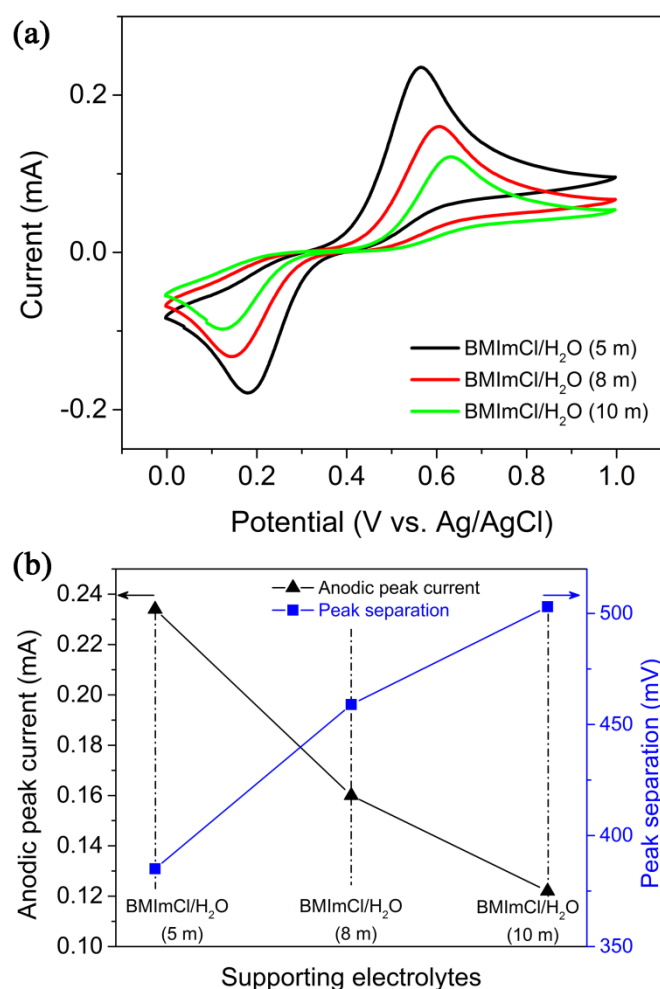


Figure 5.2 Redox behavior of H₂Q in different molality of BMIImCl/H₂O, (a) CV curves at 20 mV s⁻¹; and (b) the corresponding anodic peak currents as well as the peak separation.

However, the intermediates of H₂Q in redox process can be quite complicated, since they are highly sensitive to the additives and pH of electrolytes.^[178-180] As a representative organic active molecule with two transferred electrons in the redox

reactions, H_2Q has been reported with one or two pairs of redox peaks in the CV curves.^[87,177] The influence of LiCl additive on the redox behavior was characterized. With different amount of LiCl addition in the BMImCl/ H_2O (5 m) solution, the CV curves are almost overlapped in Figure 5.3a. Therefore, the addition of LiCl has no obvious influence on the redox activity of H_2Q , LiCl is then added to the BMImCl/ H_2O (5 m) solution to improve the ionic conductivity and provide Li^+ ions as charge carriers.

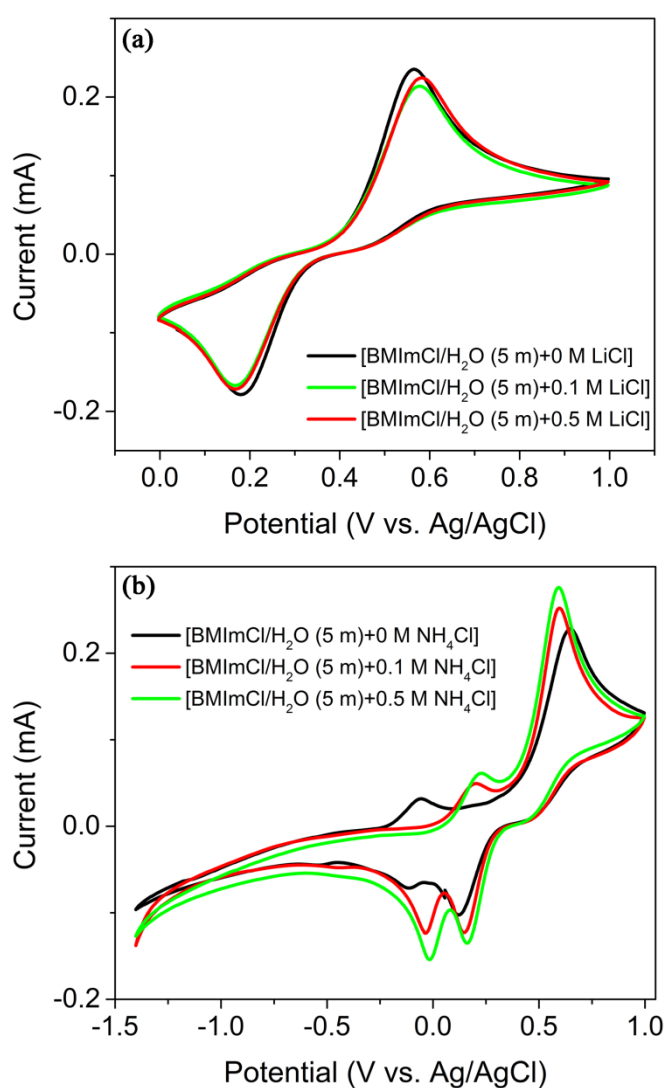


Figure 5.3 CV curves of 10 mM H_2Q in BMImCl/ H_2O (5 m) with different additives: (a) LiCl and (b) NH_4Cl .

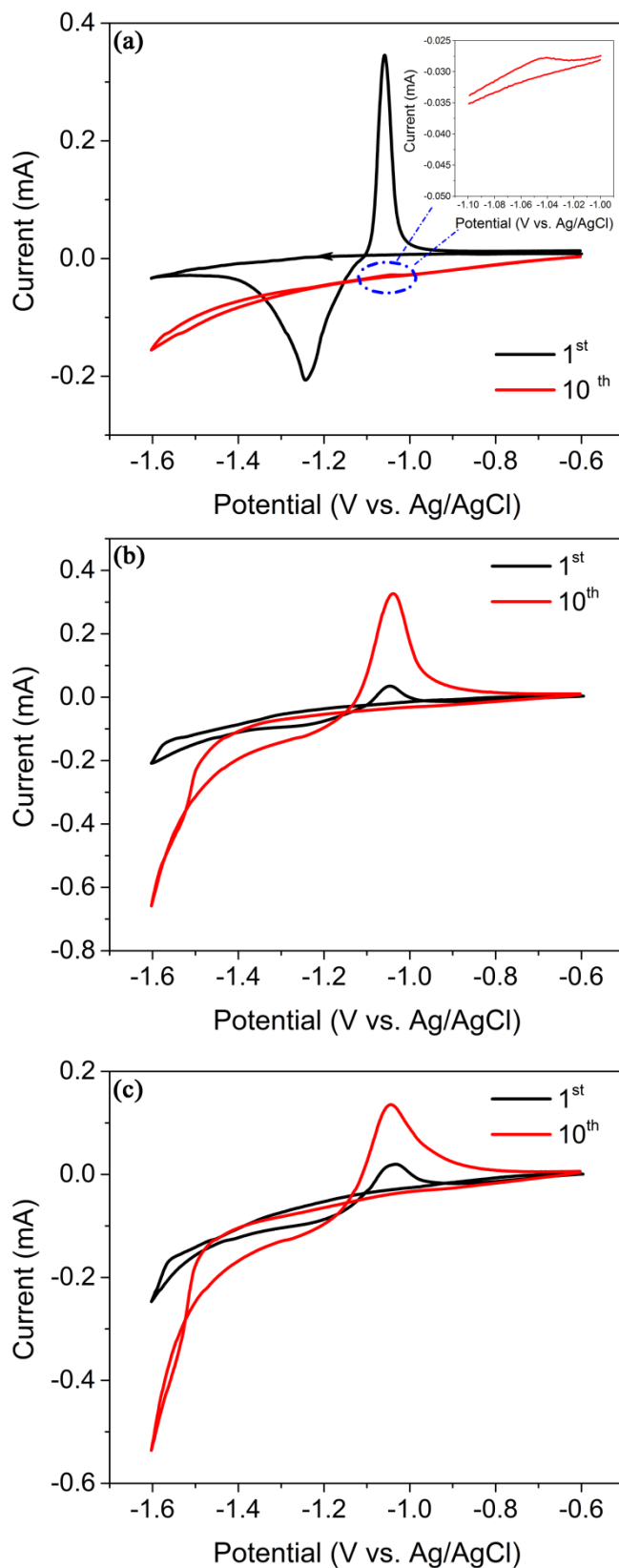


Figure 5.4 CV curves of ZnCl₂ in BMImCl/H₂O (5 m) with different amount of NH₄Cl, (a) 0 M NH₄Cl; (b) 0.2 M NH₄Cl; (c) 0.5 M NH₄Cl.

When Bronsted acid of NH₄Cl was added into the electrolyte of BMImCl/H₂O (5

m), the CV curves of H_2Q are quite different. Two pairs of redox peaks become more obvious with the increase of NH_4Cl addition (Figure 5.3b). The different redox peaks can be associated with protons and intermediates in the electrolytes during redox process of H_2Q .^[178,179] The CV curves have been further scanned to more negative region to investigate if side reactions happen. However, no obvious redox peaks can be observed in the region from -1.5 to -0.2 V vs. Ag/AgCl.

Zinc plating/stripping was investigated in BMImCl/ H_2O (5 m) solution afterwards. As is shown in Figure 5.4a, without addition of NH_4Cl , the redox peaks of zinc plating/stripping in the 1st cycle are observed clearly, however, the peak currents decrease sharply along with cycles. In the 10th cycle, the redox peaks are almost invisible. In contrast, when different amount of NH_4Cl is added, the redox peak currents in the first cycle weaken slightly, and then increase gradually in the successive cycles (Figure 5.4b and c). Therefore, the addition of NH_4Cl can promote zinc plating/stripping in BMImCl/ H_2O (5 m) solution, which is in accordance with the previous results in chapter 4.

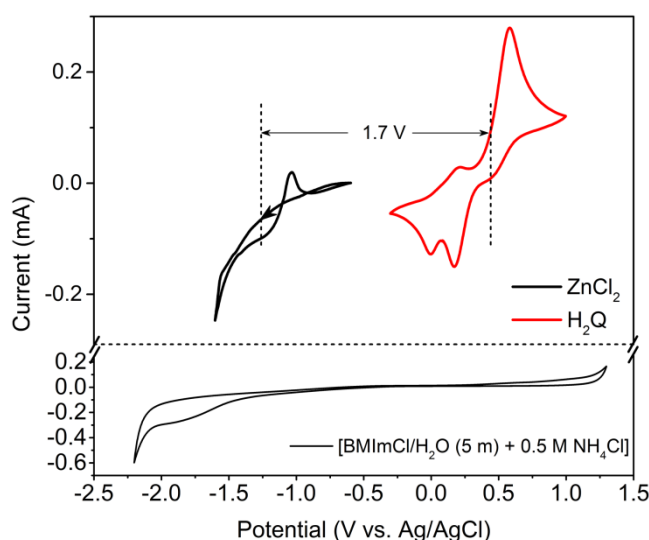


Figure 5.5 CV curves of 25 mM ZnCl_2 and 10 mM H_2Q in the supporting electrolyte of BMImCl/ H_2O (5 m) containing 0.5 M NH_4Cl .

An organic–inorganic hybrid flow battery was then designed with H_2Q and ZnCl_2 in the BMImCl/ H_2O solution. Figure 5.5 shows the CV curves of the positive and

negative active species in corresponding supporting electrolyte. The ESW of the supporting electrolyte is still stable for redox reactions of H₂Q and ZnCl₂. An average voltage of ~1.7 V can be realized in this aqueous organic–inorganic hybrid flow battery from the redox potential difference, which is slightly higher than that in previous result.^[89] Considering the high concentration and two-electron redox reaction, this organic–inorganic hybrid flow battery has an ultrahigh theoretical energy density over 220 Wh L⁻¹ based on the total volume of the catholyte and anolyte, which is more than eight times of the current VRFBs, and two times higher than the zinc–polyiodide hybrid flow batteries.^[30,31]

Initial investigation on the H₂Q–ZnCl₂ hybrid flow battery was conducted with Nafion based membranes. The PVDF/Nafion composite membrane shows much lower swelling ratio than Nafion membranes in Table 5.1. Flow cells were first assembled with Nafion membranes, but this battery could not work well with Nafion N117 (~4.2 Ω in the corresponding supporting electrolyte) even at a low current density of ±1.0 mA cm⁻², because of insufficient free charge carriers to complete the circuit. However, when Nafion NR212 was used, serious crossover happened after several cycles because of its high swelling ratio.

Table 5.1 Physical properties of Nafion based membranes.

Membranes	Thickness (μm)	Length (swelling ratio)	Width (swelling ratio)
Nafion N117	178	7.1%	19.0%
Nafion NR212	50.8	9.5%	9.5%
NR212/PVDF (lithiation)	28.6	3.6%	4.3%

Afterwards a PVDF/Nafion composite membrane was adopted for the H₂Q–ZnCl₂ hybrid flow battery. Obvious plateau can be found in the charge/discharge curves in Figure 5.6, the voltage efficiency is around 85% after IR drop correction, but the

capacity decreases clearly along with cycles. The Coulombic efficiency of the H₂Q–ZnCl₂ hybrid flow battery increases from 58% to 80% as the discharge capacity decreases slower than the charge capacity. The PVDF/Nafion composite membrane shows longer durability in contrast to pure Nafion membranes. However, the progressive capacity loss should be addressed for long-term cycles.

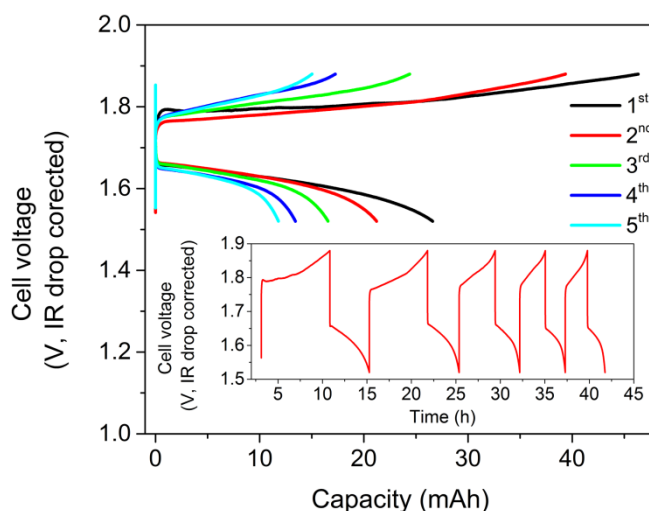


Figure 5.6 Charge/discharge curves of H₂Q–ZnCl₂ hybrid flow battery with a PVDF/Nafion composite membrane at $\pm 1.5 \text{ mA cm}^{-2}$, inset shows the cycle curves. Catholyte: 10 mL of 0.1 M H₂Q in BMImCl/H₂O; anolyte: 10 mL of 0.2 M ZnCl₂ in BMImCl/H₂O, 0.4 M LiCl was used as conductive additive in both catholyte and anolyte.

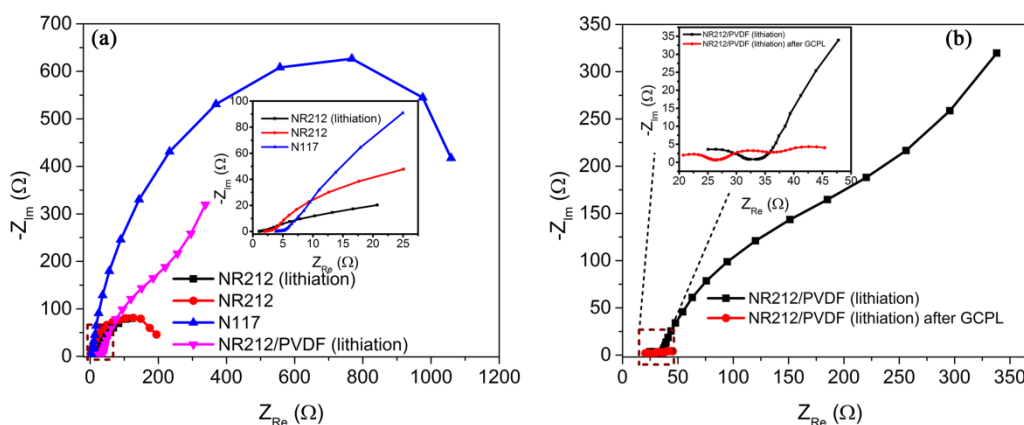


Figure 5.7 EIS curves of the H₂Q–ZnCl₂ hybrid flow battery with Nafion based membranes, (a) before and (b) after galvanostatic cycling test with potential limitation (GCPL).

EIS analysis was carried out before and after cycling test. Even though the overall

resistance of the flow cell with PVDF/Nafion composite membrane ($\sim 20 \Omega$) is much higher than that with Nafion N117 ($\sim 4.2 \Omega$) in Figure 5.7, the flow cell can still run with PVDF/Nafion composite membrane at a low current density of 1.5 mA cm^{-2} while failed with Nafion N117. That is to say, screening of membranes should not only focus on the overall resistance in the flow cell but also the ionic conductivity/mobility of the membranes.^[42] However, as is shown in Figure 5.7b, after cycling test, the slope line in the low frequency region which is associated with the ion diffusion disappears, indicating that the charge carriers (Li^+) in PVDF/Nafion composite membrane become insufficient over cycles. Even though the flow cell can still run after 100 cycles, but the capacity is quite low (not shown here).

After charge/discharge test, the anolyte of the $\text{H}_2\text{Q-ZnCl}_2$ hybrid flow battery was analyzed by CV measurement at the redox potential region of H_2Q . Weak redox peaks of H_2Q intermediates can be observed from the CV curve in Figure 5.8, confirming the crossover of H_2Q intermediates from the catholyte to the anolyte.^[91] Therefore, it is essential to find reliable membranes to mitigate against crossover as well as transfer charge carriers with long-term stability. Molecular modification of H_2Q and utilization of ceramic membranes can be considered as effective approaches to address crossover of H_2Q for further optimization.^[177]

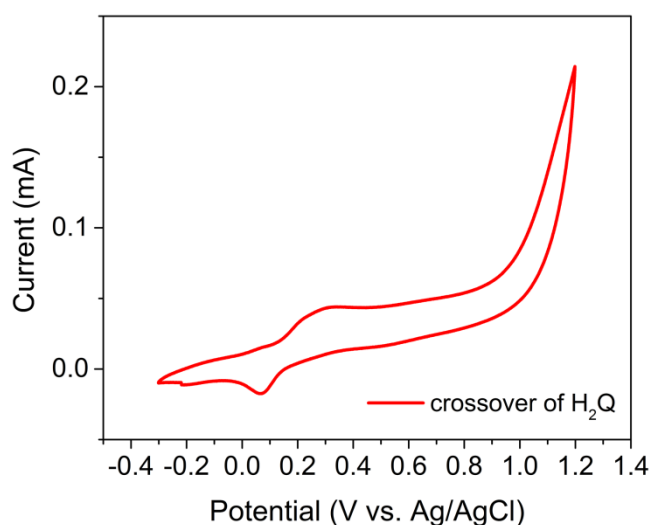


Figure 5.8 CV curve of anolyte in the $\text{H}_2\text{Q-ZnCl}_2$ hybrid flow battery after charge/discharge test.

5.3 Conclusions

An aqueous organic–inorganic hybrid flow battery has been built with hydroquinone and zinc chloride in BMImCl/H₂O based supporting electrolytes. This organic–inorganic hybrid flow battery has an average voltage of 1.7 V. The BMImCl/H₂O is found to be preferable solvent for hydroquinone, in which a concentration of 5 M hydroquinone can be prepared at room temperature. Consequently, this organic–inorganic hybrid flow battery has an ultrahigh energy density over 220 Wh L⁻¹ theoretically. The existence of NH₄Cl can tune the redox behavior of hydroquinone and promote the zinc plating/stripping. Nevertheless, crossover of hydroquinone needs to be addressed for long-term cycles in the future.

6 Summary and outlook

Aqueous electrolytes are primary choices to build safe rechargeable batteries due to the non-flammability. Herein, ionic liquids based aqueous electrolytes have been introduced as supporting electrolytes, reaction media and preferable solvents, respectively, owing to the unique advantages. Different new redox flow batteries have been developed based on aqueous electrolytes with ionic liquids in this PhD study.

Six hydrophilic ILs (imidazolium chloride, quaternary ammonium chloride and imidazolium alkyl sulfate) were selected to prepare “water-in-ionic-liquid” electrolytes. These aqueous electrolytes exhibit wide ESWs from 3 to 4.4 V, with high ionic conductivity up to 80.8 mS cm^{-1} , much higher than the commercial non-aqueous electrolytes for lithium-ion batteries. The varied ionic conductivities and ESWs can be attributed to the interaction of different cations and anions with water molecules. An aqueous $\text{TiO}_2\text{-Fe}^{2+}$ hybrid battery was proposed to demonstrate the application of these ESWs. This $\text{TiO}_2\text{-Fe}^{2+}$ hybrid battery shows an average voltage of 1.7 V and an areal capacity of 0.2 mAh cm^{-2} , confirming the feasibility of “water-in-ionic-liquid” as supporting electrolytes for aqueous high-voltage rechargeable batteries.

Aqueous ionic liquid solutions can not only serve as supporting electrolytes, but also reaction media. The redox activity of $\text{Fe}^{3+}/\text{Fe}^{2+}$ active species can be obviously improved in $\text{BMImCl}/\text{H}_2\text{O}$ solution, with high redox stability and decreased redox potential difference. Accordingly, an aqueous zinc-iron hybrid flow battery has been developed with a FeCl_2 based catholyte and a ZnCl_2 based anolyte. Furthermore, during zinc plating/stripping, aqueous CaCl_2 solution is found to be better supporting electrolyte than $\text{BMImCl}/\text{H}_2\text{O}$ without nucleation hysteresis. Kinetic analyses are conducted on the iron and zinc species, respectively. The diffusion coefficients of Fe^{2+} and Fe^{3+} ions are $5.53 \times 10^{-6} \text{ cm}^2 \text{ s}^{-1}$ and $6.39 \times 10^{-6} \text{ cm}^2 \text{ s}^{-1}$, respectively, after calibration with baselines. The addition of NH_4Cl is beneficial for zinc plating/stripping process, with standard rate constants k^0 of $1.44 \times 10^{-4} \text{ cm s}^{-1}$, which is one order higher than that in $\text{BMImCl}/\text{H}_2\text{O}$. The aqueous zinc-iron hybrid flow battery shows an average voltage of 1.5 V and a high energy efficiency about 80%.

Considering the low cost and non-toxicity of iron and zinc species, this zinc–iron hybrid flow battery is promising for practical application. However, long-term operation needs to be addressed with high-performance membranes in the future.

Ionic liquids are a group of excellent solvents. BMImCl/H₂O solutions are found to be preferable solvents for hydroquinone to realize a concentration of 5 M at room temperature. An aqueous organic–inorganic hybrid flow battery has been designed based on hydroquinone and zinc chloride in the corresponding supporting electrolyte. Unprecedentedly, this aqueous organic–inorganic hybrid flow battery has a theoretical energy density above 220 Wh L⁻¹ with an average voltage of 1.7 V. In spite of the molecular size of hydroquinone and nanochannels in polymeric membranes, further optimization via molecular modification of hydroquinone as well as adoption of ceramic membranes is needed to mitigate against the crossover of hydroquinone.

Therefore, ionic liquids based electrolytes show high potential in next-generation redox flow batteries. Furthermore, organic active species which are highly soluble in ionic liquids can be considered as promising alternatives for the current vanadium compounds in vanadium redox flow battery.

Appendix

Chemical list

Chemicals	Assay	Supplier
1-butyl-3-methylimidazolium chloride (BMImCl)	98%	Aldrich
1-ethyl-3-methylimidazolium chloride (EMImCl)	97%	Acros Organics
1-ethyl-2,3-dimethylimidazolium ethyl sulfate (EMMImEtSO ₄)	94.5%	Fluka
1,2,3-trimethylimidazolium methyl sulfate (TriMImMeSO ₄)	95%	Alfa Aesar
Ammonium chloride (NH ₄ Cl)	99.5%	Sigma Aldrich
Ammonium fluoride (NH ₄ F)	98%	Sigma Aldrich
Calcium chloride dihydrate (CaCl ₂ •2H ₂ O)	99%	Alfa Aesar
Ethylene glycol ((CH ₂ OH) ₂)	99%	Alfa Aesar
glycine betaine (GB)	98%	Alfa Aesar
Hydrochloric acid (HCl)	37%	VWR
Hydroquinone (H ₂ Q)	99%	Alfa Aesar
Iron (III) chloride (FeCl ₃)	97%	Sigma Aldrich
Iron (II) chloride tetrahydrate (FeCl ₂ •4H ₂ O)	97%	Acros Organics
Lithium chloride (LiCl)	99%	Sigma Aldrich
Tetrabutylammonium chloride (TBACl)	98%	Aldrich
Tetraethylammonium chloride (TEACl)	98%	Alfa Aesar
Titanium foil (Ti), 127 µm thick	99.7%	Sigma Aldrich
Zinc chloride (ZnCl ₂)	98%	Alfa Aesar

Publications and activities

Publications

[1] **Y. Zhang**, R. Ye, D. Henkensmeier, R. Hempelmann*, R. Chen*. “Water-in-ionic liquid” solutions towards wide electrochemical stability windows for aqueous rechargeable batteries. *Electrochimica Acta*, 2018, 263, 47.

[2] **Y. Zhang**, D. Henkensmeier, S. Kim, R. Hempelmann*, R. Chen*. Enhanced reaction kinetics of an aqueous Zn–Fe hybrid flow battery by optimizing the supporting electrolytes. *Journal of Energy Storage*, 2019, 25, 100883.

Conferences

[1] **Y. Zhang**, R. Chen, R. Hempelmann. Aqueous electrolytes with ionic liquids for redox flow batteries (poster), *Electrochemistry*, Ulm, Germany, September 2018

[2] **Y. Zhang**, R. Hempelmann, R. Chen. “Water-in-ionic liquid” electrolytes boost aqueous high-voltage rechargeable batteries (poster), *117th General Assembly of the German Bunsen Society for Physical Chemistry*, Hannover, Germany, May 2018.

[3] **Y. Zhang**, R. Hempelmann, R. Chen. Ionic liquid based aqueous electrolytes for redox flow batteries (poster), *116th General Assembly of the German Bunsen Society for Physical Chemistry*, Kaiserslautern, Germany, May 2017.

Out-reach Activities

[1] Hannover Messe, Hannover, Germany, April 2019.

Bibliography

- [1] G. L. Soloveichik. *Chemical Reviews*, 2015, 115, 11533.
- [2] W. Wang, Q. Luo, B. Li, X. Wei, L. Li, Z. Yang. *Advanced Functional Materials*, 2013, 23, 970.
- [3] B. Dunn, H. Kamath, J.-M. Tarascon. *Science*, 2011, 334, 928.
- [4] M. S. Whittingham. *Chemical Reviews*, 2004, 104, 4271.
- [5] <https://www.upsbatterycenter.com/blog/flow-batteries-history/>, 2017.
- [6] W. Kangro. Verfahren zur Speicherung von elektrischer Energie. Germany patent DE914264. 1949.
- [7] J. Winsberg, T. Hagemann, T. Janoschka, M. D. Hager, U. S. Schubert. *Angewandte Chemie International Edition*, 2017, 56, 686.
- [8] M. Skyllas-Kazacos, M. H. Chakrabarti, S. A. Hajimolana, F. S. Mjalli, M. Saleem. *Journal of the Electrochemical Society*, 2011, 158, R55.
- [9] M. Park, J. Ryu, W. Wang, J. Cho. *Nature Reviews Materials*, 2016, 2, 16080.
- [10] B. Li, J. Liu. *National Science Review*, 2017, 4, 91.
- [11] M. Duduta, B. Ho, V. C. Wood, P. Limthongkul, V. E. Brunini, W. C. Carter, Y.-M. Chiang. *Advanced Energy Materials*, 2011, 1, 511.
- [12] E. C. Montoto, G. Nagarjuna, J. Hui, M. Burgess, N. M. Sekerak, K. Hernández-Burgos *et al.* *Journal of the American Chemical Society*, 2016, 138, 13230.
- [13] B. Huskinson, M. P. Marshak, C. Suh, S. Er, M. R. Gerhardt, C. J. Galvin *et al.* *Nature*, 2014, 505, 195.
- [14] K. Schmidt-Rohr, Q. Chen. *Nature Materials*, 2008, 7, 75.
- [15] Z. Chang, D. Hakensmeier, R. Chen. *ChemSusChem*, 2017, 10, 3193.
- [16] T. Liu, X. Wei, Z. Nie, V. Sprenkle, W. Wang. *Advanced Energy Materials*, 2016, 6, 1501449.
- [17] W. Lu, Z. Yuan, Y. Zhao, H. Zhang, H. Zhang, X. Li. *Chemical Society Reviews*, 2017, 46, 2199.
- [18] W. Li, Z. Zhang, Y. Tang, H. Bian, T.-W. Ng, W. Zhang, C.-S. Lee. *Advanced Science*, 2015, 3, 1500276.
- [19] A. Ejigu, M. Edwards, D. A. Walsh. *ACS Catalysis*, 2015, 5, 7122.
- [20] H. Zhou, Y. Shen, J. Xi, X. Qiu, L. Chen. *ACS Applied Materials & Interfaces*, 2016, 8, 15369.
- [21] C. Wang, Q. Lai, P. Xu, D. Zheng, X. Li, H. Zhang. *Advanced Materials*, 2017, 29, 1605815.
- [22] M. Ulaganathan, V. Aravindan, Q. Yan, S. Madhavi, M. Skyllas-Kazacos, T. M. Lim. *Advanced Materials Interfaces*, 2015, 3, 1500309.
- [23] K. L. Hawthorne, J. S. Wainright, R. F. Savinell. *Journal of the Electrochemical Society*, 2014, 161, A1662.
- [24] M. G. Verde, K. J. Carroll, Z. Wang, A. Sathrum, Y. S. Meng. *Energy & Environmental Science*, 2013, 6, 1573.
- [25] L. Li, S. Kim, W. Wang, M. Vijayakumar, Z. Nie, B. Chen *et al.* *Advanced Energy Materials*, 2011, 1, 394.

- [26] M. Skyllas-Kazacos, L. Cao, M. Kazacos, N. Kausar, A. Mousa. *ChemSusChem*, 2016, 9, 1521.
- [27] W. Wang, S. Kim, B. Chen, Z. Nie, J. Zhang, G.-G. Xia *et al.* *Energy & Environmental Science*, 2011, 4, 4068.
- [28] Y. K. Zeng, T. S. Zhao, L. An, X. L. Zhou, L. Wei. *Journal of Power Sources*, 2015, 300, 438.
- [29] W. Wang, Z. Nie, B. Chen, F. Chen, Q. Luo, X. Wei *et al.* *Advanced Energy Materials*, 2012, 2, 487.
- [30] B. Li, Z. Nie, M. Vijayakumar, G. Li, J. Liu, V. Sprenkle, W. Wang. *Nature Communications*, 2015, 6, 6303.
- [31] G.-M. Weng, Z. Li, G. Cong, Y. Zhou, Y.-C. Lu. *Energy & Environmental Science*, 2017, 10, 735.
- [32] J. Zhang, G. Jiang, P. Xu, A. Ghorbani Kashkooli, M. Mousavi, A. Yu, Z. Chen. *Energy & Environmental Science*, 2018, 11, 2010.
- [33] C. Xie, H. Zhang, W. Xu, W. Wang, X. Li. *Angewandte Chemie International Edition*, 2018, 57, 11171.
- [34] Q. Huang, Q. Wang. *ChemPlusChem*, 2015, 80, 312.
- [35] Z. Li, G. Weng, Q. Zou, G. Cong, Y.-C. Lu. *Nano Energy*, 2016, 30, 283.
- [36] H. Chen, Y.-C. Lu. *Advanced Energy Materials*, 2016, 6, 1502183.
- [37] J. J. Biendicho, C. Flox, L. Sanz, J. R. Morante. *ChemSusChem*, 2016, 9, 1938.
- [38] S. Mubeen, Y.-s. Jun, J. Lee, E. W. McFarland. *ACS Applied Materials & Interfaces*, 2016, 8, 1759.
- [39] Q. Wang, S. M. Zakeeruddin, D. Wang, I. Exnar, M. Grätzel. *Angewandte Chemie International Edition*, 2006, 45, 8197.
- [40] R. Yan, Q. Wang. *Advanced Materials*, 2018, 30, 1802406.
- [41] J. Yu, L. Fan, R. Yan, M. Zhou, Q. Wang. *ACS Energy Letters*, 2018, 3, 2314.
- [42] C. Jia, F. Pan, Y. G. Zhu, Q. Huang, L. Lu, Q. Wang. *Science Advances*, 2015, 1, e1500886.
- [43] Q. Huang, J. Yang, C. B. Ng, C. Jia, Q. Wang. *Energy & Environmental Science*, 2016, 9, 917.
- [44] Y. G. Zhu, X. Wang, C. Jia, J. Yang, Q. Wang. *ACS Catalysis*, 2016, 6, 6191.
- [45] Y. G. Zhu, C. Jia, J. Yang, F. Pan, Q. Huang, Q. Wang. *Chemical Communications*, 2015, 51, 9451.
- [46] S. Gu, K. Gong, E. Z. Yan, Y. Yan. *Energy & Environmental Science*, 2014, 7, 2986.
- [47] K. Gong, X. Ma, K. M. Conforti, K. J. Kuttler, J. B. Grunewald, K. L. Yeager *et al.* *Energy & Environmental Science*, 2015, 8, 2941.
- [48] Y. Yang, G. Zheng, Y. Cui. *Energy & Environmental Science*, 2013, 6, 1552.
- [49] W. A. Braff, M. Z. Bazant, C. R. Buie. *Nature Communications*, 2013, 4, 2346.
- [50] P. Navalpotro, J. Palma, M. Anderson, R. Marcilla. *Angewandte Chemie International Edition*, 2017, 56, 12460.
- [51] K. Gong, F. Xu, M. G. Lehrich, X. Ma, S. Gu, Y. Yan. *Journal of the Electrochemical Society*, 2017, 164, A2590.
- [52] M. O. Bamgbopa, Y. Shao-Horn, R. Hashaikeh, S. Almheiri. *Electrochimica Acta*,

- 2018, 267, 41.
- [53] X. Gao, Y. Chen, L. Johnson, P. G. Bruce. *Nature Materials*, 2016, 15, 882.
- [54] L. Wei, H. E. Karahan, S. Zhai, H. Liu, X. Chen, Z. Zhou *et al.* *Advanced Materials*, 2017, 29, 1701410.
- [55] Y. Li, H. Dai. *Chemical Society Reviews*, 2014, 43, 5257.
- [56] J. Fu, Z. P. Cano, M. G. Park, A. Yu, M. Fowler, Z. Chen. *Advanced Materials*, 2017, 29, 1604685.
- [57] M. Bockelmann, U. Kunz, T. Turek. *Electrochemistry Communications*, 2016, 69, 24.
- [58] F. Mahlendorf, C. Müller, D. Fuchs, A. Heinzl. in *231st ECS Meeting Vol. MA2017-01* 187 (New Orleans, 2017).
- [59] N. Imanishi, O. Yamamoto. *Materials Today*, 2014, 17, 24.
- [60] K. Lin, Q. Chen, M. R. Gerhardt, L. Tong, S. B. Kim, L. Eisenach *et al.* *Science*, 2015, 349, 1529.
- [61] X. Wei, G.-G. Xia, B. Kirby, E. Thomsen, B. Li, Z. Nie *et al.* *Journal of the Electrochemical Society*, 2016, 163, A5150.
- [62] K. Gong, F. Xu, J. B. Grunewald, X. Ma, Y. Zhao, S. Gu, Y. Yan. *ACS Energy Letters*, 2016, 1, 89.
- [63] C. Xie, Y. Duan, W. Xu, H. Zhang, X. Li. *Angewandte Chemie International Edition*, 2017, 56, 14953.
- [64] Y. H. Wen, H. M. Zhang, P. Qian, H. T. Zhou, P. Zhao, B. L. Yi, Y. S. Yang. *Journal of the Electrochemical Society*, 2006, 153, A929.
- [65] Y. H. Wen, H. M. Zhang, P. Qian, H. T. Zhou, P. Zhao, B. L. Yi, Y. S. Yang. *Electrochimica Acta*, 2006, 51, 3769.
- [66] H. D. Pratt, N. S. Hudak, X. Fang, T. M. Anderson. *Journal of Power Sources*, 2013, 236, 259.
- [67] J. Friedl, M. V. Holland-Cunz, F. Cording, F. L. Pfanschilling, C. Wills, W. McFarlane *et al.* *Energy & Environmental Science*, 2018, 11, 3010.
- [68] J.-J. Chen, M. D. Symes, L. Cronin. *Nature Chemistry*, 2018, 10, 1042.
- [69] Y. Liu, S. Lu, H. Wang, C. Yang, X. Su, Y. Xiang. *Advanced Energy Materials*, 2016, 7, 1601224.
- [70] X. Wei, W. Pan, W. Duan, A. Hollas, Z. Yang, B. Li *et al.* *ACS Energy Letters*, 2017, 2, 2187.
- [71] Y. Ding, C. Zhang, L. Zhang, Y. Zhou, G. Yu. *Chemical Society Reviews*, 2017, 47, 69.
- [72] M. Burgess, J. S. Moore, J. Rodríguez-López. *Accounts of Chemical Research*, 2016, 49, 2649.
- [73] W. Wang, V. Sprenkle. *Nature Chemistry*, 2016, 8, 204.
- [74] K. Lin, R. Gómez-Bombarelli, E. S. Beh, L. Tong, Q. Chen, A. Valle *et al.* *Nature Energy*, 2016, 1, 16102.
- [75] A. Orita, M. G. Verde, M. Sakai, Y. S. Meng. *Nature Communications*, 2016, 7, 13230.
- [76] S. Er, C. Suh, M. P. Marshak, A. Aspuru-Guzik. *Chemical Science*, 2015, 6, 885.
- [77] B. Hu, C. DeBruler, Z. Rhodes, T. L. Liu. *Journal of the American Chemical*

Society, 2017, 139, 1207.

- [78] E. S. Beh, D. De Porcellinis, R. L. Gracia, K. T. Xia, R. G. Gordon, M. J. Aziz. *ACS Energy Letters*, 2017, 2, 639.
- [79] Y. Ding, Y. Zhao, Y. Li, J. B. Goodenough, G. Yu. *Energy & Environmental Science*, 2017, 10, 491.
- [80] X. Wei, W. Xu, M. Vijayakumar, L. Cosimbescu, T. Liu, V. Sprenkle, W. Wang. *Advanced Materials*, 2014, 26, 7649.
- [81] T. Janoschka, N. Martin, U. Martin, C. Friebe, S. Morgenstern, H. Hiller *et al.* *Nature*, 2015, 527, 78.
- [82] T. Janoschka, N. Martin, M. D. Hager, U. S. Schubert. *Angewandte Chemie International Edition*, 2016, 55, 14427.
- [83] A. Hollas, X. Wei, V. Murugesan, Z. Nie, B. Li, D. Reed *et al.* *Nature Energy*, 2018, 3, 508.
- [84] X. Wei, L. Cosimbescu, W. Xu, J. Z. Hu, M. Vijayakumar, J. Feng *et al.* *Advanced Energy Materials*, 2015, 5, 1400678.
- [85] M. Milton, Q. Cheng, Y. Yang, C. Nuckolls, R. Hernández Sánchez, T. J. Sisto. *Nano Letters*, 2017, 17, 7859.
- [86] X. Wei, W. Xu, J. Huang, L. Zhang, E. Walter, C. Lawrence *et al.* *Angewandte Chemie International Edition*, 2015, 54, 8684.
- [87] A. Shimizu, K. Takenaka, N. Handa, T. Nokami, T. Itoh, J.-I. Yoshida. *Advanced Materials*, 2017, 29, 1606592.
- [88] S. Zhang, X. Li, D. Chu. *Electrochimica Acta*, 2016, 190, 737.
- [89] P. K. Leung, T. Martin, A. A. Shah, M. A. Anderson, J. Palma. *Chemical Communications*, 2016, 52, 14270.
- [90] Y. Xu, Y.-H. Wen, J. Cheng, G.-P. Cao, Y.-S. Yang. *Electrochimica Acta*, 2010, 55, 715.
- [91] B. Yang, L. Hooper-Burkhardt, F. Wang, G. K. Surya Prakash, S. R. Narayanan. *Journal of the Electrochemical Society*, 2014, 161, A1371.
- [92] Y. Zhao, Y. Ding, J. Song, G. Li, G. Dong, J. B. Goodenough, G. Yu. *Angewandte Chemie International Edition*, 2014, 53, 11036.
- [93] B. Hwang, M.-S. Park, K. Kim. *ChemSusChem*, 2015, 8, 310.
- [94] G. Cong, Y. Zhou, Z. Li, Y.-C. Lu. *ACS Energy Letters*, 2017, 2, 869.
- [95] J. Friedl, M. A. Lebedeva, K. Porfyraakis, U. Stimming, T. W. Chamberlain. *Journal of the American Chemical Society*, 2018, 140, 401.
- [96] J. Luo, B. Hu, C. Debruler, T. L. Liu. *Angewandte Chemie International Edition*, 2018, 57, 231.
- [97] J. Winsberg, C. Stolze, A. Schwenke, S. Muench, M. D. Hager, U. S. Schubert. *ACS Energy Letters*, 2017, 2, 411.
- [98] C. DeBruler, B. Hu, J. Moss, X. Liu, J. Luo, Y. Sun, T. L. Liu. *Chem*, 2017, 3, 961.
- [99] S.-E. Chun, B. Evanko, X. Wang, D. Vonlanthen, X. Ji, G. D. Stucky, S. W. Boettcher. *Nature Communications*, 2015, 6, 7818.
- [100] B. Hu, Y. Tang, J. Luo, G. Grove, Y. Guo, T. L. Liu. *Chemical Communications*, 2018, 54, 6871.

- [101] X. Wei, W. Duan, J. Huang, L. Zhang, B. Li, D. Reed *et al.* ACS Energy Letters, 2016, 1, 705.
- [102] J. D. Milshtein, S. L. Fisher, T. M. Breault, L. T. Thompson, F. R. Brushett. ChemSusChem, 2017, 10, 2080.
- [103] J. Huang, L. Cheng, R. S. Assary, P. Wang, Z. Xue, A. K. Burrell *et al.* Advanced Energy Materials, 2015, 5, 1401782.
- [104] E. Mourad, L. Coustan, P. Lannelongue, D. Zigah, A. Mehdi, A. Vioux *et al.* Nature Materials, 2017, 16, 446.
- [105] G. Hernández, M. Işik, D. Mantione, A. Pendashteh, P. Navalpotro, D. Shanmukaraj *et al.* Journal of Materials Chemistry A, 2017, 5, 16231.
- [106] M. H. Chakrabarti, F. S. Mjalli, I. M. AlNashef, M. A. Hashim, M. A. Hussain, L. Bahadori, C. T. J. Low. Renewable and Sustainable Energy Reviews, 2014, 30, 254.
- [107] C. Zhang, Y. Ding, L. Zhang, X. Wang, Y. Zhao, X. Zhang, G. Yu. Angewandte Chemie, 2017, 129, 7562.
- [108] J. Divisek, M. Eikerling, V. Mazin, H. Schmitz, U. Stimming, Y. M. Volkovich. Journal of the Electrochemical Society, 1998, 145, 2677.
- [109] D. G. Kwabi, K. Lin, Y. Ji, E. F. Kerr, M.-A. Goulet, D. De Porcellinis *et al.* Joule, 2018, 2, 1894.
- [110] J. Winsberg, C. Stolze, S. Muench, F. Liedl, M. D. Hager, U. S. Schubert. ACS Energy Letters, 2016, 1, 976.
- [111] T. Janoschka, C. Friebe, M. D. Hager, N. Martin, U. S. Schubert. ChemistryOpen, 2017, 6, 216.
- [112] Y. Zhu, F. Yang, Z. Niu, H. Wu, Y. He, H. Zhu *et al.* Journal of Power Sources, 2019, 417, 83.
- [113] G. Nagarjuna, J. Hui, K. J. Cheng, T. Lichtenstein, M. Shen, J. S. Moore, J. Rodríguez-López. Journal of the American Chemical Society, 2014, 136, 16309.
- [114] M. Watanabe, M. L. Thomas, S. Zhang, K. Ueno, T. Yasuda, K. Dokko. Chemical Reviews, 2017, 117, 7190.
- [115] R. Hayes, G. G. Warr, R. Atkin. Chemical Reviews, 2015, 115, 6357.
- [116] B. Wang, L. Qin, T. Mu, Z. Xue, G. Gao. Chemical Reviews, 2017, 117, 7113.
- [117] E. L. Smith, A. P. Abbott, K. S. Ryder. Chemical Reviews, 2014, 114, 11060.
- [118] I. Krossing, J. M. Slattery, C. Daguinet, P. J. Dyson, A. Oleinikova, H. Weingärtner. Journal of the American Chemical Society, 2006, 128, 13427.
- [119] J. Zhang, J. Wu, J. Yu, X. Zhang, J. He, J. Zhang. Materials Chemistry Frontiers, 2017, 1, 1273.
- [120] M. Armand, F. Endres, D. R. MacFarlane, H. Ohno, B. Scrosati. Nature Materials, 2009, 8, 621.
- [121] M.-C. Lin, M. Gong, B. Lu, Y. Wu, D.-Y. Wang, M. Guan *et al.* Nature, 2015, 520, 324.
- [122] Z. Liu, T. Cui, G. Pulletikurthi, A. Lahiri, T. Carstens, M. Olschewski, F. Endres. Angewandte Chemie International Edition, 2016, 55, 2889.
- [123] T. Watkins, A. Kumar, D. A. Buttry. Journal of the American Chemical Society, 2016, 138, 641.

- [124] A. Ejigu, P. A. Greatorex-Davies, D. A. Walsh. *Electrochemistry Communications*, 2015, 54, 55.
- [125] R. Chen, R. Hempelmann. *Electrochemistry Communications*, 2016, 70, 56.
- [126] M. A. Miller, J. S. Wainright, R. F. Savinell. *Journal of the Electrochemical Society*, 2016, 163, A578.
- [127] K. Takechi, Y. Kato, Y. Hase. *Advanced Materials*, 2015, 27, 2501.
- [128] Z. Guo, T. Zhang, M. Khan, S. Gao, T. Liu, J. Yu. *Electrochimica Acta*, 2014, 142, 132.
- [129] M. A. Bhat. *Electrochimica Acta*, 2012, 81, 275.
- [130] D. Gong, C. A. Grimes, O. K. Varghese, W. Hu, R. S. Singh, Z. Chen, E. C. Dickey. *Journal of Materials Research*, 2001, 16, 3331.
- [131] J. M. Macak, H. Tsuchiya, L. Taveira, S. Aldabergerova, P. Schmuki. *Angewandte Chemie International Edition*, 2005, 44, 7463.
- [132] Z. Su, W. Zhou, F. Jiang, M. Hong. *Journal of Materials Chemistry*, 2012, 22, 535.
- [133] A. J. Bard, L. R. Faulkner, *Electrochemical Methods: Fundamentals and Applications*. 2nd ed. New York: John Wiley & Sons, Inc., 2001.
- [134] H. Kim, J. Hong, K.-Y. Park, H. Kim, S.-W. Kim, K. Kang. *Chemical Reviews*, 2014, 114, 11788.
- [135] I. S. Chae, T. Luo, G. H. Moon, W. Ogieglo, Y. S. Kang, M. Wessling. *Advanced Energy Materials*, 2016, 6, 1600517.
- [136] Y. Liang, Y. Jing, S. Gheytani, K.-Y. Lee, P. Liu, A. Facchetti, Y. Yao. *Nature Materials*, 2017, 16, 841.
- [137] Z. Yuan, X. Zhu, M. Li, W. Lu, X. Li, H. Zhang. *Angewandte Chemie International Edition*, 2016, 55, 3058.
- [138] J. Liu, J. Wang, Z. Ku, H. Wang, S. Chen, L. Zhang *et al.* *ACS Nano*, 2016, 10, 1007.
- [139] S. Liu, G. L. Pan, N. F. Yan, X. P. Gao. *Energy & Environmental Science*, 2010, 3, 1732.
- [140] P. Ruetschi. *Journal of the Electrochemical Society*, 1973, 120, 331.
- [141] C. Wessells, R. Ruffo, R. A. Huggins, Y. Cui. *Electrochemical and Solid-State Letters*, 2010, 13, A59.
- [142] L. Suo, O. Borodin, T. Gao, M. Olguin, J. Ho, X. Fan *et al.* *Science*, 2015, 350, 938.
- [143] Y. Yamada, K. Usui, K. Sodeyama, S. Ko, Y. Tateyama, A. Yamada. *Nature Energy*, 2016, 1, 16129.
- [144] R. S. Kühnel, D. Reber, A. Remhof, R. Figi, D. Bleiner, C. Battaglia. *Chemical Communications*, 2016, 52, 10435.
- [145] G. Feng, X. Jiang, R. Qiao, A. A. Kornyshev. *ACS Nano*, 2014, 8, 11685.
- [146] R. Ye, D. Henkensmeier, S. J. Yoon, Z. Huang, D. K. Kim, Z. Chang *et al.* *Journal of Electrochemical Energy Conversion and Storage*, 2018, 15, 010801.
- [147] D. Wang, D. Choi, J. Li, Z. Yang, Z. Nie, R. Kou *et al.* *ACS Nano*, 2009, 3, 907.
- [148] C. A. Grimes. *Journal of Materials Chemistry*, 2007, 17, 1451.
- [149] Z.-W. Fu, Q.-Z. Qin. *The Journal of Physical Chemistry B*, 2000, 104, 5505.

- [150] E. P. Grishina, N. O. Kudryakova. Russian Journal of Physical Chemistry A, 2017, 91, 2024.
- [151] S. V. J. Yuvaraj, R. K. Zhdanov, R. V. Belosludov, V. R. Belosludov, O. S. Subbotin, K. Kanie *et al.* The Journal of Physical Chemistry B, 2015, 119, 12894.
- [152] R. van de Krol. "Principles of Photoelectrochemical Cells" in: *Photoelectrochemical Hydrogen Production* (Edited by: R. van de Krol, M. Grätzel), Springer, 2012, 13.
- [153] J. Vatamanu, O. Borodin. The Journal of Physical Chemistry Letters, 2017, 8, 4362.
- [154] R.-S. Kühnel, D. Reber, C. Battaglia. ACS Energy Letters, 2017, 2, 2005.
- [155] L. Suo, D. Oh, Y. Lin, Z. Zhuo, O. Borodin, T. Gao *et al.* Journal of the American Chemical Society, 2017, 139, 18670.
- [156] J. Zheng, G. Tan, P. Shan, T. Liu, J. Hu, Y. Feng *et al.* Chem, 2018, 4, 2872.
- [157] W. Liu, T. Zhao, Y. Zhang, H. Wang, M. Yu. Journal of Solution Chemistry, 2006, 35, 1337.
- [158] M. Saito, Y. Murota, M. Takagi, M. Tajima, T. Asao, H. Inoue *et al.* Journal of the Electrochemical Society, 2011, 159, A49.
- [159] F. Bordin, R. H. Colby, C. Cametti, L. De Lorenzo, T. Gili. The Journal of Physical Chemistry B, 2002, 106, 6887.
- [160] L. Suo, O. Borodin, W. Sun, X. Fan, C. Yang, F. Wang *et al.* Angewandte Chemie, 2016, 55, 7136.
- [161] Y. Xu, E. Memarzadeh Lotfabad, H. Wang, B. Farbod, Z. Xu, A. Kohandehghan, D. Mitlin. Chemical Communications, 2013, 49, 8973.
- [162] S. Liu, J. J. Hu, N. F. Yan, G. L. Pan, G. R. Li, X. P. Gao. Energy & Environmental Science, 2012, 5, 9743.
- [163] M. S. Sitze, E. R. Schreiter, E. V. Patterson, R. G. Freeman. Inorganic Chemistry, 2001, 40, 2298.
- [164] O. Rhee, G. Lee, J. Choi. ACS Applied Materials & Interfaces, 2016, 8, 14558.
- [165] W. Wang, M. Tian, A. Abdulagatov, S. M. George, Y.-C. Lee, R. Yang. Nano Letters, 2012, 12, 655.
- [166] S. Selverston, R. F. Savinell, J. S. Wainright. Journal of the Electrochemical Society, 2017, 164, A1069.
- [167] Z. Xie, Q. Su, A. Shi, B. Yang, B. Liu, J. Chen *et al.* Journal of Energy Chemistry, 2016, 25, 495.
- [168] D. P. Scamman, G. W. Reade, E. P. L. Roberts. Journal of Power Sources, 2009, 189, 1220.
- [169] C. D. Wu, D. A. Scherson, E. J. Calvo, E. B. Yeager, M. A. Reid. Journal of the Electrochemical Society, 1986, 133, 2109.
- [170] Y. K. Zeng, X. L. Zhou, L. An, L. Wei, T. S. Zhao. Journal of Power Sources, 2016, 324, 738.
- [171] F. Wang, O. Borodin, T. Gao, X. Fan, W. Sun, F. Han *et al.* Nature Materials, 2018, 17, 543.
- [172] C. Zhang, J. Holoubek, X. Wu, A. Daniyar, L. Zhu, C. Chen *et al.* Chemical Communications, 2018, 54, 14097.

- [173] Y. Wang, Z. Niu, Q. Zheng, C. Zhang, J. Ye, G. Dai *et al.* Scientific Reports, 2018, 8, 5740.
- [174] Y. Zhang, R. Ye, D. Henkensmeier, R. Hempelmann, R. Chen. Electrochimica Acta, 2018, 263, 47.
- [175] K. Amini, M. D. Pritzker. Electrochimica Acta, 2018, 268, 448.
- [176] J. Huang, L. Su, J. A. Kowalski, J. L. Barton, M. Ferrandon, A. K. Burrell *et al.* Journal of Materials Chemistry A, 2015, 3, 14971.
- [177] Y. Ding, G. Yu. Angewandte Chemie International Edition, 2016, 55, 4772.
- [178] M. Quan, D. Sanchez, M. F. Wasylkiw, D. K. Smith. Journal of the American Chemical Society, 2007, 129, 12847.
- [179] M. T. Huynh, C. W. Anson, A. C. Cavell, S. S. Stahl, S. Hammes-Schiffer. Journal of the American Chemical Society, 2016, 138, 15903.
- [180] N. Gamboa-Valero, P. D. Astudillo, M. A. González-Fuentes, M. A. Leyva, M. d. J. Rosales-Hoz, F. J. González. Electrochimica Acta, 2016, 188, 602.